Molecular dynamics simulations of H-induced plasma processes and cluster-catalyzed epitaxial growth of thin silicon films

Ha-Linh Thi Le

To cite this version:

Ha-Linh Thi Le. Molecular dynamics simulations of H-induced plasma processes and cluster-catalyzed epitaxial growth of thin silicon films. Computational Physics [physics.comp-ph]. Ecole Polytechnique X, 2014. English. NNT : . pastel-00985657

HAL Id: pastel-00985657
https://pastel.hal.science/pastel-00985657

Submitted on 30 Apr 2014

HAL is a multi-disciplinary open access archive for the deposit and dissemination of scientific research documents, whether they are published or not. The documents may come from teaching and research institutions in France or abroad, or from public or private research centers.

L'archive ouverte pluridisciplinaire **HAL**, est destinée au dépôt et à la diffusion de documents scientifiques de niveau recherche, publiés ou non, émanant des établissements d'enseignement et de recherche français ou étrangers, des laboratoires publics ou privés.

ÉCOLE POLYTECHNIQUE
UNIVERSITÉ PARIS-SACLAY

THESE

présentée en vue d'obtenir le grade de

DOCTEUR DE L'ECOLE POLYTECHNIQUE

Spécialité: Physique

Simulations de dynamique moléculaire des processus de plasma induits par l'hydrogène atomique et la croissance épitaxiale de couches minces de silicium catalysée par l'impact d'agrégats

par

Ha-Linh Thi LE

Thèse soutenue le 29 Janvier 2014 devant le jury composé de:

Prof. **Gilles OHANESSIAN**	Président du jury
Prof. **Laïfa BOUFENDI**	Rapporteur
Dr. **Thierry BELMONTE**	Rapporteur
Prof. **Khaled HASSOUNI**	Examinateur
Prof. **Gilles PESLHERBE**	Examinateur
Dr. **Philippe BARANEK**	Examinateur
Dr. **Holger VACH**	Directeur de thèse

“Life is like riding a bicycle.
To keep your balance, you must keep moving.”

- Albert Einstein

To my family

Acknowledgments

First of all, I gratefully acknowledge my directeur de thèse, Dr. Holger Vach, for giving me the inspiration with the field of thin silicon film deposition as well as molecular dynamics simulations and *ab initio* calculations, and for his continuous encouragement and support. During three years of my PhD, we have had a lot of discussions; and I have learnt from his great knowledge and experience that are valuable not only for my PhD thesis, but also for my future career.

My PhD thesis is the continuation of two PhD theses by Quentin Brulin and Ning Ning. I am grateful to Dr. Quentin Brulin and Dr. Ning Ning for their help to get started with my PhD work. I specially thank Dr. Ning Ning and Dr. Nancy Carolina Forero-Martinez for many fruitful discussions to solve "troubles" throughout all stages of my PhD work. I grant my sincere recognition to Prof. Pere Roca i Cabarrocas, Dr. Tatiana Novikova, and Romain Cariou for discussions concerning experimental aspects.

I would like to express my greatest gratitude to Prof. Gilles Ohanessian, Prof. Laïfa Boufendi, Dr. Thierry Belmonte, Prof. Khaled Hassouni, Prof. Gilles Peslherbe, and Dr. Philippe Baranek for accepting to be the jury members of my PhD thesis defense, for their careful reading of the manuscript, and for their positive evaluations of my PhD thesis.

Many thanks to Frédéric Liege and Eric Paillassa for their help with computer problems. Also special thanks to all LPICM members for their help and for giving their love to me.

I acknowledge the Institut du développement et des ressources en informatique scientifique (IDRIS), France and Center for Research in Molecular Modeling (CERMM), Concordia University, Canada for computational resources. The financial support from the Vietnamese government (USTH project), the LPICM, the EADS Corporate Foundation, and the Conseil franco-québécois de coopération universitaire is highly appreciated.

Last but not least, my deepest gratitude is to my friends, my teachers, and my family members who have always encouraged me in my choice of doing a PhD.

Abstract Three different processes taking place in a plasma reactor; namely, heating and melting of plasma-born hydrogenated silicon clusters by reactions with atomic hydrogen, hydrogen-induced healing of cluster-damaged silicon surfaces, and cluster-catalyzed epitaxial growth of thin silicon films have been investigated by means of molecular dynamics simulations.

Two plasma-born hydrogenated silicon clusters representing amorphous and crystalline structures are chosen to be exposed to atomic hydrogen as in a realistic plasma reactor. We investigate quantitatively how the clusters heat up and melt by the subsequent reactions with H-atoms.

A silicon surface which was partly damaged by a too violent cluster impact has been treated by hydrogen atoms. We have observed that the ill-defined silicon surface is rearranged to its initial crystalline structure after the exposure with atomic hydrogen if the appropriate H-atom flux is chosen; *i.e.*, due to the surface reaction dynamics with hydrogen atoms, the silicon atoms of the investigated hydrogenated silicon cluster are positioned in an epitaxial surface structure.

We have performed an in-depth study of the deposition dynamics of hydrogenated silicon clusters on a crystalline silicon substrate by controlling the parameters governing the cluster surface deposition. We have found that epitaxial growth of thin silicon films can be obtained from cluster deposition if the impact energies are sufficiently high for cluster atoms and surface atoms touching the cluster to undergo a phase transition to the liquid state before being recrystallized in an epitaxial order. Yet more strikingly, by applying a non-normal incidence angle for the impinging clusters, the epitaxial growth efficiency could considerably be enhanced. Those findings are crucially important to improve the high-speed growth of epitaxial silicon thin films at low temperatures using Plasma-Enhanced Chemical Vapor Deposition (PECVD) techniques for industrial applications.

Keywords: molecular dynamics simulations, hydrogen, hydrogenated silicon clusters, epitaxial growth, thin silicon films, non-normal incidence

Résumé Trois processus qui ont lieu dans un réacteur à plasma ont été étudiés au moyen de simulations de dynamique moléculaire: le chauffage et la fusion des agrégats de silicium hydrogéné par des réactions avec l'hydrogène atomique, la guérison induite par l'hydrogène des surfaces de silicium auparavant endommagées par l'impact violent d'agrégats, et la croissance épitaxiale des couches minces catalysée par des agrégats de silicium hydrogéné.

Deux agrégats de silicium hydrogéné qui représentent des structures amorphes et cristallines sont choisis pour être exposés à l'hydrogène atomique comme dans un réacteur à plasma réaliste. Nous avons étudié quantitativement comment les agrégats chauffent

et fondent par des réactions avec des atomes d'hydrogène.

Une surface de silicium qui a été partiellement endommagée par l'impact violent d'un agrégat a été traitée par des atomes d'hydrogène. Nous avons observé que la surface du silicium mal définie est réarrangée à sa structure cristalline initiale après l'exposition à l'hydrogène atomique ; à savoir, en raison de la dynamique de réaction de surface avec des atomes d'hydrogène, les atomes de silicium de l'agrégat de silicium hydrogéné sont positionnés dans une structure épitaxiale de la surface.

Ensuite, nous avons effectué une étude approfondie sur la dynamique du dépôt des agrégats de silicium hydrogéné sur un substrat de silicium cristallin en contrôlant les paramètres régissant le dépôt d'agrégat sur la surface. Nous avons trouvé que la croissance épitaxiale de couches minces de silicium peut être obtenue à partir de dépôts d'agrégats si les énergies d'impact sont suffisamment élevées pour que les atomes de l'agrégat et des atomes de la surface touchant l'agrégat subissent une transition de phase à l'état liquide avant d'être recristallisés dans un ordre épitaxial. Ce processus est d'une importance cruciale pour améliorer la croissance épitaxiale à grande vitesse des couches minces de silicium à basse température en utilisant la technique PECVD ("Plasma Enhanced Chemical Vapor Deposition") pour des applications industrielles.

Mots-clés : simulations de dynamique moléculaire, l'hydrogène, agrégats de silicium hydrogéné, croissance épitaxiale, couches minces de silicium

Contents

Contents v

List of Figures vii

List of Tables xi

1 Introduction 1

2 Computational methodology 6
2.1 Molecular dynamics simulations 6
2.1.1 Classical molecular dynamics simulation 6
2.1.1.1 Basic of molecular dynamics simulation 6
2.1.1.2 MD simulation procedure 7
2.1.1.3 Empirical interatomic Ohira-Tersoff potential 10
2.1.2 *Ab initio* molecular dynamics simulation 13
2.1.2.1 Why *ab initio* molecular dynamics? 13
2.1.2.2 Adiabatic and Born-Oppenheimer approximations 14
2.1.2.3 Kohn-Sham density functional theory 16
2.1.2.4 Born-Oppenheimer molecular dynamics 18
2.1.2.5 *Ab initio* forces: the Hellmann-Feynman theorem 19
2.2 Methods to “measure”system properties 20
2.2.1 Cluster temperature 20
2.2.2 Radial distribution function 21
2.2.3 Mean-square displacement 22

3 Heating and melting of plasma-born hydrogenated silicon clusters by reactions with atomic hydrogen 23
3.1 Introduction 23
3.2 Computational details 25
3.3 Results and Discussions 26
3.3.1 Hydrogen-induced heating of hydrogenated silicon nanoparticles . 26
3.3.1.1 $Si_{15}H_{10} + nH$ 26
3.3.1.2 $Si_{29}H_{24} + nH$ 27
3.3.2 Melting dynamics 28
3.4 Conclusions 33

4 Hydrogen-induced healing of cluster-damaged silicon surfaces 35
4.1 Introduction 35

4.2 Simulation details . . . 37
4.2.1 Deposition of plasma-born hydrogenated silicon clusters on H-terminated Si(100)-(2×1) surfaces . . . 37
4.2.2 Hydrogen treatment processes . . . 39
4.3 Results . . . 40
4.4 Conclusions . . . 45

5 Cluster-catalyzed epitaxial growth of thin silicon films 46
5.1 Introduction . . . 46
5.2 Simulation details . . . 50
5.3 Results . . . 51
5.3.1 Deposition of $Si_{15}H_{10}$ clusters on a H-terminated Si(100)-(2×1) surface . . . 51
5.3.2 Deposition of $Si_{8}H_{12}$ clusters on H-terminated Si(100)-(2×1) surfaces 56
5.3.3 Deposition of $Si_{28}H_{13}$ clusters on H-terminated Si(100)-(2×1) surfaces . . . 63
5.3.4 Deposition of $Si_{29}H_{24}$ clusters on H-terminated Si(100)-(2×1) surfaces . . . 67
5.4 Conclusions . . . 74

6 Conclusions and Perspectives 77

List of Figures

1.1 Schematic diagram of a parallel plate capacitively coupled RF glow discharge reactor. 3

3.1 The initial configuration of the hydrogenated silicon clusters. The large brown spheres represent silicon atoms while the small white ones represent hydrogen atoms. 25
3.2 The evolution of the instantaneous temperature of clusters with the number n of reactions with H-atoms: a) $Si_{15}H_{10}$; b) $Si_{29}H_{24}$. 27
3.3 The RDFs of the clusters during the heating processes induced by the subsequent reactions with H-atoms: a) $Si_{15}H_{10}$; b) $Si_{29}H_{24}$. 28
3.4 a) MSD of silicon atoms of the $Si_{15}H_{10}$ cluster at different temperatures due to the subsequent reactions with H-atoms; b) a zoom to show the details of the MSD graphs. 29
3.5 MSD of silicon atoms of the $Si_{29}H_{24}$ cluster at different temperatures due to the subsequent reactions with H-atoms: a) first six reactions with H-atoms; b) last six reactions with H-atoms. 30
3.6 a) Time evolution of the instantaneous temperature of the $Si_{29}H_{24}$ cluster after the reaction with the 12th H-atom for the chosen typical example; b) The MSD of silicon atoms of the cluster right after the reaction with the 12th H-atom at a temperature of 1813 K; c) The MSD of silicon atoms of the cluster after it equilibrated to 1668 K. 31
3.7 Self-diffusion coefficients of silicon atoms of the two considered clusters at different temperatures resulting from the subsequent hydrogen exposure reactions: a) $Si_{15}H_{10}$; b) $Si_{29}H_{24}$. 32

4.1 Snapshots at t = 10 ps of various trajectories of the deposition of the $Si_{29}H_{24}$ clusters with different impact energies on the substrates at different temperatures to illustrate various deposition mechanisms, from soft-landing to destructive deposition of clusters. 36
4.2 The initial configuration of the plasma-born $Si_{15}H_{10}$ cluster. The large brown spheres represent silicon atoms while the small white ones represent hydrogen atoms. 37
4.3 Side and top view of the initial configuration of the H-terminated Si(100)-(2×1) surface. The atom colors are the same as in Fig. 4.2. 38
4.4 Snapshots of the atomic configurations at various times during the deposition of the $Si_{15}H_{10}$ cluster onto the substrate at 573 K with an impact energy of 3.70 eV/atom. The large brown spheres represent surface silicon atoms while the green ones represent silicon atoms of the $Si_{15}H_{10}$ cluster. The small white spheres represent surface hydrogen atoms while the cyan ones represent hydrogen atoms of the $Si_{15}H_{10}$ cluster. 39

4.5 The evolution of the instantaneous temperature of the cluster atoms together with the substrate atoms touching the cluster after one reation with a H-atom: a) with Berendsen thermostat; b) without Berendsen thermostat. 40
4.6 The evolution of the instantaneous temperature of the cluster atoms together with the substrate atoms touching the cluster as function of the number of reactions with H-atoms. 41
4.7 Snapshots of the atomic configuration: a) before surface exposure to atomic hydrogen. The snapshot was recorded 20 ps after the impact of a $Si_{15}H_{10}$ cluster onto a substrate at 573 K with an impact energy of 3.70 eV/atom; b) after surface exposure to nine H-atoms. The violet atoms indicate the region where six silicon atoms of the “rough”surface rearranged themselves to a structure which has the same order as the initial substrate. 41
4.8 The structure evolution of the silicon surface after the 12 H-atom exposure, at a surface temperature around 1616 K. The blue atoms represent the silicon atoms found in epitaxial positions. 42
4.9 Side and top view of the atomic configuration after the cooling down to 573 K. 44
4.10 The RDF of the cluster atoms and the substrate atoms touching the cluster after the H-treatment and the cooling down to 573 K is compared with the RDF of those atoms before the H-exposure and with the RDF of bulk *c-Si* at 573 K. 44

5.1 The initial configurations of the employed hydrogenated silicon clusters. The large brown spheres represent silicon atoms while the small white ones represent hydrogen atoms. 50
5.2 Snapshots of atomic configurations at various times during the $Si_{15}H_{10}$ cluster surface collision with an impact energy of 5.3 eV/atom and a substrate temperature of 373 K. The large brown spheres represent the surface silicon atoms while the green ones represent silicon atoms of the $Si_{15}H_{10}$ cluster. The small white spheres represent surface hydrogen atoms while the cyan ones represent hydrogen atoms of the $Si_{15}H_{10}$ cluster. The same colors will be used to display atomic configurations of the following investigated trajectories. 52
5.3 Time evolution of the instantaneous temperature of atoms belonging to both the initial $Si_{15}H_{10}$ cluster and the substrate in the immediate vicinity of the cluster after impact. The insert shows that right after the impact the temperature of cluster atoms and substrate atoms touching the cluster exceeds 3000 K and then rapidly decreases to 1600 K. 53
5.4 Time evolution of the instantaneous temperature of substrate atoms surrounding the impact region in the reconstructed silicon layer after the $Si_{15}H_{10}$ cluster-surface impact. The insert indicates a rapid increase of the temperature of those atoms from 373 K to about 3000 K and a subsequent decrease to an equilibrated temperature of 1600 K. 53

5.5 Side and top view of the atomic configuration after cooling down the system to the experimental temperautre of 373 K in the case where the $Si_{15}H_{10}$ cluster approached the surface at 373 K with an impact energy of 5.3 eV/atom resulting in a local equilibrated heating at the impact region to 1600 K and the reoganisation of cluster and substrate atoms at the impact region to the perfectly ordered stucture of the initial substrate at about 78.70 ps. 54
5.6 RDFs of: a) bulk silicon at 373 K; b) the amorphous $Si_{15}H_{10}$ cluster at 300 K before impact; c) cluster and substrate atoms touching the cluster at 1 ps after the impact; d) cluster and substrate atoms touching the cluster after the cooling down to 373 K. The RDF graph of the cluster and substrate atoms touching the cluster after cooling down to 373 K is quite consistent with the one of crystalline bulk silicon. 55
5.7 MSDs of silicon atoms of the $Si_{15}H_{10}$ cluster and substrate silicon atoms touching the cluster: a) at 1 ps after the impact; b) after the cooling down to 373 K. 55
5.8 Side and top view of the atomic configuration after the cooling down to 373 K for the case of the Si_8H_{12} cluster approaching the substrate with an impact energy of 5.23 eV/atom. 57
5.9 MSDs of silicon atoms of the Si_8H_{12} cluster and substrate silicon atoms touching the cluster for the case of the Si_8H_{12} cluster approaching the substrate with an impact energy of 5.23 eV/atom: a) at 1 ps after the impact; b) after the cooling down to 373 K. 57
5.10 Side and top view of the atomic configuration at 200 ps after the collision for the case of the Si_8H_{12} cluster approaching the substrate at 473 K with an impact energy of 5.23 eV/atom. 58
5.11 Side and top view of the atomic configuration after the cooling down to 573 K for the case of the Si_8H_{12} cluster approaching the substrate with an impact energy of 5.23 eV/atom. 59
5.12 MSDs of silicon atoms of the Si_8H_{12} cluster and substrate silicon atoms touching the cluster for the case of the Si_8H_{12} cluster approaching the substrate with an impact energy of 5.23 eV/atom: a) at 1 ps after the impact; b) after the cooling down to 573 K. 59
5.13 Side and top view of the atomic configuration after the cooling down to 373 K for the case of the Si_8H_{12} cluster approaching the substrate with an impact energy of 9.95 eV/atom. 60
5.14 MSDs of silicon atoms of the Si_8H_{12} cluster and substrate silicon atoms touching the cluster for the case of the Si_8H_{12} cluster approaching the substrate with an impact energy of 9.95 eV/atom: a) at 1 ps after the impact; b) after the cooling down to 373 K. 60
5.15 Side and top view of the atomic configuration after the cooling down to 473 K for the case of the Si_8H_{12} cluster approaching the substrate at 473 K with an impact energy of 9.95 eV/atom. 62
5.16 MSDs of silicon atoms of the Si_8H_{12} cluster and substrate silicon atoms touching the cluster for the case of the Si_8H_{12} cluster approaching the substrate at 473 K with an impact energy of 9.95 eV/atom: a) at 1 ps after the impact; b) after the cooling down to 473 K. 62

5.17 Side and top view of the atomic configuration at 200 ps after the collision for the case of the Si_8H_{12} cluster approaching the substrate at 573 K with an impact energy of 9.95 eV/atom. 63
5.18 Snapshots of the atomic configurations at 200 ps after the impact of the $Si_{28}H_{13}$ cluster onto the silicon surface for various impact energies: a) 2.46, b) 2.84, c) 3.08, d) 3.77, and e) 5.37 eV/atom. The substrate temperature is always at 373 K. 64
5.19 Snapshots of the atomic configurations at 200 ps after the impact of the $Si_{28}H_{13}$ cluster with the surface for different substrate temperatures: a) 373 K; b) 573 K. The impact energy is always 2.84 eV/atom. 66
5.20 Snapshots of the atomic configurations at 200 ps after the impact of the $Si_{29}H_{24}$ cluster with the surface for various impact energies: a) 2.74, b) 3.03, c) 3.67, and d) 5.31 eV/atom. The substrate temperature is always 373 K. 67
5.21 Snapshots of the atomic configurations at 200 ps after the impact of the $Si_{29}H_{24}$ cluster with the surface for various substrate temperatures: a) 373, b) 473, and c) 573 K. The impact energy is always 2.74 eV/atom. . . 69
5.22 Snapshots of atomic configurations at various times during the $Si_{29}H_{24}$ cluster surface collision with an impact energy of 3.67 eV/atom, a substrate temperature of 473 K, and a normal incidence angle. 70
5.23 Snapshots of atomic configurations at various times during the $Si_{29}H_{24}$ cluster surface collision with an impact energy of 3.67 eV/atom, a substrate temperature of 473 K, and an incidence angle of 30 degrees. 71
5.24 Time evolution of the instantaneous temperature of atoms belonging to both the initial $Si_{29}H_{24}$ cluster and the substrate in the immediate vicinity of the cluster after the impact. 72
5.25 Side and top view of the atomic configuration after the cooling down to 473 K for the case of the $Si_{29}H_{24}$ cluster approaching the surface at 473 K with an impact energy of 3.67 eV/atom and an incidence angle of 30 degrees. 72
5.26 RDFs of silicon atoms of the $Si_{29}H_{24}$ cluster and substrate atoms touching the cluster: a) at 1 ps after the impact; b) after the cooling down to 473 K for the case of the $Si_{29}H_{24}$ cluster approaching the surface at 473 K with an impact energy of 3.67 eV/atom and an incidence angle of 30 degrees. . 73
5.27 MSDs of silicon atoms of the $Si_{29}H_{24}$ cluster and substrate atoms touching the cluster for the case of the $Si_{29}H_{24}$ cluster approaching the surface at 473 K with an impact energy of 3.67 eV/atom and an incidence angle of 30 degrees: a) at 1 ps after the impact; b) after the cooling down to 473 K. 73
5.28 Snapshots of atomic configurations at various times during the $Si_{29}H_{24}$ cluster surface collision with an impact energy of 3.67 eV/atom, a substrate temperature of 473 K, and an incidence angle of 45 degrees. 74

List of Tables

2.1 Parameters of the Ohira-Tersoff potential 12
2.2 Comparison of the energies and structures of *c-Si* and H-terminated Si(100)-(2×1) predicted by the OT potential with experimental and *ab initio* results. 13

Chapter 1

Introduction

In the continuing progress of microelectronic and photovoltaic devices, thin silicon films play an important role because they are the basis for many technological innovations toward low cost products, *e.g.*, the design of solar cells based on silicon thin films, such as hydrogenated amorphous silicon, hydrogenated polymorphous silicon, and epitaxially-grown crystalline silicon thin films.

Amorphous silicon (*a-Si*) materials [1, 2] have no long-range order structure like crystalline silicon (*c-Si*). Instead, they possess a short-range order structure in the way that the number of neighbors and the average bond lengths and angles are the same as in *c-Si*; *i.e.*, the first few nearest neighbor distances are the same for both materials. Small random changes in atomic bond lengths, however, then lead to the absence of long-range order in the amorphous material as can be witnessed in the corresponding pair correlation functions as will be shown in the following chapters. Moreover, not all silicon atoms in an *a-Si* network are fourfold coordinated. Some of them lack one, two, or three bonds to other silicon atoms; *i.e.*, they contain dangling bonds. These dangling bonds represent defects and can be passivated by H-atoms. When the material is obtained by the dissociation of silane in a plasma, there is the presence of hydrogen atoms in the *a-Si* network resulting in a different material called hydrogenated amorphous silicon (*a-Si:H*). In the world of photovoltaic technologies, amorphous silicon modules are commercial products [3].

Polymorphous hydrogenated silicon (*pm-Si:H*) [4, 5] is a nanostructured material consisting of silicon nanocrystals embedded in a hydrogenated amorphous silicon matrix. Because of this particular structure, *pm-Si:H* exhibits many improved properties with respect to *a-Si:H*; namely, a low defect density ($\sim 5 \times 10^{14}/\mathrm{cm}^3$) [6, 7], increased transport properties, enhanced stability under illumination [7–10]. Therefore, *pm-Si:H* is a competitive candidate in comparison with *a-Si:H* for potential applications in large

area electronic devices, such as thin film solar cells, electroluminescent diodes, non-volatile memories, and single-electron transistors [11, 12].

Epitaxially-grown crystalline silicon thin films: The oriented growth of a crystalline material on a single crystal surface is called epitaxy [13]. In the field of epitaxial growth, molecular beam epitaxy (MBE) is the standard technique, but it requires the use of an ultra-high vacuum system. Epitaxial growth of thin silicon films on crystalline silicon substrates has been studied with alternative techniques, *e.g.*, ion beam epitaxy (IBE) [14], hot wire chemical vapor deposition (HWCVD) [15], and plasma enhanced chemical vapor deposition (PECVD) [16, 17]. The latter was reported to offer some advantages, such as the production of epitaxial silicon films at low substrate temperatures (as low as 150 °C [18]). At high hydrogen flow rates, epitaxial silicon films grown from $SiF_4/H_2/Ar$ gas mixtures at substrate temperature $\sim 200\,°C$ in a radio frequency (RF) PECVD reactor form a porous interface layer with the crystalline silicon wafer that can be used to transfer the epitaxial films to foreign substrates [19].

This PhD work has been inspired by the experimental work at the "Laboratoire de Physique des Interfaces et Couches Minces" (LPICM) to get a better understanding for the deposition processes of silicon thin films with PECVD techniques, *e.g.*, hydrogenated polymorphous silicon and epitaxially-grown crystalline silicon thin films. PECVD has been widely used in the industrial manufacturing of thin silicon films [20]. One of the advantages of PECVD in comparison to other chemical vapor deposition (CVD) techniques is that the deposition can be operated with lower substrate temperatures, hence, allowing the use of cheap substrate materials as polymer foils.

Figure 1.1 is a schematic diagram of a parallel plate capacitively coupled RF glow discharge reactor with the species contributing to the film deposition shown at the plasma sheath [20]. Depending on the plasma conditions, such as pressure, gas ratios, and power, we can control the film precursors approaching the substrate. At low silane dissociation rates, silicon radicals and ions can be considered to be the main film precursors. Increasing the pressure will lead to secondary reactions and the formation of clusters, nanocrystals, and eventually powders in the gase phase of the plasma. Hydrogenated silicon clusters/nanocrystals formed in the plasma suffer from charge fluctuations. As long as they are negatively charged, they are trapped in the plasma between the sheath regions and can continue their growth. As soon as they become neutrally or positively charged they can leave the plasma and deposit on the substrate. The former ones represent roughly 25% of the plasma exiting clusters and will impact on the substrate with room temperature velocities. Positively charged nanoparticles that represent roughly 75% of the depositing clusters will be accelerated toward the substrate due to the plasma potential. For those nanoparticles, the impact energy can precisely be controlled by a conducting grid placed in front of the substrate [21]. In addition, they can be produced with a narrow size dispersion by the use of modulated discharges (*e.g.*, square

pulse plasmas), and their radial growth rate can be extremely high (up to 75 nm/s) [22]. Hydrogenated silicon clusters/nanocrystals synthesized in plasma reactors can be used as building blocks for the thin silicon film production with high-speed deposition rates necessary for industrial applications [20, 23]. For the same deposition conditions, it is shown in Ref. [16] that the presence of plasma-born hydrogenated silicon clusters/-nanocrystals results into *a-Si:H* films when glass or (111) *c-Si* substrates are used, while epitaxial silicon thin films are grown when depositing on (100) *c-Si* substrates. Therefore, depending on the plasma conditions and the substrate properties, various silicon thin films can be obtained, from standard *a-Si:H*, *pm-Si:H*, microcrystalline (μc-*Si:H*) to epitaxial silicon thin films.

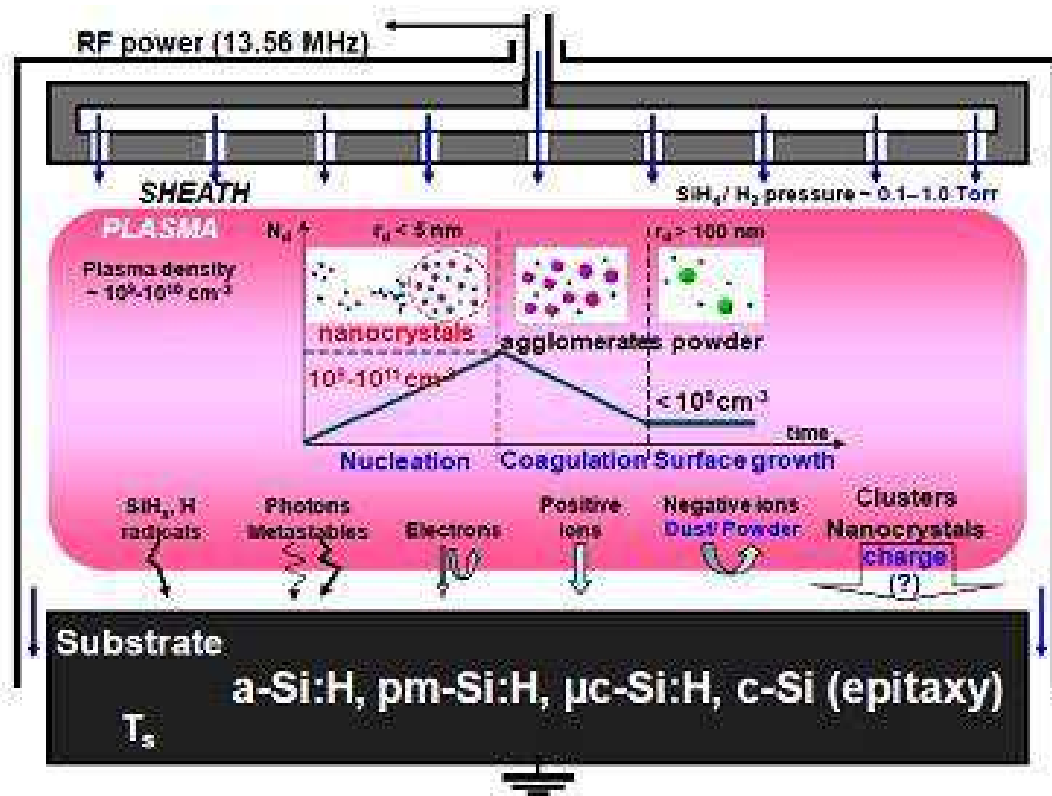

FIGURE 1.1: Schematic diagram of a parallel plate capacitively coupled RF glow discharge reactor.

For the previous simulations, the results of fluid dynamics models for a H_2/SiH_4 discharge were used as input data to simulate the formation of hydrogenated silicon nanoparticles by means of semi-empirical molecular dynamics [24–26]. The growth process was started by the reaction between a SiH_4 molecule and a SiH_3 radical. After this first reaction, a cluster was grown by additional reactive collisions with SiH_4 molecules. All of the formed clusters display amorphous structures, very rich in hydrogen with the hydrogen atoms always on top of the cluster surfaces. Atomic hydrogen was found to play a crucial role in the crystallization of amorphous hydrogenated silicon clusters

generated in a plasma reactor [22, 24, 27, 28]. The interaction with atomic hydrogen leads to cluster heating while the collision with hydrogen molecules cools the cluster down. Heating from reactions with H-atoms is necessary for the cluster to overcome energy barriers to more stable structures. Depending on the impinging H-atom flow rates and cooling down rates of clusters by the collisions with hydrogen molecules, they can become either amorphous or crystalline. For very high H impact rates, however, the clusters can melt since the clusters do not have sufficient time to cool down between two subsequent collisions with hydrogen atoms. The first subject in the thesis is, thus, devoted to investigate quantitatively how atomic hydrogen heats up plasma-born hydrogenated silicon nanoparticles necessary for their melting and crystallization before their deposition on a substrate.

Deposition dynamics of silicon clusters on crystalline silicon substrates has been extensively studied with molecular dynamics simulations. Those studies concentrate on the influence of impact parameters on the growth mechanisms of silicon thin films, *e.g.*, amorphous and epitaxial silicon thin films using ionized cluster beam techniques [29–40]. It was shown that the impact energy is the most important parameter and the substrate temperature only plays a second role. Ning *et al.* [35, 36] have investigated the deposition of hydrogenated silicon clusters on a H-terminated Si(100)-(2×1) substrate under realistic plasma conditions. The results reveal that cluster-surface interaction mechanisms strongly depend on the impact energy. Low impact energies lead to soft-landing of clusters on the substrate. At an intermediate impact energy range, the clusters partially dissociate. Complete cluster dissociation followed by fragment migration onto the surface and cluster atom penetration into the lattice is found for high impact energies [36]. Moreover during the thin silicon film growth by PECVD, there is always a flux of atomic hydrogen to the surface resulting from the dissociation of silane and hydrogen molecules in the plasma reactor. The second research topic of the thesis is to answer the question if H-atoms in the reactor can repair the silicon surfaces, which were locally damaged by violent cluster impacts, to the initial crystalline silicon surface.

Recently, it has been shown experimentally that high-quality epitaxial growth of silicon thin films in a PECVD reactor can be achieved at low temperatures and high deposition rates when plasma-born hydrogenated silicon clusters are used as deposition precursors [17, 19, 41]. Therefore, the last subject of the thesis deals with cluster-catalyzed epitaxial growth of thin silicon films. Our research is focused on the question which experimental conditions can lead to high-speed epitaxial growth of thin silicon films from the deposition of silicon nanoparticles. Contrary to a former study [42], it is shown that the cluster impact energy has to be sufficiently elevated not only to break apart the atoms of the impinging cluster, but also to destroy the surface atom organization in the impact area. If the breaking of the surface order remains sufficiently localized,

the ensemble of cluster and local surface atoms will then reorganize themselves to obtain an epitaxially grown surface structure under the condition that the resulting excess energy can be sufficiently fast evacuated to the deeper layers of the silicon substrate.

The presented studies are based on numerical simulations. In the following chapter, we describe, therefore, the basic concepts of classical and *ab initio* molecular dynamics simulations as well as the methods to determine cluster temperature, to analyze structure characteristics, and to evaluate the system phase states.

Chapter 2

Computational methodology

This work is dedicated to study the H-induced plasma processes and cluster-catalyzed epitaxial growth of thin silicon films by means of molecular dynamics simulations. These simulations have been performed with the general chemical dynamics computer program VENUS [43] and the *ab initio* simulation package VASP[44–46]. In this chapter, we present the basic ideas of classical and *ab initio* molecular dynamics simulations, the typical procedure of a molecular dynamics simulation, and tools to analyze system properties from the phase-space trajectories of the system saved after each molecular dynamics simulation.

2.1 Molecular dynamics simulations

2.1.1 Classical molecular dynamics simulation

2.1.1.1 Basic of molecular dynamics simulation

Together with the invention and the continuously increasing power of electronic computers, computer simulations have become very powerful tools supporting theory and experiments. They serve as the numerical "experiments" designed to test the quality of theories. Computer simulations are also employed to predict the properties of materials because computers are able to "measure" the properties at extreme conditions (for instance, high pressures or temperatures) that are difficult or expensive to measure in experiments.

Since the earliest computer simulations were performed in the 1950s, numerous simulation methods have been developed and applied in many fields of science [47]. Molecular dynamics (MD) simulation, a technique involving numerically solving differential

equations of motion, has been widely used in physics, chemistry, biology, and materials science. It allows us to access to N-body systems at the atomic scale, therefore, we can investigate the materials properties at levels that are inaccessible in experiments. MD simulations are based on Newton's Second Law of motion:

$$\mathbf{F}_i = m_i \mathbf{a}_i = m_i \frac{d^2 \mathbf{r}_i}{dt^2}, \tag{2.1}$$

where $\mathbf{F}_i$ is the force acting on the particle i due to the interaction with the other particles in the system; m_i, $\mathbf{a}_i$, and $\mathbf{r}_i$ are particle mass, acceleration, and position, respectively; and t is time. The force $\mathbf{F}_i$ can also be determined as the negative gradient of the total potential energy of the system $V(\mathbf{r}_1, \mathbf{r}_2, ..., \mathbf{r}_N)$,

$$\mathbf{F}_i = -\frac{\partial}{\partial \mathbf{r}_i} V(\mathbf{r}_1, \mathbf{r}_2, ..., \mathbf{r}_N). \tag{2.2}$$

Therefore, we need to know the total potential energy of the system to solve the set of equations (2.1). Before starting any MD simulation, we have to choose a relevant interaction potential that describes well the system as well as the examined properties. The solution of the set of equations (2.1) gives us the positions and velocities of each individual particle in the system at any time, *i.e.*, the phase-space trajectories of the system.

2.1.1.2 MD simulation procedure

MD simulations in many respects are very similar to real experiments. When we carry out a real experiment: first, we prepare a sample; second, we connect this sample to a measuring instrument; and finally, we measure the property of interest during a certain time interval. In a MD simulation, we follow a similar procedure. A typical MD simulation consists of the following steps:

- Initialize the system: We select initial positions and velocities of all particles in the system.
- Compute the forces acting on all particles.
- Integrate Newton's equations of motion. This step and the previous one are crucial in the simulation. They are repeated for a certain number of time-steps chosen in the simulation. The system evolves into the thermal equilibrium.
- Compute the averages of measured quantities.

The most time-consuming part of MD simulations is the calculation of the forces at each time-step. For a pair potential the CPU time necessary to evaluate the forces scales as N^2, and for an N-body potential it scales as N^N. Several techniques have been designed to efficiently speed up the evaluation of both short-range and long-range forces. Details of these techniques are found in references [48, 49].

Many methods are available for integrating the equations of motion (2.1). Most of them are finite-difference techniques. The criterion to judge finite-difference algorithms used in MD simulations is total energy conservation. If we want to examine the system for a certain time interval; the longer time-step that we can use, the fewer number of time-steps needs to be calculated. Because the evaluations of the forces are time-consuming, an efficient integration algorithm should allow the use of relatively large time-step and ensure long-term total energy conservation. In the VASP software, the Verlet algorithm or the fourth-order predictor-corrector is available to integrate Newton's equations of motion. We have used the Verlet algorithm to perform our MD simulations. The fourth-order Runge-Kutta algorithm and the fifth-order predictor-corrector algorithm of Gear have been employed in the VENUS program. The basis of these integration algorithms will be presented below.

Verlet algorithm

To derive the trajectory equations, we expand the coordinate of a particle at time $t+\Delta t$ as a second-order Taylor expansion:

$$\mathbf{r}_i(t+\Delta t) = \mathbf{r}_i(t) + \mathbf{v}_i(t)\Delta t + \frac{1}{2}\frac{\mathbf{F}_i(t)}{m_i}(\Delta t)^2 + O((\Delta t)^3). \tag{2.3}$$

Similarly,

$$\mathbf{r}_i(t-\Delta t) = \mathbf{r}_i(t) - \mathbf{v}_i(t)\Delta t + \frac{1}{2}\frac{\mathbf{F}_i(t)}{m_i}(\Delta t)^2 - O((\Delta t)^3). \tag{2.4}$$

Adding Eqs. (2.3) and (2.4), we obtain:

$$\mathbf{r}_i(t+\Delta t) = 2\mathbf{r}_i(t) - \mathbf{r}_i(t-\Delta t) + \frac{\mathbf{F}_i(t)}{m_i}(\Delta t)^2 + O((\Delta t)^4). \tag{2.5}$$

Thus, we can calculate the position at time $t+\Delta t$ if we know the positions at times t and $t-\Delta t$. The error of the estimate of new position is of order $(\Delta t)^4$, where Δt is the time-step in our MD simulations. The velocity is computed by subtracting Eq. (2.4) from Eq. (2.3):

$$\mathbf{v}_i(t) = \frac{\mathbf{r}_i(t+\Delta t) - \mathbf{r}_i(t-\Delta t)}{2\Delta t} + O((\Delta t)^2). \tag{2.6}$$

Runge-Kutta Algorithm

For the MD simulations performed with VENUS program, positions and momenta are calculated by the fourth-order Runge-Kutta method for the first six time-steps to generate derivatives of $\mathbf{r}_i(t_0)$: $\dot{\mathbf{r}}_i(t_0)$, $\ddot{\mathbf{r}}_i(t_0)$, $\mathbf{r}_i^{(iii)}(t_0)$, $\mathbf{r}_i^{(iv)}(t_0)$, and $\mathbf{r}_i^{(v)}(t_0)$, which are used

as the starting point for the Gear's predictor-corrector algorithm.

The Runge-Kutta methods have the structure of the Euler's method in which the position of a particle at time $t + \Delta t$ is expanded as a first-order Taylor series,

$$\mathbf{r}_i(t + \Delta t) = \mathbf{r}_i(t) + \dot{\mathbf{r}}_i(t)\Delta t + O((\Delta t)^2). \tag{2.7}$$

The fourth-order Runge-Kutta algorithm [50] makes four estimates of $\dot{\mathbf{r}}_i$ at various points in the time interval $[t, t + \Delta t]$:

$$\begin{aligned}
k_1 &= \dot{\mathbf{r}}_i(t), \\
k_2 &= \dot{\mathbf{r}}_i(t + \frac{1}{2}\Delta t, \mathbf{r}_i(t) + \frac{1}{2}k_1\Delta t), \\
k_3 &= \dot{\mathbf{r}}_i(t + \frac{1}{2}\Delta t, \mathbf{r}_i(t) + \frac{1}{2}k_2\Delta t), \\
k_4 &= \dot{\mathbf{r}}_i(t + \Delta t, \mathbf{r}_i(t) + k_3\Delta t),
\end{aligned} \tag{2.8}$$

which lead to the approximate value of the trajectory for the next time-step:

$$\mathbf{r}_i(t + \Delta t) = \mathbf{r}_i(t) + \frac{1}{6}(k_1 + 2k_2 + 2k_3 + k_4)\Delta t + O((\Delta t)^5). \tag{2.9}$$

Predictor-corrector algorithm of Gear

The Gear predictor-corrector algorithm [51] includes the following steps:

Prediction: The position of a particle at time $t + \Delta t$ is developed as a fifth-order Taylor expansion consisting of the particle position and their derivatives at time t. Therefore, we need to know the derivatives $\dot{\mathbf{r}}_i$, $\ddot{\mathbf{r}}_i$, $\mathbf{r}_i^{(iii)}$, $\mathbf{r}_i^{(iv)}$, and $\mathbf{r}_i^{(v)}$ at each time-step. These derivatives are also predicted at time $t + \Delta t$ by applying Taylor expansions at time t,

$$\begin{aligned}
&\mathbf{r}_i(t + \Delta t) = \mathbf{r}_i(t) + \dot{\mathbf{r}}_i(t)\Delta t + \ddot{\mathbf{r}}_i(t)\frac{(\Delta t)^2}{2!} + \mathbf{r}_i^{(iii)}(t)\frac{(\Delta t)^3}{3!} + \mathbf{r}_i^{(iv)}(t)\frac{(\Delta t)^4}{4!} + \mathbf{r}_i^{(v)}(t)\frac{(\Delta t)^5}{5!}, \\
&\dot{\mathbf{r}}_i(t + \Delta t) = \dot{\mathbf{r}}_i(t) + \ddot{\mathbf{r}}_i(t)\Delta t + \mathbf{r}_i^{(iii)}(t)\frac{(\Delta t)^2}{2!} + \mathbf{r}_i^{(iv)}(t)\frac{(\Delta t)^3}{3!} + \mathbf{r}_i^{(v)}(t)\frac{(\Delta t)^4}{4!}, \\
&\ddot{\mathbf{r}}_i(t + \Delta t) = \ddot{\mathbf{r}}_i(t) + \mathbf{r}_i^{(iii)}(t)\Delta t + \mathbf{r}_i^{(iv)}(t)\frac{(\Delta t)^2}{2!} + \mathbf{r}_i^{(v)}(t)\frac{(\Delta t)^3}{3!}, \\
&\mathbf{r}_i^{(iii)}(t + \Delta t) = \mathbf{r}_i^{(iii)}(t) + \mathbf{r}_i^{(iv)}(t)\Delta t + \mathbf{r}_i^{(v)}(t)\frac{(\Delta t)^2}{2!}, \\
&\mathbf{r}_i^{(iv)}(t + \Delta t) = \mathbf{r}_i^{(iv)}(t) + \mathbf{r}_i^{(v)}(t)\Delta t, \\
&\mathbf{r}_i^{(v)}(t + \Delta t) = \mathbf{r}_i^{(v)}(t).
\end{aligned} \tag{2.10}$$

The quantities obtained by this development are called *predicted values*. These values will then be *corrected*.

Evaluation: Based on the predicted positions, we recalculate the potentials yielding

to new values for the forces on all particles, consequently all particle accelerations at time $t + \Delta t$.

Correction: The difference between the predicted accelerations and the corrected accelerations is obtained:

$$\Delta \ddot{\mathbf{r}}_i(t + \Delta t) = \ddot{\mathbf{r}}_i^c(t + \Delta t) - \ddot{\mathbf{r}}_i^p(t + \Delta t). \tag{2.11}$$

This difference for the acceleration is then used to correct all predicted positions and their derivatives at time $t + \Delta t$:

$$\begin{aligned}
&\mathbf{r}_i^c = \mathbf{r}_i^p + \alpha_0 \Delta\mathbf{R2}, \\
&\dot{\mathbf{r}}_i^c \Delta t = \dot{\mathbf{r}}_i^p \Delta t + \alpha_1 \Delta\mathbf{R2}, \\
&\frac{\ddot{\mathbf{r}}_i^c (\Delta t)^2}{2!} = \frac{\ddot{\mathbf{r}}_i^p (\Delta t)^2}{2!} + \alpha_2 \Delta\mathbf{R2}, \\
&\frac{\mathbf{r}_i^{(iii)c} (\Delta t)^3}{3!} = \frac{\mathbf{r}_i^{(iii)p} (\Delta t)^3}{3!} + \alpha_3 \Delta\mathbf{R2}, \\
&\frac{\mathbf{r}_i^{(iv)c} (\Delta t)^4}{4!} = \frac{\mathbf{r}_i^{(iv)p} (\Delta t)^4}{4!} + \alpha_4 \Delta\mathbf{R2}, \\
&\frac{\mathbf{r}_i^{(v)c} (\Delta t)^5}{5!} = \frac{\mathbf{r}_i^{(v)p} (\Delta t)^5}{5!} + \alpha_5 \Delta\mathbf{R2},
\end{aligned} \tag{2.12}$$

where

$$\Delta\mathbf{R2} \equiv \Delta \ddot{\mathbf{r}}_i(t + \Delta t) \frac{(\Delta t)^2}{2!}. \tag{2.13}$$

This correction is given by a set of coefficients that Gear derived empirically to assure the best numerical stability of his algorithm [52, 53]:

$$\alpha_0 = \frac{3}{16}, \alpha_1 = \frac{251}{360}, \alpha_2 = 1, \alpha_3 = \frac{11}{18}, \alpha_4 = \frac{1}{6}, \textit{ and } \alpha_5 = \frac{1}{60}. \tag{2.14}$$

2.1.1.3 Empirical interatomic Ohira-Tersoff potential

Silicon, the second most abundant element in the Earth's crust, plays the major role in microelectronic and photovoltaic technologies. Because of its importance in technology, several empirical interatomic potentials have been developed by Stillinger and Weber [54], Tersoff [55], Biswas and Hamann [56], Dodson [57], and Baskes [58] to describe silicon structures, such as nanoparticles, nanowires, and thin films; and to study their static and dynamic properties.

Ohira-Tersoff (OT) potential, an extension of the Tersoff potential to include the Si-H and H-H interactions, has been shown to perform well in describing the structure and properties of bulk *a-Si:H* material [59], the structure and energy of the Si(100)-(2×1) and the H-terminated Si(100)-(2×1) surfaces [60, 61]. It has been successfully used to

investigate the interactions of SiH_x (x = 1, 2, 3) radicals with silicon surfaces [61–63], the adsorption mechanisms and energetics of the SiH_3 radical on the pristine Si(001)-(2×1) surface [64], the growth and characterization of *a-Si:H* thin films from SiH or SiH_2 radical precursor [65, 66], and hydrogen-induced crystallization of amorphous silicon thin films [67]. The OT potential, however, does not describe well the structural characteristics and the energies of small silicon hydride molecules [26, 42]. Recently, N. Ning *et al.* have used coupled-cluster methods to re-optimize the parameters of the OT potential to study hydrogenated silicon nanoparticle collisions [42] and the interaction of small hydrogenated silicon molecules and radicals with a crystalline silicon substrate under typical plasma conditions [36]. Because of its wide applications in the Si:H systems, the OT potential has been employed in this work to simulate the H-treatment of cluster-damaged silicon surfaces and the cluster-catalyzed epitaxial growth of silicon thin films.

The OT potential V is given as a function of atomic coordinates in the following:

$$V = \frac{1}{2}\sum_{i}\sum_{j\neq i}[a_{ij}V_r(r_{ij}) + b_{ij}V_a(r_{ij})]f_c(r_{ij}), \tag{2.15}$$

where

$$V_r(r_{ij}) = A_{ij}exp(-\lambda_{ij}r_{ij}), V_a(r_{ij}) = -B_{ij}exp(-\mu_{ij}r_{ij}), \tag{2.16}$$

$$a_{ij} = \epsilon_{ij}(1 + \beta_i^{n_i}\tau_{ij}^{n_i})^{-1/2n_i}, b_{ij} = \chi_{ij}(1 + \beta_i^{n_i}\xi_{ij}^{n_i})^{-m_i/2n_i}, \tag{2.17}$$

$$\tau_{ij} = \sum_{k\neq i,j} f_c(r_{ik})\delta_{ik}g(\theta_{ijk}), \tag{2.18}$$

$$\xi_{ij} = \sum_{k\neq i,j} f_c(r_{ik})\omega_{ik}g(\theta_{ijk})exp[\sigma_{ik}(r_{ij} - r_{ik})], \tag{2.19}$$

$$g(\theta_{ijk}) = 1 + \frac{c_i^2}{d_i^2} - \frac{c_i^2}{d_i^2 + (h_i - cos\theta_{ijk})^2}, \tag{2.20}$$

$$f_c(r_{ij}) = \begin{cases} 1, & r_{ij} \leq R_{ij}, \\ \frac{1}{2} + \frac{1}{2}cos(\frac{\pi(r_{ij} - R_{ij})}{S_{ij} - R_{ij}}), & R_{ij} < r_{ij} < S_{ij}, \\ 0, & r_{ij} \geq S_{ij}. \end{cases} \tag{2.21}$$

In Eqs. (2.15)-(2.21), i, j, and k denote the atoms in the system, r_{ij} is the distance between atom i and j, and θ_{ijk} is the angle between the vectors r_{ij} and r_{ik}.

The function $V_r(r_{ij})$ represents a repulsive pair potential, while $V_a(r_{ij})$ represents an attractive one (Eq. (2.16)). The smooth cutoff function $f_c(r_{ij})$ presented in Eq. (2.21) is employed to limit the range of the potential, therefore, reduces the computational effort.

The functions a_{ij} and b_{ij} (Eq. (2.17)) represent a measure of the bond order and strength, which depend on the local environment.

The set of potential parameters is shown in Table 1 [68]. The parameters for Si-Si

TABLE 2.1: Parameters of the Ohira-Tersoff potential

i-*j*	Si-Si	H-H	Si-H, H-Si
A(eV)	1.8308×10^3	80.07	4.8733×10^2
B(eV)	4.7118×10^2	31.38	1.8470×10^2
λ(Å^{-1})	2.4799	4.2075	2.9117
μ(Å^{-1})	1.7322	1.7956	1.9898
R (Å)	2.70	1.10	1.85
S (Å)	3.00	1.7	2.05
χ	1.0	1.0	1.0485
ϵ	1.0	1.0	1.1027

i-*j*-*k*	Si-Si-Si	H-H-Si	Si-H-Si	H-Si-Si
σ(Å^{-1})	0.0	3.0	0.0	0.0
c	1.0039×10^5	0.0	1.0039×10^5	4.7762×10^5
d	16.217	1.0	16.217	6.3214×10^2
ω	1.0	4.0	0.0	0.6999
δ	0.0	0.0	0.0	0.0
β	1.1×10^{-6}	1.0	1.1×10^{-6}	1.0
n	0.78734	1.0	0.78734	1.0
h	-0.59825	-1.0	-0.59825	-1.0
m	1.0	1.6094	1.0	1.6094
i-*j*-*k*	Si-Si-H	H-H-H	Si-H-H	H-Si-H
σ(Å^{-1})	0.0	3.0	0.0	3.0
c	1.0039×10^5	0.0	1.0039×10^5	0.0
d	16.217	1.0	16.217	1.0
ω	1.5	4.0	0.4	4.0
δ	0.0	0.0	0.8512	0.0
β	1.1×10^{-6}	1.0	1.1×10^{-6}	1.0
n	0.78734	1.0	0.78734	1.0
h	-0.59825	-1.0	-0.59825	-1.0
m	1.0	1.6094	1.0	1.6094

interactions were defined by Tersoff [55, 69, 70], whereas the corresponding parameters for H-H, Si-H and the corresponding three-body interactions were derived from *ab initio* calculations (configuration interaction method), from another empirical interatomic potential for Si-H interactions proposed by Murty and Atwater [71], and from experimental measurements by Ohira and co-workers [59, 68, 72]. Table 2 shows the performance of the Ohira-Tersoff potential in describing the energies and structures of bulk *c-Si* and H-terminated Si(100)-(2×1).

TABLE 2.2: Comparison of the energies and structures of *c-Si* and H-terminated Si(100)-(2×1) predicted by the OT potential with experimental and *ab initio* results.

c-Si	OT	Experimental results [73]
Bulk cohesive energy (eV/atom)	4.6296	4.63
Lattice parameter (Å)	5.4320	5.43
H-terminated Si(100)-(2×1)	OT	*Ab initio* results [61]
Dimer bond length (Å)	2.44	2.4
H-Si-Si bond angle (^{0})	110.2	114.7

2.1.2 *Ab initio* molecular dynamics simulation

2.1.2.1 Why *ab initio* molecular dynamics?

As mentioned above, MD simulations require information on the interaction potential of the system. The calculation of the interatomic forces is one of the most important aspects of MD simulations. In classical MD simulations, these forces are computed from empirical models or force fields which have been parameterized from either experimental data or the results of *ab initio* calculations of small model systems. Classical MD simulations are therefore fast and employed to investigate systems with a large number of particles. Model potentials work perfectly for rare gases (K, Xe, He, Ne, and Ar). There are however some drawbacks of classical MD simulations, for instance, traditional force fields are not able to model chemical reactions because of the requirement of breaking and forming bonds. If we consider some systems with changed structures or chemical reactions, bond order potentials, such as Tersoff, Brenner, ReaxFF, etc. could be good choices. Nevertheless, if systems are chemically complex; *i.e.*, they contain many different atom or molecule types, there will be a myriad of different interatomic interactions that have to be parameterized. Furthermore, the empirical potentials or force fields might not describe well the chemical bonding processes occurring in those systems. Since the classical MD simulations do not explicitly take into account the electrons, they are not able to study some important and interesting physical and chemical properties of the systems. On the contrary, in *ab initio* molecular dynamics (AIMD) simulations, the forces acting on the nuclei are obtained directly from electronic structure calculations performed "on-the-fly" as the molecular dynamics trajectory is generated. This means that AIMD simulations do not rely on any adjustable parameters [74].

2.1.2.2 Adiabatic and Born-Oppenheimer approximations

The (non-relativistic) time-dependent Schrödinger equation of a many-body system consisting of N nuclei and N_e electrons is,

$$i\hbar\frac{\partial}{\partial t}\Phi(\{\mathbf{r}_i\},\{\mathbf{R}_I\};t) = H\Phi(\{\mathbf{r}_i\},\{\mathbf{R}_I\};t), \tag{2.22}$$

where H is the total Hamiltonian,

$$\begin{aligned} H &= -\sum_{I=1}^{N}\frac{\hbar^2}{2M_I}\nabla_I^2 - \sum_{i=1}^{N_e}\frac{\hbar^2}{2m_e}\nabla_i^2 + \frac{1}{4\pi\epsilon_0}\sum_{i<j}\frac{e^2}{|\mathbf{r}_i-\mathbf{r}_j|} - \frac{1}{4\pi\epsilon_0}\sum_{i,I}\frac{Z_Ie^2}{|\mathbf{R}_I-\mathbf{r}_i|} + \frac{1}{4\pi\epsilon_0}\sum_{I<J}\frac{Z_IZ_Je^2}{|\mathbf{R}_I-\mathbf{R}_J|} \\ &= -\sum_{I=1}^{N}\frac{\hbar^2}{2M_I}\nabla_I^2 - \sum_{i=1}^{N_e}\frac{\hbar^2}{2m_e}\nabla_i^2 + V_{n-e}(\{\mathbf{r}_i\},\{\mathbf{R}_I\}) \\ &= -\sum_{I=1}^{N}\frac{\hbar^2}{2M_I}\nabla_I^2 + H_e(\{\mathbf{r}_i\},\{\mathbf{R}_I\}). \end{aligned} \tag{2.23}$$

Here, $\{\mathbf{r}_i\}$ and $\{\mathbf{R}_I\}$ denote electronic and nuclear positions, M_I and Z_I are mass and atomic number of the Ith nucleus, m_e is the electron mass, ϵ_0 is the vacuum permittivity, and $H_e(\{\mathbf{r}_i\},\{\mathbf{R}_I\})$ is the electronic Hamiltonian.

Suppose that the set of solutions to the time-independent electronic Schrödinger equation,

$$H_e(\{\mathbf{r}_i\};\{\mathbf{R}_I\})\psi_k(\{\mathbf{r}_i\};\{\mathbf{R}_I\}) = E_k(\{\mathbf{R}_I\})\psi_k(\{\mathbf{r}_i\};\{\mathbf{R}_I\}), \tag{2.24}$$

is available. Here, the eigenvalues of H_e are assumed to be discrete and the eigenfunctions to be orthonormalized

$$\int \psi_k^*(\{\mathbf{r}_i\};\{\mathbf{R}_I\})\psi_l(\{\mathbf{r}_i\};\{\mathbf{R}_I\})d\mathbf{r} = \delta_{kl} \tag{2.25}$$

at all possible positions of the nuclei; $\int ...d\mathbf{r}$ refers to the integration over all variables $\{\mathbf{r}_i\} = \mathbf{r}$.

The total (exact) wave function can be expressed as an expansion in the complete set of electronic wave functions, with the time-dependent expansion coefficients being functions of the nuclear coordinates,

$$\Phi(\{\mathbf{r}_i\},\{\mathbf{R}_I\};t) = \sum_{l=0}^{\infty}\psi_l(\{\mathbf{r}_i\};\{\mathbf{R}_I\})\chi_l(\{\mathbf{R}_I\};t). \tag{2.26}$$

By inserting Eq. (2.26) into Eq. (2.22) then multiplying from the left by $\psi_k^*(\{\mathbf{r}_i\};\{\mathbf{R}_I\})$ and integrating over all electronic coordinates $\mathbf{r}$, a set of coupled differential equations is obtained,

$$\left[-\sum_I\frac{\hbar^2}{2M_I}\nabla_I^2 + E_k(\{\mathbf{R}_I\})\right]\chi_k + \sum_i C_{kl}\chi_l = i\hbar\frac{\partial}{\partial t}\chi_k \tag{2.27}$$

where

$$C_{kl} = \int \psi_k^* \left[-\sum_I \frac{\hbar^2}{2M_I} \nabla_I^2 \right] \psi_l d\mathbf{r} + \frac{1}{M_I} \sum_I \left\{ \int \psi_k^* [-i\hbar \nabla_I] \psi_l d\mathbf{r} \right\} [-i\hbar \nabla_I] \tag{2.28}$$

is the exact non-adiabatic coupling operator.

In the *adiabatic approximation* [75], the form of the total wave function is restricted to one electronic surface; *i.e.*, all coupling elements in Eq. (2.27) are neglected (only the terms with $l = k$ survive). Moreover, the second term of Eq. (2.28) is zero when the electronic wave function is real. These lead to complete decoupling of the set of coupled differential equations Eq. (2.27)

$$\left[-\sum_I \frac{\hbar^2}{2M_I} \nabla_I^2 + E_k(\{\mathbf{R}_I\}) + C_{kk}(\{\mathbf{R}_I\}) \right] \chi_k = i\hbar \frac{\partial}{\partial t} \chi_k \tag{2.29}$$

with

$$C_{kk} = -\sum_I \frac{\hbar^2}{2M_I} \int \psi_k^* \nabla_I^2 \psi_k d\mathbf{r}. \tag{2.30}$$

This implies that the motion of the nuclei occur without changing the quantum state, k, of the electronic subsystem during the time evolution. The total wave function in Eq. (2.22) can be decoupled simply into a direct product of an electronic and a nuclear wave function

$$\Phi(\{\mathbf{r}_i\}, \{\mathbf{R}_I\}; t) \approx \psi_k(\{\mathbf{r}_i\}; \{\mathbf{R}_I\}) \chi_k(\{\mathbf{R}_I\}; t). \tag{2.31}$$

The term $C_{kk}(\{\mathbf{R}_I\})$, known as the *diagonal correction*, represents a correction to the adiabatic eigenvalue $E_k(\{\mathbf{R}_I\})$ of the electronic Schrödinger equation Eq. (2.24) in this kth state. It is smaller than $E_k(\{\mathbf{R}_I\})$ by a factor roughly equal to the ratio of the electronic and nuclear masses. It is usually a slowly varying function of nuclear positions $\{\mathbf{R}_I\}$. The shape of the energy surface is therefore determined almost exclusively by $E_k(\{\mathbf{R}_I\})$. In the *Born-Oppenheimer* approximation, the diagonal correction is neglected, and Eq. (2.29) becomes

$$\left[-\sum_I \frac{\hbar^2}{2M_I} \nabla_I^2 + E_k(\{\mathbf{R}_I\}) \right] \chi_k = i\hbar \frac{\partial}{\partial t} \chi_k. \tag{2.32}$$

Eq. (2.32) has the usual form of Schrödinger equation where the electronic energy plays the role of a potential energy. In the *Born-Oppenheimer* approximation, the nuclei move according to classical mechanics in an effective potential which is given by the potential energy surface $E_k(\{\mathbf{R}_I\})$ obtained by solving the time-independent electronic Schrödinger equation for kth state at the given nuclear configuration $\{\mathbf{R}_I\}$. Moreover, the nuclei move much slower than the electrons due to their heavier masses. On the typical time scale of the nuclear motion, the electrons will very rapidly relax to their

instantaneous ground-state configuration. This means that electrons are always in their instantaneous ground-state for each given nuclear configuration $\{\mathbf{R}_I\}$.

Therefore, in the *Born-Oppenheimer* approximation, the motion of the nuclei can be treated classically on the ground-state electronic surface. The classical dynamics of the nuclei obey the equations of motion

$$M_I \ddot{\mathbf{R}}_I = -\nabla_I E_0(\{\mathbf{R}_I\}) \tag{2.33}$$

where $E_0(\{\mathbf{R}_I\})$ is deduced from the time-independent electronic Schrödinger equation in the ground-state

$$H_e(\{\mathbf{r}_i\};\{\mathbf{R}_I\})\psi_0(\{\mathbf{r}_i\};\{\mathbf{R}_I\}) = E_0(\{\mathbf{R}_I\})\psi_0(\{\mathbf{r}_i\};\{\mathbf{R}_I\}). \tag{2.34}$$

Here, $E_0(\{\mathbf{R}_I\})$ and $\psi_0(\{\mathbf{r}_i\},\{\mathbf{R}_I\})$ are the ground-state eigenvalue and eigenfunction of the electronic Schrödinger equation at the nuclear configuration $\{\mathbf{R}_I\}$, respectively. Eq. (2.34) cannot be solved exactly, therefore, it needs to be solved approximately. The electronic structure method most commonly used is the Kohn-Sham (KS) formulation of density functional theory (DFT).

2.1.2.3 Kohn-Sham density functional theory

The total ground-state energy of an interacting system of electrons at the nuclear configuration $\{\mathbf{R}_I\}$

$$E_{tot} = \min_{\psi_0}\{\langle\psi_0|H_e|\psi_0\rangle\} = \min_{\{\phi_i\}} E^{KS}[\{\phi_i\}] \tag{2.35}$$

can be obtained as the minimum of Kohn–Sham energy [76, 77]

$$E^{KS}[\{\phi_i\}] = T_S[\{\phi_i\}] + \int V_{ext}(\mathbf{r})n(\mathbf{r})d\mathbf{r} + \frac{1}{2}\int V_H(\mathbf{r})n(\mathbf{r})d\mathbf{r} + E_{xc}[n], \tag{2.36}$$

which is an explicit functional of the set of fictitious one-particle functions, the KS orbitals $\{\phi_i(\mathbf{r})\}$, that satisfy the orthonormal relation $\langle\phi_i|\phi_j\rangle = \delta_{ij}$. The orbitals are related to the electronic density or charge density $n(\mathbf{r})$ as follows

$$n(\mathbf{r}) = \sum_{i=1}^{N_{occ}} f_i|\phi_i(\mathbf{r})|^2 \tag{2.37}$$

where N_{occ} is the number of occupied orbitals and f_i is the occupation number of the ith orbital. N_{occ} and f_i satisfy the relation $\sum_{i=1}^{N_{occ}} f_i = N_e$.

The first term in the KS functional Eq. (2.36) is the kinetic energy of a non-interacting reference system

$$T_S[\{\phi_i\}] = \sum_{i=1}^{N_{occ}} f_i \left\langle \phi_i | -\frac{1}{2}\nabla^2 | \phi_i \right\rangle \tag{2.38}$$

including the same number of electrons exposed to the same external potential as in the fully interacting system.

The second term comes from the fixed external potential

$$V_{ext}(\mathbf{r}) = -\sum_I \frac{Z_I}{|\mathbf{R}_I - \mathbf{r}|} + \sum_{I<J} \frac{Z_I Z_J}{|\mathbf{R}_I - \mathbf{R}_J|} \tag{2.39}$$

in which the electrons move. This term contains the Coulomb interactions between electrons and nuclei and the internuclear Coulomb interactions.

The third term is the Hartree energy, *i.e.*, the classical electrostatic energy of two charge clouds which stem from the electronic density, and is obtained from the Hartree potential

$$V_H(\mathbf{r}) = \int \frac{n(\mathbf{r}')}{|\mathbf{r} - \mathbf{r}'|} d\mathbf{r}'. \tag{2.40}$$

The Hartree potential is related to the electronic density via Poisson's equation

$$\nabla^2 V_H(\mathbf{r}) = -4\pi n(\mathbf{r}). \tag{2.41}$$

The last term $E_{xc}[n]$ is the exchange-correlation energy functional. The exact form of $E_{xc}[n]$ is unknown and must be approximated. Approximation methods to the exact $E_{xc}[n]$ are available, for instance, Local Density Approximation (LDA), Generalized Gradient Approximation (GGA), hybrid functionals, Meta-GGA, etc. The quality of the electronic structure calculations relies on the quality of the approximation method chosen for $E_{xc}[n]$.

The minimum of the KS functional is obtained by varying the Eq. (2.36) for a fixed number of electrons with respect to the electronic density $n(\mathbf{r})$ or with respect to the orbitals subject to the holonomic orthonormality constraint. This leads to the KS equations

$$\left\{-\frac{1}{2}\nabla^2 + V_{ext}(\mathbf{r}) + V_H(\mathbf{r}) + \frac{\delta E_{xc}[n]}{\delta n(\mathbf{r})}\right\} \phi_i(\mathbf{r}) = \sum_j \Lambda_{ij}\phi_j(\mathbf{r}) \tag{2.42}$$

$$\left\{-\frac{1}{2}\nabla^2 + V^{KS}(\mathbf{r})\right\} \phi_i(\mathbf{r}) = \sum_j \Lambda_{ij}\phi_j(\mathbf{r}) \tag{2.43}$$

$$H_e^{KS}\phi_i(\mathbf{r}) = \sum_j \Lambda_{ij}\phi_j(\mathbf{r}), \tag{2.44}$$

where $\dfrac{\delta E_{xc}[n]}{\delta n(\mathbf{r})} = V_{xc}[n]$ is the exchange-correlation potential, $V^{KS}(\mathbf{r})$ and H_e^{KS} are the effective one-particle potential and Hamiltonian, respectively. A unitary transformation within the space of the occupied orbitals leads to the diagonal canonical form of the KS equations

$$H_e^{KS}\phi_i(\mathbf{r}) = \epsilon_i\phi_i(\mathbf{r}) \tag{2.45}$$

where ϵ_i is the KS eigenvalue of state i.

2.1.2.4 Born-Oppenheimer molecular dynamics

Numerous AIMD approaches are available. Among them, two fundamental methods employed in almost AIMD simulation packages are Born-Oppenheimer MD (BOMD) and Car-Parrinello MD (CPMD). VASP uses the BOMD approach.

In the BOMD [74], the time-independent electronic Schrödinger equation in the ground-state Eq. (2.34) is solved in each MD step for a given nuclear configuration $\{\mathbf{R}_I\}$ at that instant of time. Then the forces acting on the nuclei are computed according to the equations of motion Eq. (2.33) from the potential energy $E_0(\{\mathbf{R}_I\})$ which is the total electronic energy in the ground-state.

We assume that the potential energy $E_0(\{\mathbf{R}_I\})$ is calculated using DFT. Therefore, the KS functional $E^{KS}(\{\phi_i\})$ is minimized at each MD step with respect to the KS orbitals $\{\phi_i(\mathbf{r})\}$ under the holonomic orthonormality constraint $\langle\phi_i|\phi_j\rangle$. This leads to the following Lagrangian:

$$L_{BO} = \frac{1}{2}\sum_{I=1}^{N} M_I\dot{\mathbf{R}}_I^2 - \min_{\{\phi_i\}} E^{KS}[\{\phi_i\}] + \sum_{i,j}\Lambda_{ij}(\langle\phi_i|\phi_j\rangle - \delta_{ij}) \tag{2.46}$$

where Λ is a Hermitian Lagrangian multiplier matrix. By solving the corresponding Euler-Lagrange equations for both the nuclear positions and the KS orbitals

$$\frac{d}{dt}\frac{\partial L}{\partial \dot{\mathbf{R}}_I} = \frac{\partial L}{\partial \mathbf{R}_I}, \tag{2.47}$$

$$\frac{d}{dt}\frac{\partial L}{\partial \langle\dot{\phi}_i|} = \frac{\partial L}{\partial \langle\phi_i|}, \tag{2.48}$$

we obtain the associated equations of motion

$$M_I\ddot{\mathbf{R}}_I = -\nabla_I\left[\min_{\{\phi_i\}} E^{KS}[\{\phi_i\}]|_{\{\langle\phi_i|\phi_j\rangle=\delta_{ij}\}}\right], \tag{2.49}$$

$$H_e^{KS}\phi_i(\mathbf{r}) = \sum_j \Lambda_{ij}\phi_j(\mathbf{r}) \; or \; H_e^{KS}\phi_i(\mathbf{r}) = \epsilon_i\phi_i(\mathbf{r}). \tag{2.50}$$

To sum up, in the BOMD the electronic and nuclear systems are fully decoupled. As a consequence, the electronic structure problem has to be solved self-consistently at each MD step. The total electronic energy needs to be minimal at each MD step in order to estimate the forces acting on the nuclei. The equations of motion of the nuclei can be integrated on the time scale given by nuclear motion, thus allows us to use a relatively large MD time step (up to the nuclear resonance limit). This holds irrespective of the band gap; *i.e.*, the BOMD also works in the case where the band gap is zero. In principle, even metals can be straightforwardly treated.

2.1.2.5 *Ab initio* forces: the Hellmann-Feynman theorem

The most time-consuming part of almost MD simulations is the calculation of the forces acting on the nuclei. A straightforward numerical evaluation of these forces

$$F_I = -\nabla_I \langle \psi_0 | H_e | \psi_0 \rangle \tag{2.51}$$

by a finite-difference approximation of the total electronic energy is too costly and inaccurate for dynamical simulations. The derivative on the right-hand-side (RHS) of Eq. (2.51) can be evaluated analytically

$$\nabla_I \langle \psi_0 | H_e | \psi_0 \rangle = \langle \psi_0 \nabla_I | H_e | \psi_0 \rangle + \langle \psi_0 | \nabla_I H_e | \psi_0 \rangle + \langle \psi_0 | H_e | \nabla_I \psi_0 \rangle \, . \tag{2.52}$$

The first and third terms on the RHS of Eq. (2.52) vanish if the wave function is an exact eigenfunction (or stationary state wave function) of the particular Hamiltonian under consideration. This is known as the Hellmann-Feynman theorem (HFT) [78]

$$F_I^{HFT} = - \langle \psi_0 | \nabla_I H_e | \psi_0 \rangle \tag{2.53}$$

which is also valid for many vibrational wave functions (for example, the Hartree-Fock wave function) provided that complete basis sets are used. If this is not the case, there are additional terms to be considered

$$F_I = F_I^{HFT} + F_I^{IBS} + F_I^{NSC}. \tag{2.54}$$

The first term in Eq. (2.54) is the force computed according to the HFT. The second term is Pulay or wave function force stemming from the incompleteness of the basis sets used. It vanishes in the case of complete basis sets, or in the case of originless basis functions, such as plane waves. The last term is the non-self-consistency force arising in case exact self-consistency is not achieved.

2.2 Methods to "measure" system properties

Molecular dynamics simulations save phase-space trajectories of all particles in the system. We are, nevertheless, interested in the physical (*i.e.*, structural, thermal, and dynamics) properties of the system. This section presents methods to "measure" system properties from MD simulation data. Subsection 2.2.1 discusses the method to determine the cluster temperature used to study the heating of hydrogenated silicon clusters due to reactions with atomic hydrogen. To analyze the structure characteristics of the systems, for instance, clusters during the hydrogen exposure, cluster-damaged silicon surfaces before and after the hydrogen treatment, and clusters before and after the substrate impact; we calculate the radial distribution function. The definition of this function will be presented in the subsection 2.2.2. The solid-liquid phase transition of hydrogenated silicon clusters due to reactions with H-atoms is evaluated by the self-diffusion coefficient of silicon atoms of the clusters. This quantity can be deduced from either the mean-square displacement using the Einstein relation or the velocity autocorrelation function using the Green-Kubo relation [79]. For classical systems, both relations are strictly equivalent. In this work, we have investigated the mean-square displacement to calculate the self-diffusion coefficient. The mean-square displacement is also used to study the phase states of clusters after the surface impact necessary to discover the mystery of the cluster-catalyzed epitaxial growth of silicon thin films. Subsection 2.2.3 is devoted to present the mean-square displacement.

2.2.1 Cluster temperature

To determine the cluster temperature, we first eliminate the translational motion; *i.e.*, we subtract the cluster's center-of-mass (COM) velocity from all cluster particles. We then separate the energy of the "internal" (vibrational) motion from that of the overall rotation based on the scheme proposed by Jellinek and Li [80, 81]. In the COM coordinate system of the cluster, the total angular momentum $\mathbf{L}$ of the cluster is defined as follows

$$\mathbf{L} = \sum_{i=1}^{N} \mathbf{r}_i \times \mathbf{p}_i \tag{2.55}$$

where the sum is calculated over all cluster particles $N, \mathbf{r}_i$ is the position vector of the particle i in the COM coordinate system of the cluster, and $\mathbf{p}_i$ is the momentum of the particle i after correction for the COM velocity of the cluster.

Alternatively, the total angular momentum $\mathbf{L}$ can be expressed in terms of the instantaneous angular velocity vector ω and the instantaneous tensor of inertia $\mathbf{I}$ in the

COM coordinate system of the cluster

$$\mathbf{L} = \mathbf{I} \cdot \omega. \tag{2.56}$$

The instantaneous tensor of inertia **I** in Eq. (2.56) is a 3×3 matrix with matrix elements

$$\mathbf{I}_{\alpha\alpha} = \sum_{i=1}^{N} m_i(r_i^2 - \alpha_i^2), \mathbf{I}_{\alpha\beta} = -\sum_{i=1}^{N} m_i \alpha_i \beta_i \tag{2.57}$$

with $\alpha_i \neq \beta_i$ and $\alpha_i, \beta_i = x_i, y_i, z_i$ in the COM coordinate system of the cluster.

From Eq. (2.56) and (2.57), we can thus determine the instantaneous angular velocity vector ω of the cluster, consequently, its instantaneous rotational kinetic energy

$$E_{rot} = \frac{1}{2}\omega \cdot \mathbf{L}. \tag{2.58}$$

Defining the total kinetic energy of the cluster as

$$E_{kin} = \sum_{i=1}^{N} \frac{p_i^2}{2m_i}, \tag{2.59}$$

we can find the vibrational kinetic energy

$$E_{vib} = E_{kin} - E_{rot}. \tag{2.60}$$

The vibrational cluster temperature, so called 'cluster temperature', is then obtained from the time resolved average vibrational kinetic energy over a large number of time-steps

$$T = \frac{2\langle E_{vib}\rangle}{(3N-6)\,k_B} \tag{2.61}$$

where k_B is the Boltzmann constant.

2.2.2 Radial distribution function

The radial distribution function (RDF) gives the probability of finding a pair of atoms with an interatomic distance in comparison with the probability expected for a completely random distribution at the same density. Using the RDF is an efficient way to characterize the structure of crystalline, amorphous, and liquid systems. In addition, this function can be also deduced experimentally from neutron or X-ray diffraction studies. Therefore, calculation of RDF has been implemented in this work to verify the structure of the clusters during the hydrogen exposure, the cluster-damaged silicon surfaces before and after the hydrogen treatment, and the clusters before and after the

substrate impact. The expression to calculate RDF is described as follows [82, 83]

$$g(r) = \frac{n(r, \Delta r)}{\rho N \tau_{run} 4\pi r^2 \Delta r}, \tag{2.62}$$

in which $g(r)$ is the RDF, $n(r, \Delta r)$ is the average number of atoms in a shell of width Δr at distance r, ρ is the average atom density, N is the total number of atoms, and τ_{run} is the number of steps selected to calculate the RDF.

2.2.3 Mean-square displacement

The mean-square displacement (MSD) is a measure of the average square distance that a given particle in a system travels over a time interval. The MSD is defined as [84]

$$MSD(t) = \frac{1}{N} \left\langle \sum_{i=1}^{N} [\mathbf{r}_i(t_0 + t) - \mathbf{r}_i(t_0)]^2 \right\rangle \tag{2.63}$$

where $\mathbf{r}_i(t)$ denotes the position of particle i in the COM system at time t, N is the number of particles. The MSD contains information on the diffusion of particles. If the system is in the solid state, the MSD saturates to a finite value. However, if the system is in the liquid state, the MSD grows linearly with time. We can thus distinguish between solid and liquid phases of the system by looking at the behavior of the MSD. The slope of the MSD is related with the self-diffusion coefficient D by Einstein relation [85]

$$D = \frac{1}{6} \frac{d}{dt} (MSD(t)). \tag{2.64}$$

We have calculated the MSD to investigate the phase states of the hydrogenated silicon clusters during the hydrogen exposure to show their solid-liquid phase transition. The MSD was also employed to determine the phase states of the clusters after the surface impact, which is helpful to study the cluster-catalyzed epitaxial growth of silicon thin films.

Chapter 3

Heating and melting of plasma-born hydrogenated silicon clusters by reactions with atomic hydrogen

Abstract *Ab initio* molecular dynamics simulations have been carried out to investigate quantitatively the "realistic" heating and melting processes of plasma-born hydrogenated silicon clusters due to the reactions with atomic hydrogen in a plasma reactor. For H-exposure processes, we have chosen one hydrogenated amorphous silicon cluster ($Si_{15}H_{10}$) and the 1 nm hydrogenated silicon nanocrystal $Si_{29}H_{24}$. Our results indicate that the energies resulting from one H-atom reaction are about the same for both the amorphous and the initially crystalline clusters before the clusters start undergoing their structural transition from the solid to the liquid state. We show that the melting temperature of the $Si_{29}H_{24}$ nanocrystal is between 1621 and 1668 K and that its complete phase transition takes about 15 ps after the melting temperature is reached.

3.1 Introduction

Polymorphous hydrogenated silicon (*pm-Si:H*) thin films produced by plasma enhanced chemical vapor deposition (PECVD) largely improve the performance of solar cells, LEDs, and transistors over those based on amorphous silicon materials. Hydrogenated silicon nanocrystals embedded in an amorphous silicon matrix are thought to be responsible for this improvement [86]. It was shown that the synthesis of those silicon

nanocrystals/nanoparticles is taking place in the gas phase of the plasma, not on the substrate itself [87]; and that their size can be controlled with a quite narrow size dispersion by varying the plasma on-time of square-wave-modulated silane plasmas [22].

The formation processes of these hydrogenated silicon nanoparticles were "visualized" at atomic scale by means of semi-empirical molecular dynamics simulations [24, 25]. First, the experimentally employed silane plasma is characterized by a fluid dynamics model [26, 88]. The fluid model calculations provide information about relative densities of all plasma species, their temperatures, the energy distribution of the reactive species, mean free path lengths, and time intervals between chemical reactions. For a H_2/SiH_4 discharge, it is demonstrated that atomic hydrogen and SiH_3 radicals are the dominant dissociation products; however, hydrogen and silane molecules are still the major plasma species. Namely, the density of SiH_4 molecules is about 50 times smaller than that of molecular hydrogen, but about 1000 times greater than that of SiH_3 and 10 times greater than that of atomic hydrogen. In addition, all reactive species are found to have a room temperature energy distribution. This distribution can be described as a Maxwell-Boltzmann distribution function at room temperature. Based on those results of fluid model, the growth process of hydrogenated silicon clusters are hence started by the reaction between a SiH_4 molecule and a SiH_3 radical. Thereafter, the continuation of the cluster growth is simulated by the impact with additional SiH_4 molecules. All of the formed clusters exhibit amorphous structures, very rich in hydrogen with the hydrogen atoms always on top of the cluster surfaces.

The crystallization of amorphous hydrogenated silicon clusters by the reactions with hydrogen atoms was also shown in molecular dynamics simulations [24, 27, 28, 89] and later confirmed in experiments [22]. The interaction with atomic hydrogen leads to cluster heating while the collision with hydrogen molecules cools the cluster down. The simulations performed in Ref. [24] reveal that by changing the impinging H-atom flow rates while keeping the same number of hydrogen molecules, we can control the structure of the growing hydrogenated silicon clusters. The hydrogen-treated clusters can evolve to crystalline structures with relatively low H impact rates. For very high H impact rates, however, the clusters can melt since the clusters do not have sufficient time to cool down between two subsequent collisions with hydrogen atoms.

The interaction of the cluster with H-atoms leads to cluster heating that is necessary for the cluster to overcome energy barriers to more stable structures. Moreover, depending on the H impact flux rates and cooling down rates of clusters by the collisions with hydrogen molecules, they can become either amorphous or crystalline. The present study has been dedicated to investigate quantitatively how atomic hydrogen heats up plasma-born hydrogenated silicon nanoparticles necessary for their melting and crystallization before their deposition on the silicon substrate.

3.2 Computational details

In our investigation, we have chosen an amorphous hydrogenated silicon cluster ($Si_{15}H_{10}$) and the 1 nm hydrogenated silicon nanocrystal $Si_{29}H_{24}$ for the hydrogen exposure processes. The $Si_{15}H_{10}$ cluster was formed in a cluster growth process under plasma conditions presented in Ref. [25]. The $Si_{29}H_{24}$ nanoparticle experimentally produced from the dispersion of bulk silicon by lateral electrochemical etching exhibits a crystalline structure and outstanding optical properties [90–94]. We chose here the $Si_{29}H_{24}$ nanoparticle as a model for crystalline nanoparticles generated in plasma reactors. These clusters are optimized to their minimum energy structures. Figure 3.1 presents the corresponding configurations. Thereafter, the clusters are heated up to room temperature using a quasi-canonical ensemble process. The clusters are then thermalized for 5 ps (for $Si_{15}H_{10}$) and 15 ps (for $Si_{29}H_{24}$) in the microcanonical ensemble.

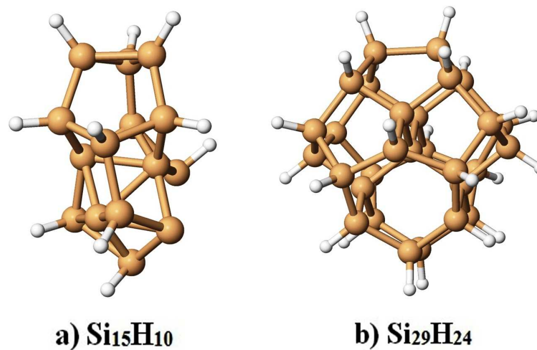

FIGURE 3.1: The initial configuration of the hydrogenated silicon clusters. The large brown spheres represent silicon atoms while the small white ones represent hydrogen atoms.

For the heating process, we consider a pure hydrogen plasma with a high concentration of H-atoms. To this end, hydrogen atoms are sent to the clusters, one after the other, with an impact energy of 0.025 eV (*i.e.*, with a velocity of 2225 m/s) corresponding to a Maxwell-Boltzmann distribution at room temperature [88]. Each hydrogen-cluster reaction is calculated in the microcanonical ensemble and followed for 10 ps after the reaction took place in the case of $Si_{15}H_{10}$ and 30 ps in the case of $Si_{29}H_{24}$.

All of our calculations have been carried out with the *ab initio* molecular dynamics simulations package VASP [44–46] using density functional theory (DFT) in the generalized gradient approximation (GGA) and with the projector-augmented wave (PAW) method [46]. Molecular dynamics simulations are performed using the Verlet algorithm with a time step of 1.0 fs.

To determine the cluster temperature after each reaction with atomic hydrogen, we have developed a program to separate the translational, rotational, and vibrational kinetic energies of a cluster based on the scheme proposed by Jellinek and Li [80, 81]. The

cluster temperature is calculated from the average vibrational kinetic energy

$$T = \frac{2\left\langle E_{vib}\right\rangle}{(3N-6)\,k_B} \tag{3.1}$$

where N is the number of cluster atoms, k_B is the Boltzmann constant.

To analyze the structure characteristics of the clusters during the hydrogen treatment process, we have calculated their radial distribution functions (RDFs). The RDF gives the probability of finding a pair of atoms with an interatomic distance in comparison with the probability expected for a completely random distribution at the same density. The expression to calculate RDF is described as follows [82, 83]

$$g(r) = \frac{n(r,\Delta r)}{\rho N \tau_{run} 4\pi r^2 \Delta r}, \tag{3.2}$$

in which $g(r)$ is the RDF, $n(r,\Delta r)$ is the average number of atoms in a shell of width Δr at distance r, ρ is the average atom density, N is the total number of atoms, and τ_{run} is the number of steps selected to calculate the RDF.

In order to determine phase states of the clusters during the H-exposure process, we have also investigated the behavior of the mean-square displacement (MSD) defined as [84]

$$MSD(t) = \frac{1}{N}\left\langle \sum_{i=1}^{N}[\mathbf{r}_i(t_0+t)-\mathbf{r}_i(t_0)]^2 \right\rangle \tag{3.3}$$

where $\mathbf{r}_i(t)$ denotes the position of atom i at time t, N is the number of atoms.

From the slope of the MSD, we can calculate the self-diffusion coefficient [85]

$$D = \frac{1}{6}\frac{d}{dt}(MSD(t)). \tag{3.4}$$

All of the average values are calculated over the last 5 or 15 ps of each trajectory for $Si_{15}H_{10}$ and for $Si_{29}H_{24}$, respectively.

3.3 Results and Discussions

3.3.1 Hydrogen-induced heating of hydrogenated silicon nanoparticles

3.3.1.1 $Si_{15}H_{10} + nH$

Figure 3.2a shows a heating process of the $Si_{15}H_{10}$ cluster while it adsorbs atomic hydrogen. The cluster is heated rapidly (about 330-400 K for each reaction) during the first three reactions with H-atoms. Thereafter, the cluster temperature increases more slowly, namely, about 190 K for the fourth reaction and only about 60 K for the fifth

H-atom to reach 1704 K. Therefore, we suggest that the $Si_{15}H_{10}$ might melt and undergo a phase transition to the liquid state at a temperature between 1450 and 1704 K because most of the energy which the cluster gains from the fourth and fifth reactions with H-atoms are probably employed to carry out structural changes and only a small part of the reaction energies are used to heat the cluster up further.

As a result of the H adsorption, there are more and more silicon hydrides (SiH_2 and SiH_3) formed on the cluster surface because of hydrogen diffusion. Those silicon hydrides are weakly bound on the cluster surface. In some trajectories, one SiH_4 molecule desorbs from the surface of $Si_{15}H_{16}$ cluster typically after the reaction with six H-atoms. The remaining $Si_{14}H_{12}$ cluster rearranges its structure and ends up with a final temperature of 1903 K.

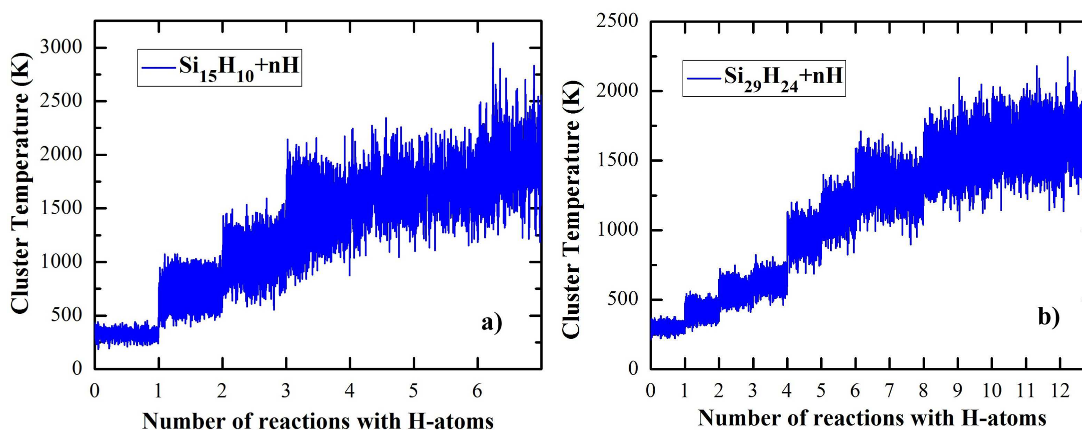

FIGURE 3.2: The evolution of the instantaneous temperature of clusters with the number n of reactions with H-atoms: a) $Si_{15}H_{10}$; b) $Si_{29}H_{24}$.

3.3.1.2 $Si_{29}H_{24}$ + nH

During the H-exposure process, the cluster temperature rapidly increases during the first six H-atom adsorption reactions following a staircase function with numbers of reactions with H-atoms (see Fig. 3.2b for a typical and representative reaction dynamics). In the shown example, the seventh reaction with a H-atom leads to the etching of one SiH_4 molecule from the cluster surface. As a result, the cluster temperature slightly decreases (from 1343 to 1288 K). The remaining $Si_{28}H_{27}$ cluster then adsorbs one H-atom and heats again to 1507 K. Thereafter, we have observed a slowly increasing cluster temperature from the eighth to the 12th reaction with H-atoms (from 1507 to 1668 K). This range of temperature is near the melting point of bulk silicon. Therefore, we suppose that there is a structural transition from the solid to the liquid state.

We calculated the average cluster temperature increase for each reaction during the

first three H-atom reactions for $Si_{15}H_{10}$ and during the first six H-atom reactions for $Si_{29}H_{24}$. Those values are about 375 and 186 K for $Si_{15}H_{10}$ and for $Si_{29}H_{24}$, respectively. The ratio between those values is inversely proportional to the cluster masses. This implies that the average energy resulting from each H-atom reaction is about the same for both the amorphous and the initially crystalline clusters according to thermodynamics before the clusters start undergoing their structural transition from the solid to the liquid state.

3.3.2 Melting dynamics

The RDFs were investigated to examine how the atomic hydrogen damages the structure of the clusters. The RDFs of the $Si_{15}H_{10}$ cluster after each H-atom reaction (Fig. 3.3a) show that the second peak is less pronounced indicating that the structure of the $Si_{15}H_{10}$ cluster becomes more and more disordered as the cluster is heated up.

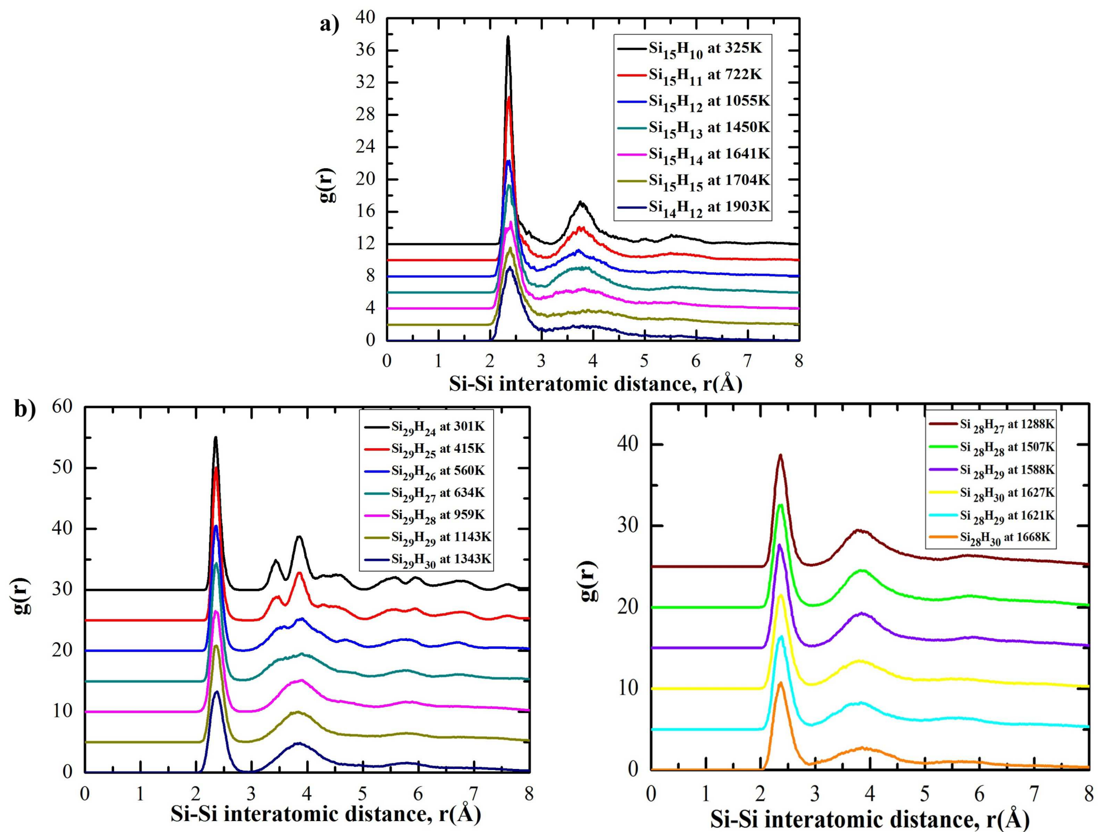

FIGURE 3.3: The RDFs of the clusters during the heating processes induced by the subsequent reactions with H-atoms: a) $Si_{15}H_{10}$; b) $Si_{29}H_{24}$.

The RDFs of $Si_{29}H_{24}$ cluster show that after two reactions with H-atoms, the cluster remains in its crystalline structure because the features of the second and third peak are still clearly distinguishable. After the reaction with the fifth H-atom, however, the

second peak entirely disappeared. The peak at 3.85 Å becomes broader duringthe H-induced cluster heating because of the less well defined cluster geometry.

From the RDFs, we can observe how the cluster structures change due to the hydrogen-induced heating. However, to further distinguish between solid and liquid phases of our clusters, we also consulted the MSD of silicon atoms of the clusters at different equilibrated temperatures after the H-atom reactions (Fig. 3.4). The MSD at 722 K (after the first reaction) exhibits a solid-like behavior. The MSD graphs for the intermediate temperatures at 1055 and 1450 K mark the onset of the phase transition to the liquid state. After the fourth, fifth, and sixth H-atom reactions, the MSDs clearly indicate a liquid state. The ballistic regimes in the MSD graphs of both the $Si_{15}H_{14}$ cluster at 1641 K and the $Si_{15}H_{15}$ cluster at 1704 K last about 0.25 ps and are directly followed by diffusive regimes. On the other hand, for the $Si_{14}H_{12}$ cluster at 1903 K, the silicon atoms are in the ballistic regime only up to about 0.1 ps suggesting a less stable cluster configuration.

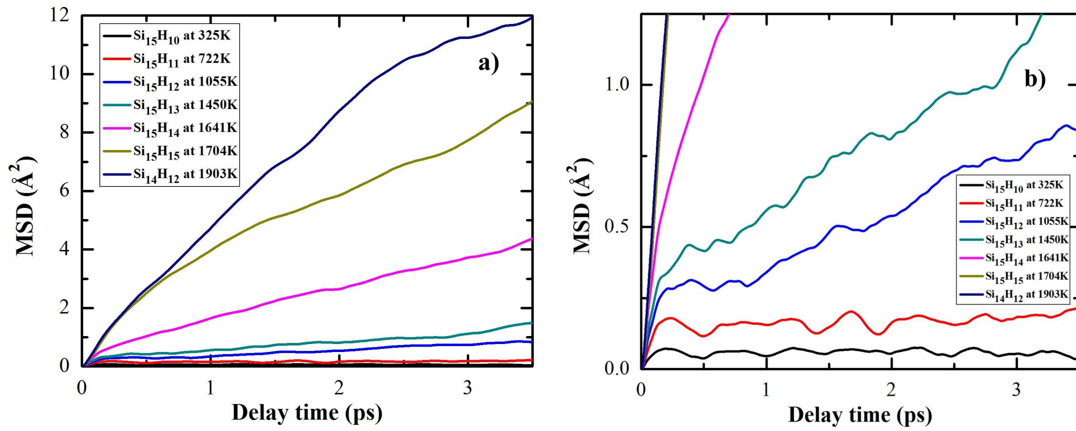

FIGURE 3.4: a) MSD of silicon atoms of the $Si_{15}H_{10}$ cluster at different temperatures due to the subsequent reactions with H-atoms; b) a zoom to show the details of the MSD graphs.

The MSD graphs for $Si_{29}H_{24}$ shown in Fig. 3.5a and b indicate that the $Si_{29}H_{24}$ cluster clearly remains in the solid state although it heated up to 1507 K due to its reaction with eight H-atoms. Continuing the hydrogen exposure process, we have observed the on-set of the structural transition to the liquid state after the reaction with the 11th H-atom yielding a cluster temperature of about 1621 K. The cluster completes its phase transition to the liquid state after the reaction with the 12th hydrogen atom as can be concluded from the liquid-like behavior shown in the MSD graph; *i.e.*, the silicon atoms of the cluster are in the ballistic regime for about 0.2 ps and enter the diffusive regime of the liquid state thereafter.

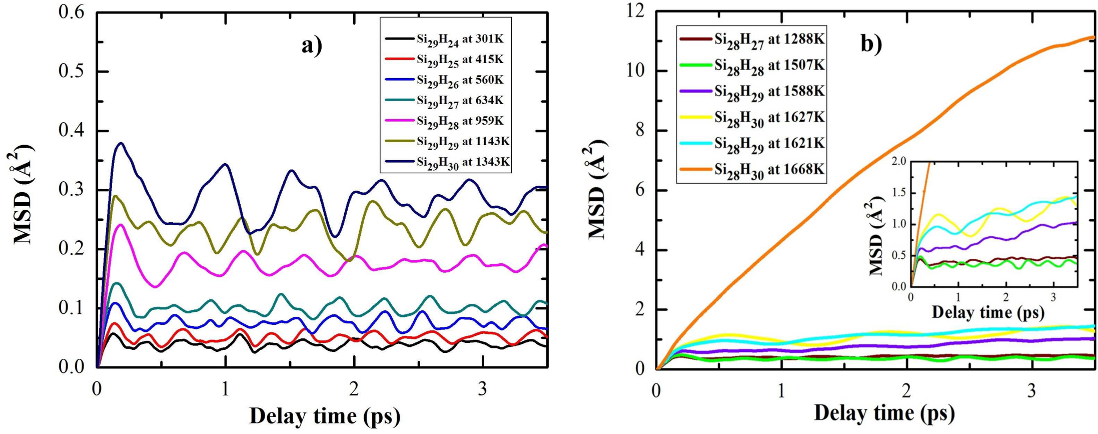

FIGURE 3.5: MSD of silicon atoms of the $Si_{29}H_{24}$ cluster at different temperatures due to the subsequent reactions with H-atoms: a) first six reactions with H-atoms; b) last six reactions with H-atoms.

Interestingly enough, we have observed a slight decrease in cluster temperature about 15 ps after the $Si_{29}H_{24}$ cluster reacted with the 12th H-atom. Right after the reaction, the cluster temperature reached 1813 K, then it slowly decreased and finally equilibrated at 1668 K. We have investigated the MSD graphs of the silicon atoms of the cluster directly after it reacted with the 12th H-atom (Fig. 3.6b) and after it equilibrated (Fig. 3.6c). The MSD graph right after the reaction with the 12th H-atom exhibits the same slope as the one of the MSD graph after the 11th H-atom reaction. It means that the cluster is still at an intermediate state before the complete change to the liquid-like state is achieved. The MSD graph after the cluster equilibrated at 1668 K, however, clearly shows a liquid-like behavior. This indicates that the phase transition is only completed about 15 ps after the $Si_{29}H_{24}$ cluster reacted with the 12th H-atom. During this process, the cluster gained the reaction energy to make a structural transition to a less stable state. Therefore, we have seen above that the temperature decreased slightly.

Figure 3.7a shows that the self-diffusion coefficients of silicon atoms of the $Si_{15}H_{10}$ cluster increase with temperature. Those coefficients are extracted from the slopes of the MSD graphs in the diffusive regime at different temperatures of the H-treatment process. There is a slight increase of the self-diffusion coefficients from 1055 to 1450 K, while a rapid increase is observed between 1450 and 1704 K. In fact, the self-diffusion coefficient at 1704 K is about six times larger than at 1450 K. The self-diffusion coefficient is about 0.67 $\mathring{A}^2$/ps at 1903 K. This value is quite comparable to the one obtained by Zachariah *et al.* [95] especially considering that his 480-silicon atom cluster is much larger than ours and that his temperature is yet higher than ours. Using classical molecular dynamics simulations with the three-body Stillinger-Weber interatomic potential, they determined the self-diffusion coefficient to be 1.05 $\mathring{A}^2$/ps at 2000 K and concluded that their cluster is in the liquid state. Therefore, we suggest that our H-treated $Si_{15}H_{10}$ cluster at 1903

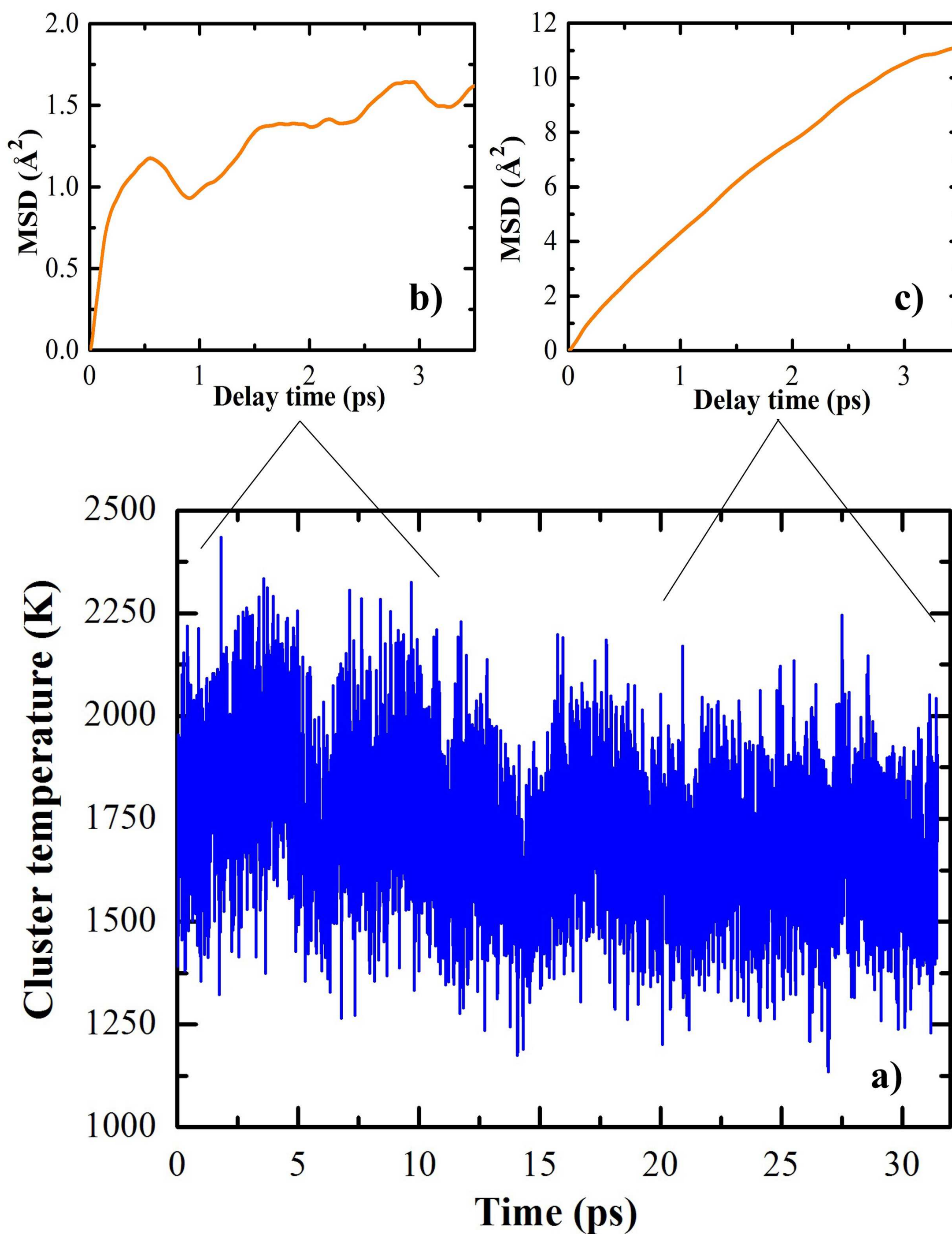

FIGURE 3.6: a) Time evolution of the instantaneous temperature of the $Si_{29}H_{24}$ cluster after the reaction with the 12th H-atom for the chosen typical example; b) The MSD of silicon atoms of the cluster right after the reaction with the 12th H-atom at a temperature of 1813 K; c) The MSD of silicon atoms of the cluster after it equilibrated to 1668 K.

K is also in the liquid state and that there is a structural transition from the solid to the liquid state in the temperature region between 1450 and 1704 K. The self-diffusion coefficients for the $Si_{29}H_{24}$ cluster at different temperatures of the H-exposure process exhibit a very rapid increase (by a factor of about 15) from 0.036 Å^2/ps to 0.53 Å^2/ps in a very narrow temperature region (1621-1668 K) suggesting a structure change to the liquid state resulting from the reaction with the 12th H-atom (see Fig. 3.7b).

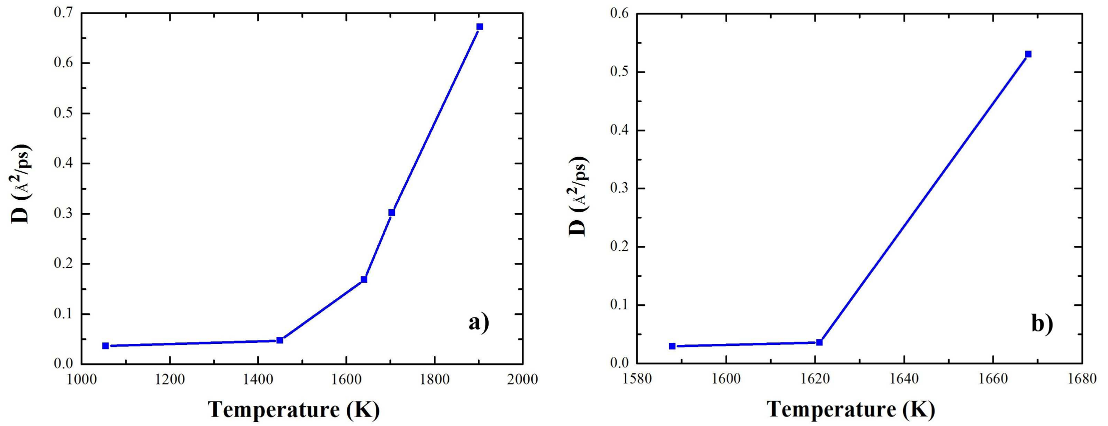

FIGURE 3.7: Self-diffusion coefficients of silicon atoms of the two considered clusters at different temperatures resulting from the subsequent hydrogen exposure reactions: a) $Si_{15}H_{10}$; b) $Si_{29}H_{24}$.

The self-diffusion coefficients of the H-treated $Si_{15}H_{10}$ and $Si_{29}H_{24}$ clusters are about 0.17Å^2/ps at 1641 K and 0.53 Å^2/ps at 1668 K, respectively. Those values are smaller than the self-diffusion coefficient of bulk silicon at the melting point (2.52 Å^2/ps at 1687 K) obtained from experiments [96, 97]. This difference is in agreement with previous studies about the melting characterizations of pure and hydrogenated silicon nanoparticles [95, 98, 99]. The self-diffusion coefficients for pure and hydrogenated silicon nanoparticles investigated in those references are always considerable smaller than that of bulk silicon at comparable temperatures. Tentatively, we suggest that the observed difference in self-diffusion coefficients for bulk and nanocrystalline silicon can be traced back to the relative number of core and surface atoms. While the core silicon atoms behave fairly like bulk silicon, the surface silicon atoms exhibit different properties. Zachariah *et al.* [95] had examined a 480-silicon atom cluster over the temperature range from 600 to 2000 K. The authors found that the surface atoms are three to four times coordinated over the studied temperature range, while the coordination number of core atoms is around 5 at temperatures up to 1600 K and 8.49 at 2060 K. For a given temperature, the mean bond length of the cluster increases with coordination number due to partial electron deficiency. Consequently, core atoms have larger mean bond lengths than surface atoms. This indicates that the Si-Si bonding in the core is weaker than at the surface, facilitating the diffusion and thus increasing the self-diffusion coefficient. Our

$Si_{15}H_{10}$ cluster has no core silicon atoms and $Si_{29}H_{24}$ nanocrystal has only one. Therefore, the self-diffusion coefficients of our clusters at a given temperature are smaller than those of bigger silicon nanoparticles [95, 98, 99] and bulk silicon [100].

Some previous work concerning the melting behavior of small silicon clusters [101, 102] (from 7 to 21 silicon atoms) has investigated the melting temperature as a function of cluster size. They have found that the melting temperature of small silicon clusters does not exhibit a clear trend with cluster size; *i.e.*, some sizes (for instance, 7, 12, 15 silicon atoms) are more stable, and exhibit thus higher melting temperatures than other sizes. The authors [102] used canonical Metropolis Monte Carlo simulations to study the thermal behavior of silicon clusters and calculated the bond length root-mean-square fluctuation to characterize the melting behavior of those clusters. They have found that the melting temperature of a 15-silicon atom cluster with a layered stack structure is about 1350 K and that this cluster started melting from about 1250 K and was fully melted at about 1500 K. In our work, according to the evolution of the cluster temperature and the self-diffusion coefficients with the number of reactions with H-atoms, we conclude that the $Si_{15}H_{10}$ cluster starts to melt from 1450 K (after three reactions with H-atoms) and becomes totally liquid at about 1704 K (after five reactions with H-atoms). Looking back at Fig. 3.2a, the $Si_{15}H_{10}$ cluster temperature significantly increases during the first three H-atom reactions. It remains nearly constant during the fourth and the fifth reaction where the cluster undergoes its phase transition. Thereafter, additional reactions with H-atom heat the liquid silicon cluster further.

3.4 Conclusions

In the present work, the hydrogen-induced heating and the phase transition from crystalline to amorphous and solid to liquid states as well as the on-set for etching of plasma-born hydrogenated silicon nanoparticles have been investigated quantitatively for the first time. Contrary to previous studies concerning the phase transition dynamics of pure or hydrogenated silicon nanoparticles, we considered here cluster heating induced by reactions with H-atoms as in a realistic plasma reactor instead of using “artificial” velocity scaling.

The results indicate that the average energy resulting from each H-atom reaction is about the same for both the amorphous and the initially crystalline clusters before the clusters start undergoing their structural transition from the solid to the liquid state. The evolution of the cluster temperature as well as the self-diffusion coefficients with the number of reactions with H-atoms suggest that the clusters undergo the solid to liquid phase transition in the temperature regions from 1450 to 1704 K in the case of $Si_{15}H_{10}$ and from 1621 to 1668 K in the case of $Si_{29}H_{24}$. At those temperature regions,

the cluster temperature slowly increases, while the self-diffusion coefficients significantly augment. In a typical example, we have observed the melting dynamics of the $Si_{29}H_{24}$ cluster at 1668 K after the reaction with the 12th H-atom, showing that the phase transition from an intermediate to a completely liquid-like state takes about 15 ps after the $Si_{29}H_{24}$ cluster reacted with the 12th H-atom.

All 24 H-atoms are on the surface of the saturated $Si_{29}H_{24}$ cluster before the heating with H-atoms. As a result, this cluster is initially less reactive than the $Si_{15}H_{10}$ cluster and some of the impinging H-atoms do thus not react with this cluster at all and are reflected. Despite this difference between the two investigated clusters, however, the melting always occurs once the reactions with incoming H-atoms supplied enough energy for the solid-liquid phase transition to take place since the particular cluster structure was lost a long time before the melting.

Our quantitative analysis of H-induced processes concerning plasma-born hydrogenated silicon clusters might help to improve our understanding of dusty plasma dynamics necessary for the optimization of plasma conditions employed for *pm-Si:H* thin film deposition.

Chapter 4

Hydrogen-induced healing of cluster-damaged silicon surfaces

Abstract A silicon surface which was partly damaged by the violent impact of hydrogenated silicon clusters has been treated by hydrogen atoms. After the exposure with hydrogen atoms, we observe that the ill-defined silicon surface is rearranged to its initial crystalline structure and that the silicon atoms of the deposited cluster are now incorporated in the crystalline structure of the repaired substrate surface.

4.1 Introduction

Recently, hydrogenated silicon nanoparticles synthesized in a plasma enhanced chemical vapor deposition (PECVD) reactor have been shown to be ideal precursors for the deposition of high quality silicon thin films, such as polymorphous [86], microcrystalline [103], and epitaxial silicon thin films [20] with relatively high deposition rates. Deposition mechanisms of hydrogenated silicon clusters on crystalline silicon substrates under realistic plasma conditions have been investigated by Ning *et al.* by means of molecular dynamics (MD) simulations with a special emphasis on the experimental parameters governing the various deposition processes from soft-landing to destructive deposition [35, 36]. The images shown in Fig. 4.1 illustrate those deposition mechanisms [42]. Among other impact parameters, cluster impact energy has the most significant influence on the deposition mechanisms. Low impact energies lead to the soft-landing of the clusters on the substrate. In the intermediate impact energy range, the clusters partially dissociate. Complete cluster dissociation followed by fragment migration onto the surface and cluster atom penetration into the lattice is found for high impact energies.

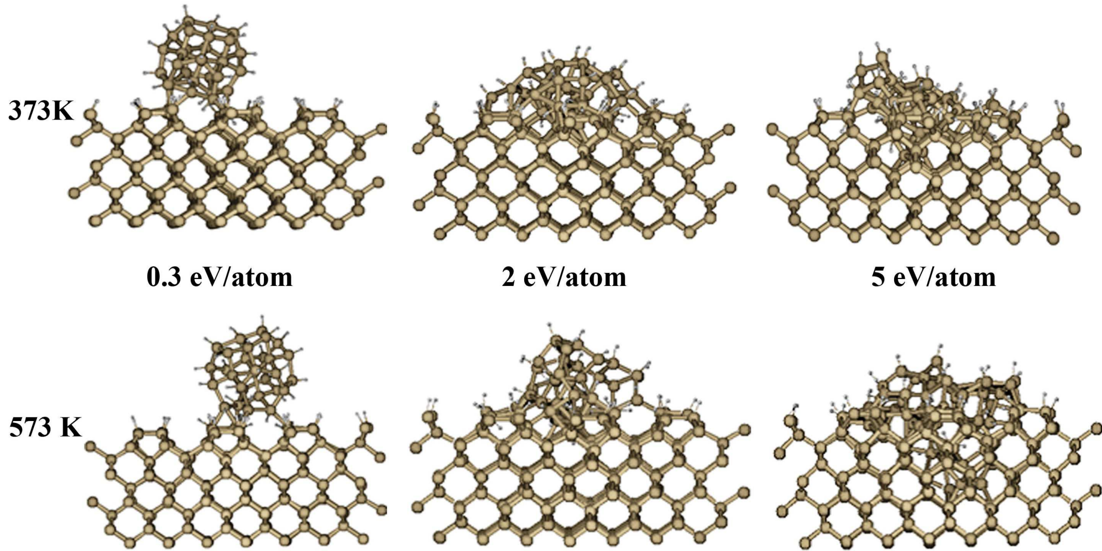

FIGURE 4.1: Snapshots at t = 10 ps of various trajectories of the deposition of the $Si_{29}H_{24}$ clusters with different impact energies on the substrates at different temperatures to illustrate various deposition mechanisms, from soft-landing to destructive deposition of clusters.

During the growth of thin silicon films by PECVD, there is always a continuous flux of atomic hydrogen to the surface. This is the result of the dissociation of silane and hydrogen molecules in the plasma reactor. Atomic hydrogen plays a crucial role in PECVD. For instance, it is known to heat up plasma-born hydrogenated silicon clusters [104], to trigger the auto-assembly of silicon nanocrystals [22, 24, 28, 105], and to cause silicon surface etching [106, 107]. Fontcuberta *et al.* have studied the role of atomic hydrogen on the growth of thin silicon films based on *in-situ* spectroscopic ellipsometry measurements. In their experimental investigation, hydrogenated amorphous silicon (*a-Si:H*) and hydrogenated polymorphous silicon (*pm-Si:H*) films were exposed to hydrogen plasmas. For both materials, they observed the formation of a hydrogen-rich subsurface layer during the first minute of the hydrogen exposure. Thereafter, the hydrogen-rich subsurface layer thickness remained relatively constant while the total film thickness decreased. The hydrogen diffusion coefficient and etching rate were found to be higher in *a-Si:H* films than in *pm-Si:H* ones. Since a possible transition to the microcrystalline phase is in general induced by H-atoms, the authors conclude that microcrystalline materials can be obtained from amorphous silicon films, but not from polymorphous ones even for relatively similar large atomic hydrogen flow conditions in the plasma reactor [106, 107]. The work of Sriraman *et al.* [67] demonstrated hydrogen-induced relaxation of partially strained silicon thin films by both MD simulations and infrared spectroscopy. The authors [67, 108, 109] have illustrated one possible mechanism: hydrogen atoms diffusing through the amorphous silicon films can insert temporarily into strained Si-Si bonds leading to the formation of intermediate bridging and bond-centered Si-H-Si

configurations. When the H-atoms move away, the strained Si-Si bonds relax resulting in crystalline configurations because the silicon atoms are now able to move into lower energy states.

In the present work, we will employ atomic hydrogen to treat the silicon surface which was locally damaged by the violent impact of a hydrogenated silicon cluster to see if there is a transition to an ordered structure as the one of the initial silicon surface before the cluster-induced damage.

4.2 Simulation details

We have employed the general chemical dynamics computer program VENUS [43] with the empirical interatomic Ohira-Tersoff potential [59, 60, 68] to simulate the deposition of plasma-born hydrogenated silicon clusters on crystalline silicon substrates and the H-treatment of cluster-damaged silicon surfaces. The time step used in our MD simulations was chosen to be 0.1 fs to follow trajectories of up to 400 ps.

4.2.1 Deposition of plasma-born hydrogenated silicon clusters on H-terminated Si(100)-(2×1) surfaces

We have chosen plasma-born $Si_{15}H_{10}$ clusters to deposit on H-terminated Si(100)-(2×1) surfaces. First, the cluster was optimized to its minimum energy structure and heated up to 300 K to reproduce our experimental plasma conditions. Figure 4.2 shows the atomic configuration of the $Si_{15}H_{10}$ cluster.

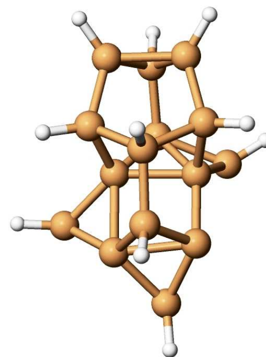

FIGURE 4.2: The initial configuration of the plasma-born $Si_{15}H_{10}$ cluster. The large brown spheres represent silicon atoms while the small white ones represent hydrogen atoms.

The H-terminated Si(100)-(2×1) substrate has the dimensions of 21.72 Å × 21.72 Å × 10.86 Å and consists of 288 silicon atoms terminated by 32 hydrogen atoms (see

Fig. 4.3). Periodic boundary conditions are applied in the two directions parallel to the surface plane. The top silicon layer is a (2×1) reconstructed layer including silicon dimers. The bottom two silicon layers are kept rigid in their equilibrium positions to avoid the translation and bending of the entire substrate in space. To control the substrate temperature, we apply a Berendsen thermostat [110] to the three silicon layers above the two rigid layers. The H-terminated Si(100)-(2×1) substrate was heated to 573 K corresponding to the low temperature requirement in silicon thin film production in industry.

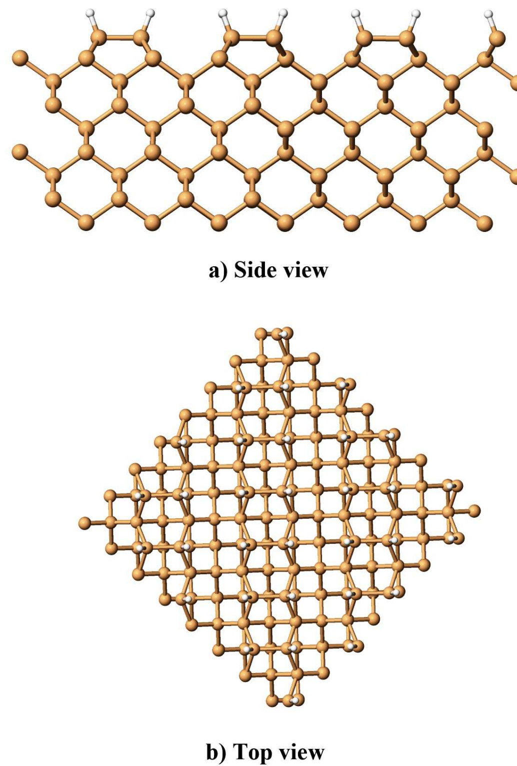

FIGURE 4.3: Side and top view of the initial configuration of the H-terminated Si(100)-(2×1) surface. The atom colors are the same as in Fig. 4.2.

The $Si_{15}H_{10}$ clusters were initially placed at positions sufficiently far from the substrate so that their interaction with the surface can be neglected. The clusters were then deposited onto the surfaces with impact energies ranging from 0.42 to 6.21 eV/atom. We have observed both soft-landing and destructive deposition of the $Si_{15}H_{10}$ clusters on the substrates over this impact energy range. To investigate the hydrogen treatment of silicon surfaces after they became damaged by the cluster impact, we start from a trajectory in which the cluster with an impact energy of 3.70 eV/atom approached the silicon substrate at 573 K leading to a “rough” surface with a locally disordered structure (see Fig. 4.4d).

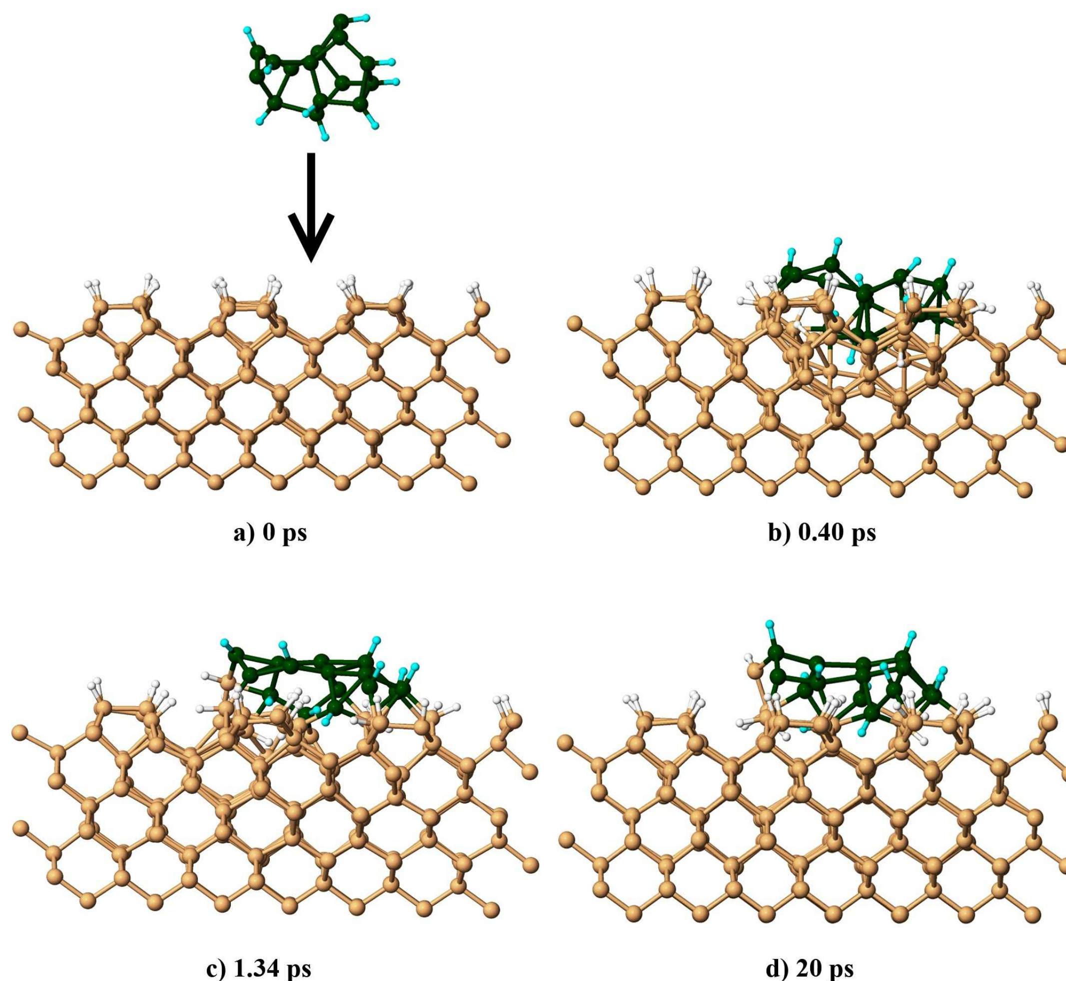

FIGURE 4.4: Snapshots of the atomic configurations at various times during the deposition of the $Si_{15}H_{10}$ cluster onto the substrate at 573 K with an impact energy of 3.70 eV/atom. The large brown spheres represent surface silicon atoms while the green ones represent silicon atoms of the $Si_{15}H_{10}$ cluster. The small white spheres represent surface hydrogen atoms while the cyan ones represent hydrogen atoms of the $Si_{15}H_{10}$ cluster.

4.2.2 Hydrogen treatment processes

The resulting partially damaged silicon surface obtained in the trajectory shown in Fig. 4.4 was then "treated" by atomic hydrogen. To this end, the incoming H-atoms were put at a distance of about 8 Å from the surface to assure there is no initial interaction with the surface atoms. The H-atoms were then sent to the surface, one after the other, with a normal incidence angle and a kinetic energy sampled from a room temperature Maxwell-Boltzmann distribution as in our plasma reactors. The time interval between two reactions with H-atoms was 5 ps [67].

The heating from reactions with hydrogen atoms is needed for the damaged surface area to overcome energy barriers to more stable structures. Due to the relatively small

size of our substrate model, the Berendsen thermostat interacts unrealistically with the surface atoms: under certain conditions the thermostat "reflects" the heat flow coming from the impact area instead of spreading it out to the "bulk" of the substrate (see Fig. 4.5a and b). Therefore, we followed the simulation procedure detailed in Ref. [111] and switched off the thermostat during the initial interaction of the hydrogen atoms with the "rough" silicon surface. Thereafter, we switched the thermostat on again to cool the substrate down to the experimental temperature of 573 K.

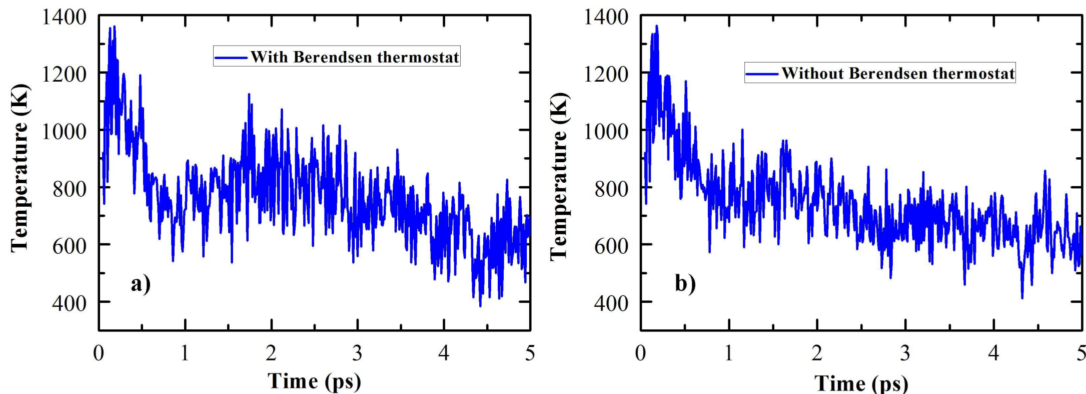

FIGURE 4.5: The evolution of the instantaneous temperature of the cluster atoms together with the substrate atoms touching the cluster after one reation with a H-atom: a) with Berendsen thermostat; b) without Berendsen thermostat.

4.3 Results

Figure 4.6 presents the evolution of the instantaneous temperature of the cluster atoms together with the substrate atoms touching the cluster as function of the number of reactions with H-atoms. In this typical trajectory, the temperature of the cluster atoms together with the substrate atoms touching the cluster heats above 1800 K after the reactions with 12 H-atoms. This temperature then rapidly equilibrates to 1616 K within 1.5 ps. We limited ourselves to 12 impinging H-atoms because the temperature of the surface had already reached a temperature which is around the melting point of bulk silicon.

After the reactions with the first five H-atoms, the temperature of the cluster atoms together with the substrate atoms touching the cluster reaches 1050 K and the cluster atoms start the rearrangement process. After the surface exposure to nine H-atoms, the temperature is 1371 K and a region of six silicon atoms on the silicon surface rearranges itself to a structure which has the same order as the initial substrate (see Fig. 4.7b).

Continuing the hydrogen exposure process, we observe the reorganization of the locally disordered silicon surface; once a silicon atom finds a position where its presence

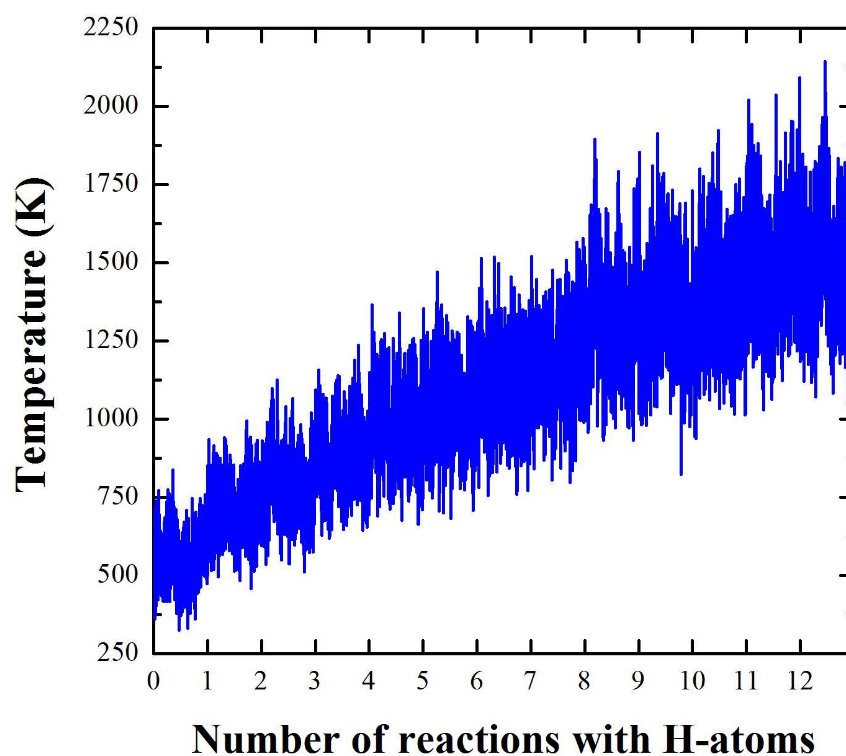

FIGURE 4.6: The evolution of the instantaneous temperature of the cluster atoms together with the substrate atoms touching the cluster as function of the number of reactions with H-atoms.

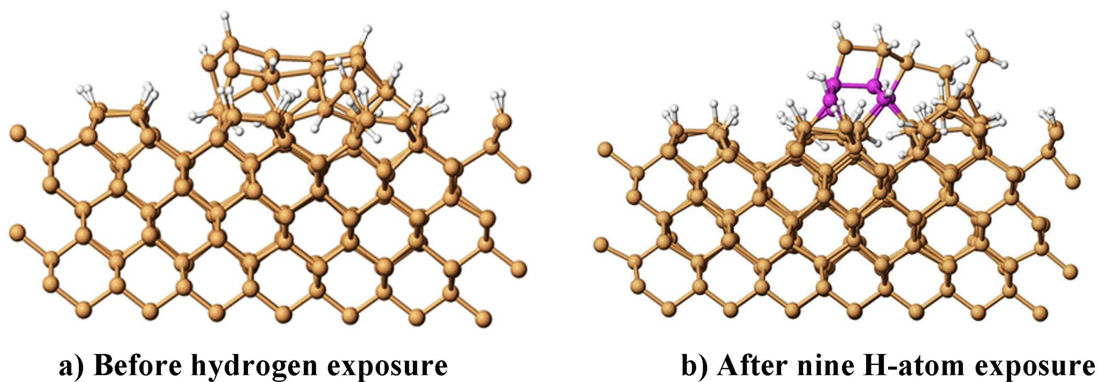

FIGURE 4.7: Snapshots of the atomic configuration: a) before surface exposure to atomic hydrogen. The snapshot was recorded 20 ps after the impact of a $Si_{15}H_{10}$ cluster onto a substrate at 573 K with an impact energy of 3.70 eV/atom; b) after surface exposure to nine H-atoms. The violet atoms indicate the region where six silicon atoms of the "rough" surface rearranged themselves to a structure which has the same order as the initial substrate.

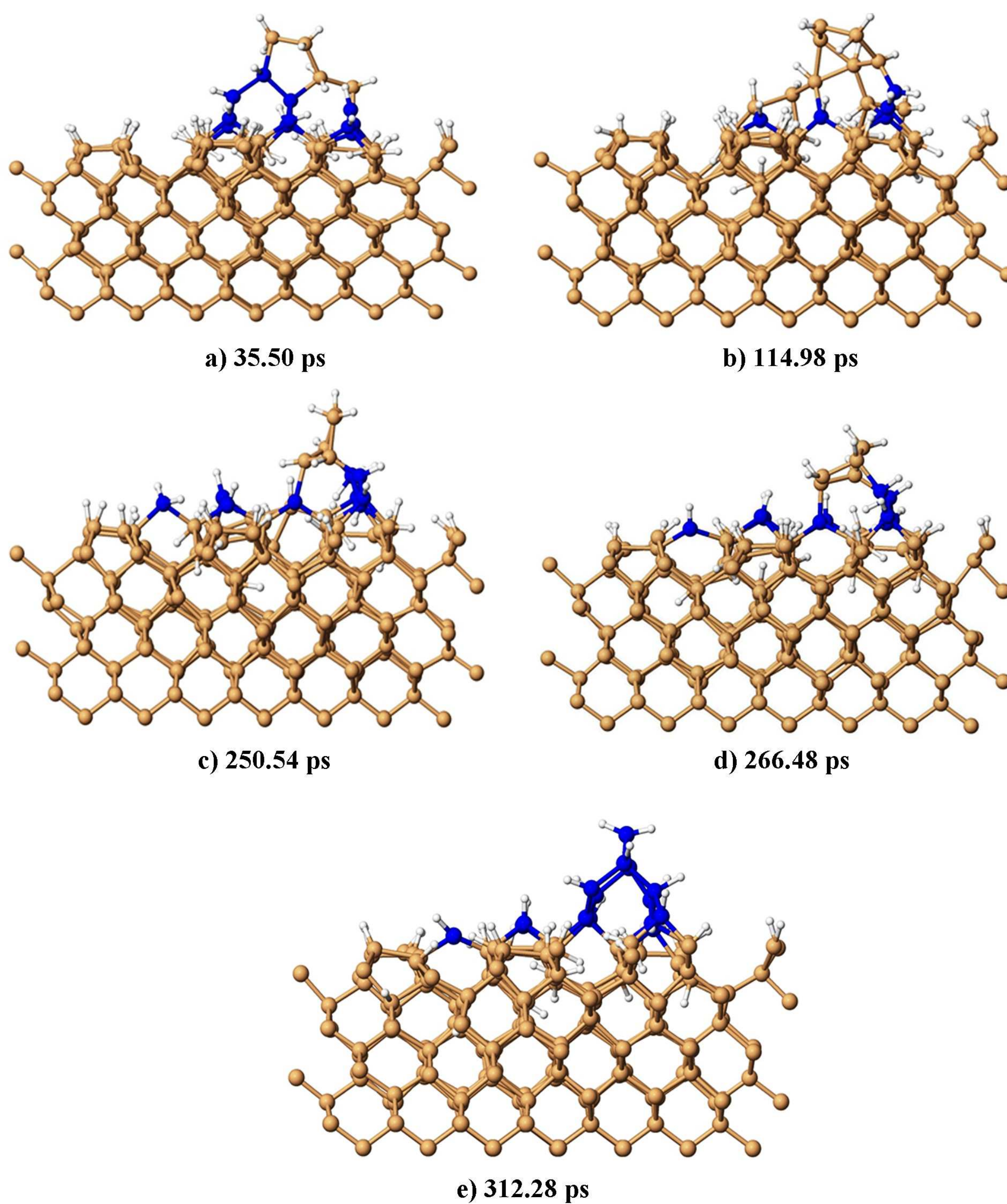

FIGURE 4.8: The structure evolution of the silicon surface after the 12 H-atom exposure, at a surface temperature around 1616 K. The blue atoms represent the silicon atoms found in epitaxial positions.

increases the volume of the crystalline part of the Si(100) surface, we consider it to be in an epitaxial position. A typical example of the silicon surface after the 12 H-atom exposure, shown in Fig. 4.8 , indicates that there are 11 out of 15 silicon atoms that found epitaxial positions at about 35 ps after the reaction with the 12th H-atom took place. 10 ps later, however, this structure is lost again. At about 115 ps, there are only 5 out of 15 silicon atoms that remain in epitaxial positions. Thereafter, we have observed a structure reorganization again leading to 10 out of 15 silicon atoms in epitaxial positions at about 250 ps and 11 out of 15 silicon atoms in epitaxial positions at about 266 ps. Finally, at about 312 ps, all 15 silicon atoms of the initial cluster are settled in epitaxial positions.

The reaction with H-atoms leads to the heating of the silicon surface and, consequently, to the increase in kinetic energy of the silicon atoms on the surface. This increase in kinetic energy allows the silicon atoms to overcome local potential energy barriers to access epitaxial positions. However, once a silicon atom reaches its epitaxial positions, it still has enough energy to overcome the local potential barriers to go to a less stable position again; especially, when considering that the access to an epitaxial position considerably lowers its potential energy resulting in a yet higher kinetic energy. In order to remain in its epitaxial position, the silicon atom has to lose a significant part of its kinetic energy rapidly to its neighbor atoms. The heat transfer to the other, colder silicon atoms turns out to be actually fast enough to maintain all 15 cluster silicon atoms in their epitaxial position in a metastable manner. To fix them "permanently" in their epitaxial positions, we then turn on the Berendsen thermostat to "cool" down the entire silicon surface to the experimental substrate temperature of 573 K. Figure 4.9 shows that all 15 cluster silicon atoms found perfect epitaxial positions after the cooling down.

To investigate the structure of the silicon surface after the exposure to 12 H-atoms and the cooling down more quantitatively, we calculated the radial distribution function (RDF) of the cluster atoms and the substrate atoms touching the cluster and compared it with the RDF of those atoms before the H-treatment and with the RDF of bulk crystalline silicon (*c-Si*) at 573 K. In our calculation, the latter was simulated as a crystalline structure of 192 silicon atoms with three dimensional periodic boundary conditions at 573 K. As can be seen in Fig. 4.10, this *c-Si* structure is characterized by peaks shown as the black curve that correspond to short- and long-range order. For our local surface region of 26 silicon atoms, we focus on the first three peaks of the RDF. Before the hydrogen exposure, the disordered nature of the cluster atoms and the substrate atoms touching the cluster can be witnessed from the corresponding RDF (blue curve in Fig. 4.10). The first peak exhibits a Si-Si interatomic distance considerably longer than the Si-Si bond length in bulk *c-Si*. The second peak is excessively broad; and the third peak is significantly shifted to longer distances in comparison to the RDF of bulk *c-Si*. After

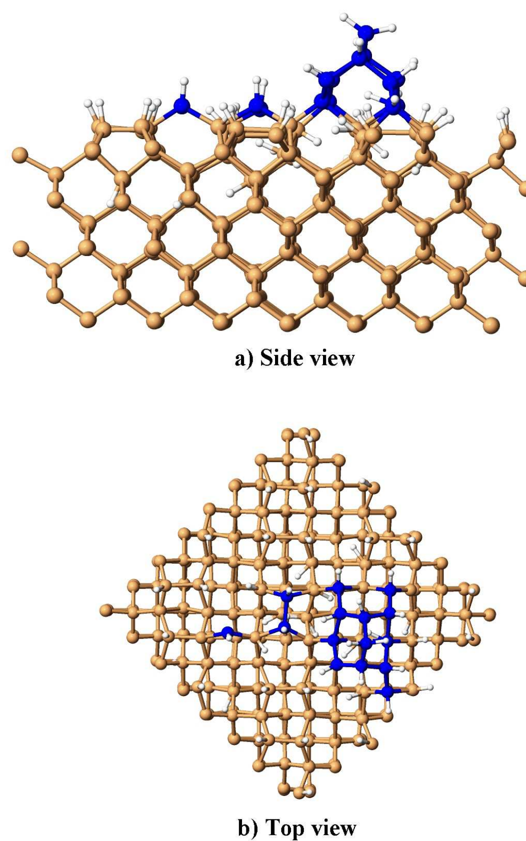

FIGURE 4.9: Side and top view of the atomic configuration after the cooling down to 573 K.

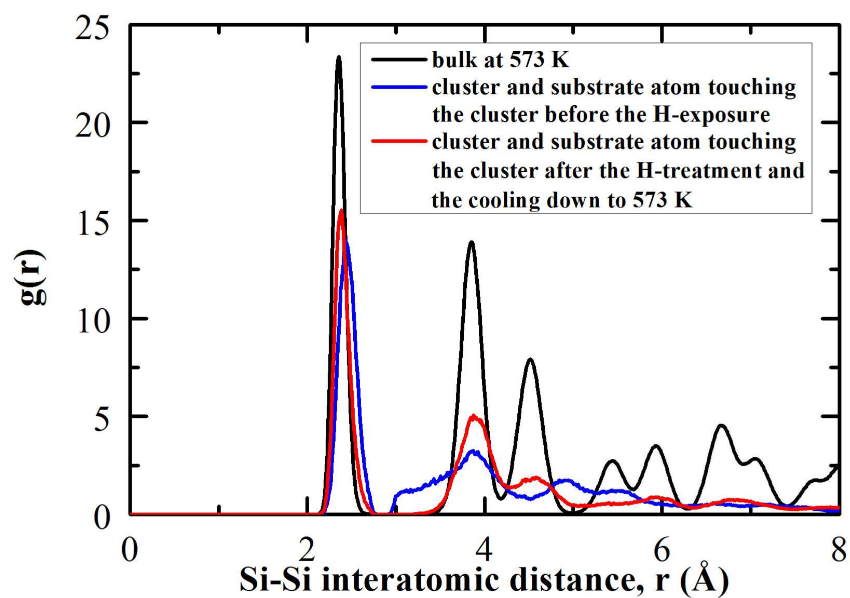

FIGURE 4.10: The RDF of the cluster atoms and the substrate atoms touching the cluster after the H-treatment and the cooling down to 573 K is compared with the RDF of those atoms before the H-exposure and with the RDF of bulk *c-Si* at 573 K.

the H-treatment and the cooling down, we observe that the first peak of the RDF graph of the the cluster atoms and the substrate atoms touching the cluster (red curve in Fig. 4.10) is shifted close to the one of bulk *c-Si*. Moreover, the second and the third order peaks are consistent with that of bulk *c-Si*; this observation is not only true for their absolute positions, but even for their relative intensities. This means that H-atoms can, indeed, "heal" a damaged silicon surface with a locally disordered configuration to an ordered structure. This finding, however, is only correct when a relatively low flux of H-atoms is used; at too high incoming H-atom rates, the surface will instead suffer even greater damage due to the resulting etching.

4.4 Conclusions

The increase in kinetic energy of the silicon atoms is the result of the chemical reaction with H-atoms (either adsorption or recombination). This increase in kinetic energy permits the silicon atoms to overcome local potential barriers giving them access to the epitaxial positions.

Every time a silicon atom finds an epitaxial position, the total potential energy becomes somewhat more negative and the local region around that silicon atom heats accordingly slightly up. As long as this additional kinetic energy remains localized around that silicon atom, it can leave again its epitaxial position. The silicon atom can only remain "permanently" in its epitaxial position if a sufficient part of its increased kinetic energy is transferred to its neighbors. Ideally, it has to be well distributed among many neighbor atoms to avoid that another silicon atom might leave its epitaxial position.

Exposure of a partially damaged silicon surface to relatively few H-atoms leads to heating and ordering, while too much H-atoms result in extreme heating and etching. We propose for the experimentalists to expose locally disordered silicon surfaces to a hydrogen plasma after epitaxial deposition to repair local damages due to non-perfect epitaxial deposition conditions.

Chapter 5

Cluster-catalyzed epitaxial growth of thin silicon films

Abstract Thin crystalline silicon solar cells based on epitaxial silicon thin films have been widely investigated in the field of photovoltaics. Recently, it has been shown experimentally that high-quality epitaxial growth of silicon thin films in a PECVD reactor can be achieved at low temperatures and high deposition rates when plasma-born hydrogenated silicon clusters are used as deposition precursors. However, the under-lying growth mechanisms for such an epitaxial growth have not been understood yet. In the present work, we have performed MD simulations for the deposition of hydrogenated silicon clusters on crystalline silicon substrates by controlling various impact parameters to get a better understanding of high-speed epitaxial growth of silicon thin films catalyzed by plasma-born hydrogenated silicon nanoparticles at low substrate temperatures. Our results show that a temporary phase transition of the silicon atoms in the impact area to the liquid state seems to be necessary for the cluster-catalyzed epitaxial growth. In addition, we present evidence that a non-normal incidence angle for the cluster impact significantly facilitates the epitaxial growth of thin crystalline silicon films.

5.1 Introduction

Epitaxial silicon thin films can be grown on crystalline silicon substrates with a huge variety of different deposition procedures [112]. PECVD presents many advantages over other techniques. The most important one is the fact that it is possible to obtain epitaxial silicon thin films at considerably lower substrate temperatures (as low as 150 °C [18]) than other CVD techniques, such as Atmospheric Pressure CVD [113] or HWCVD

[15]. When operated close to dusty plasma conditions, PECVD yields, in addition, significantly higher film growth rates in comparison to other low temperature techniques as Molecular Beam Epitaxy (MBE) due to the presence of plasma-born hydrogenated silicon nanoparticles. Those clusters do not only "catalyze" the film growth, but they also lead to films with high quality. The resulting epitaxial silicon films have been employed as the absorber layers in heterojunction solar cells showing a fill factor as high as 78.6% and an efficiency of 7% for a 2.4 μm absorber thickness [41]. At high hydrogen flow rates, epitaxial silicon films grown from $SiF_4/H_2/Ar$ gas mixtures at a substrate temperature of $\sim 200\,°C$ in a radio-frequency (RF) PECVD reactor form a porous interface layer with the crystalline silicon wafer that can be used to transfer the epitaxial films to low cost foreign substrates [19]. The doped epitaxial silicon thin films can also be achieved in a RF PECVD reactor at substrate temperatures of 175 °C and 140 °C for phosphorous-doped and boron-doped silicon films, respectively [114]. A p-type epitaxial layer and a n-type *c-Si* wafer have been assembled to fabricate a p-n junction solar cell which exhibits an efficiency of 14.2% and a fill factor of 76.4%. Epitaxial silicon thin films produced by PECVD should, thus, be considered for the future design of high-efficient solar cells. However, the optimal experimental conditions and the under-lying growth mechanisms leading to high-speed epitaxial growth of thin silicon films from hydrogenated silicon nanoparticles remain far from being understood.

In the literature, numerous MD simulations for the deposition of a single silicon cluster or a continuous beam of silicon clusters on crystalline silicon substrates were reported. Those simulations have been performed to study the influence of impact parameters on the growth mechanisms of silicon thin films, *e.g.*, amorphous and epitaxial silicon thin films deposited by ionized cluster beam technique [29–40]. Biswas *et al.* simulated the single cluster impacts on a Si(111) surface [29]. Tentatively, they assumed that the impinging cluster should dissociate and spread in a uniform layer on the substrate to achieve epitaxial films grown from cluster deposition.

Kwon *et al.* examined the deposition of an amorphous 33-silicon atom cluster on a Si(111) substrate and identified regimes of both low and high surface diffusivity of the silicon atoms [30]. Low surface diffusion resulted in amorphous silicon films, while epitaxial silicon films were produced with deposition conditions of high surface diffusion; *i.e.*, the authors suggest that cluster spreading is necessary for epitaxial growth. In fact, the authors have observed complete epitaxial growth in the case where clusters with an energy of 2.1 eV deposited on the substrate at about 1392 K; and nearly complete epitaxial growth in the case of cluster translational energies of 1.05 eV at the same high substrate temperature. Unluckily, the authors did not investigate the possibility of epitaxial growth for lower surface temperatures.

Gilmer *et al.* [31] have shown that crystalline patterns may be obtained by depositing very small clusters (Si_{10}) with energies of 17 and 70 eV/atom onto non-specified

silicon substrates at temperature of 380 K. They also observed a thin amorphous layer on top of the films during the cluster deposition. They qualitatively argued that impinging clusters cause some local heating at the point of the impact facilitating the atomic rearrangement and leading to crystallization at the amorphous-crystal interface.

Xie *et al.* have studied silicon films grown from the deposition of glassy Si_{10} clusters on Si(111) substrates at 1000 [32] and 300 K [33]. Their work showed the influence of cluster impact energy and substrate temperature on the spreading of the cluster on the substrate as well as the structure of the resulting films. At a substrate temperature of 1000 K, they found higher surface diffusion and spreading of deposited clusters with the increase of impact energy. However, very high impact energy led to damage of both the substrate and the growing film. They showed that epitaxial silicon films can be achieved with a moderate impact energy (10 eV/atom) of impinging clusters. They concluded that silicon films grown at a low substrate temperature of 300 K only exhibit amorphous structures with all investigated impact energies.

Tarus *et al.* [34] deposited fullerene Si_{20} clusters on a Si(001)-(2×1) reconstructed surface with various cluster energies at two different substrate temperatures (300 and 1000 K). At 300 K, they did not observe any epitaxial growth. The silicon films deposited at 1000 K, however, showed epitaxial growth for all studied cluster energies. They also found an amorphous film on top of the substrate and an advancing crystalline-amorphous interface below it. They attributed local heating caused by the cluster impact to the enhancement of epitaxial growth. This means that the lower substrate temperature is, the higher the impact energy needed for epitaxial growth. They concluded that epitaxial growth originates from the rearrangement of atoms at the amorphous-crystalline interface and not from the atomic diffusion on the surface; *i.e.*, contrary to Kwon *et al.*, Tarus *et al.* exclude the importance of cluster spreading for epitaxial growth.

Deposition mechanisms of hydrogenated silicon clusters on H-terminated Si(100)-(2×1) substrates under realistic plasma conditions have been investigated by Ning *et al.* with a special emphasis on the experimental parameters governing the various deposition processes [35, 36]. The authors studied small and moderate clusters (less than 30 silicon atoms). The results reveal that in the employed cluster size range the cluster-surface interaction mechanisms are only slightly influenced by the size of the cluster, while they strongly depend on the impact energy. Low impact energies lead to the soft-landing of clusters on the substrate. At the intermediate impact energy range, the clusters partially dissociate. Complete cluster dissociation followed by fragment migration onto the surface and cluster atom penetration into the lattice is found for high impact energies. Ning *et al.* observed the onset of epitaxial-like structure growth in only one case where the cluster with an impact energy of 4.8 eV/atom almost completely lost its initial structure due to the surface impact. They suggested that epitaxial growth may in principle occur at impact energies that are high enough to dissociate the impinging cluster, but

low enough to avoid serious damage of the substrate structure. They also promoted the use of amorphous clusters for the deposition of epitaxial silicon thin films.

Chen *et al.* [37] simulated the formation of Si nanoclusters in the plasma during continuous cooling from high temperature Si vapors. The resulting clusters have a globular shape and are loosely bound structure. Those clusters (Si_{256} and Si_{1000}) were then deposited on Si(100) substrates with different impact velocities and at different substrate temperatures. The authors observed an epitaxial rearrangement of silicon atoms of the clusters at a certain distance ($\sim$ 2-3 nm) from the impact interface. They suggested that clusters as small as $\sim$ 3 nm could play the role of growth precursors for fast rate epitaxial growth of silicon films under mesoplasma conditions. They also concluded that there is no need for spreading. Unluckily, their conclusions have to be considered with caution since they only employed a one-dimensional Lennard-Jones potential for the calculation of the interatomic forces leading, for instance, to the reported long range rearrangement schemes.

Later, the same authors [38] extended their work to hydrogenated silicon clusters which are obtained during rapid cooling of high temperature atomic Si and H vapor mixtures. They found that hydrogenated silicon clusters exhibit higher degrees of deformation and atomic self-ordering than pure silicon clusters. They also observed that the H-atoms move from the inside to the surface of the cluster, and desorb from the cluster surface as species, such as SiH_3 and SiH_4. They speculated that the resulting absence of H-atoms within the cluster leaves enough space for silicon atoms, consequently facilitating the cluster deformation and the silicon atom rearrangement. They concluded that H-atoms incorporated in hydrogenated silicon clusters promote the epitaxial growth from cluster deposition. Again, those results call for caution since those authors are the only ones who observed H-atoms inside of the hydrogenated silicon clusters.

In the above mentioned studies, many aspects of cluster-surface impact possibly leading to epitaxial growth of thin silicon films under different experimental conditions have been examined with MD simulations. However, those studies have only observed and suggested some conditions for epitaxial growth of thin silicon films by means of cluster deposition. The under-lying growth mechanisms for such epitaxial silicon thin films, however, have not been understood yet. Therefore, our work is aimed toward a better understanding for the high-speed epitaxial growth of silicon thin films at low substrate temperatures from plasma-born hydrogenated silicon nanoparticles as experimentally observed in PECVD reactors.

5.2 Simulation details

Generally, parameters governing the cluster-surface deposition process are cluster impact velocity/energy, cluster shape, structure (crystalline/amorphous) and size, incidence angle of approaching cluster, substrate temperature, and the nature and crystal orientation of the exposed surface. Among those parameters, impact energy is the most important parameter and the substrate temperature plays a second role. Hence, impact energy and substrate temperature are chosen to be the controlling parameters in our investigations. Contrary to Ning's studies as mentioned above, our work is based on an alternative strategy: *Epitaxial growth may occur at impact energies that are high enough to dissociate or to deform the initial atomic structures sufficiently to allow the rearrangement in a different configuration for all silicon atoms of both the impinging cluster and the local substrate; i.e., during an intermediate transition period the silicon atoms of the cluster and of the local surface become indistinguishable.*

- Cluster preparation: In our simulations, we have employed plasma-grown amorphous clusters (Si_8H_{12}, $Si_{15}H_{10}$, and $Si_{28}H_{13}$) and the well-known $Si_{29}H_{24}$ nanocrystal [90–94] as impinging clusters. Those clusters were optimized to obtain their minimum energy structures and heated up to 300 K according to our experimental plasma conditions. Figure 5.1 presents their corresponding minimum energy configurations.

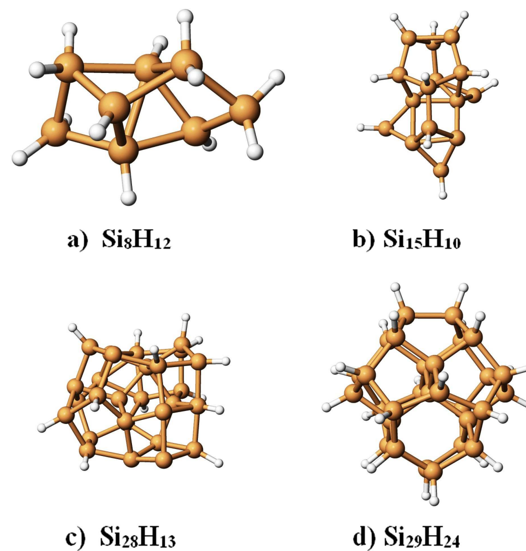

FIGURE 5.1: The initial configurations of the employed hydrogenated silicon clusters. The large brown spheres represent silicon atoms while the small white ones represent hydrogen atoms.

- Surface preparation: Recent experimental studies have been shown that epitaxial growth of crystalline silicon thin films based on plasma-generated hydrogenated silicon nanoparticles in a PECVD reactor can be obtained on (100), but not on (111) *c-Si* wafers

[16]. Therefore, the H-terminated Si(100)-(2×1) surface is chosen as a substrate in our work. Details of substrate characterization were described in chapter 4. We heated up the substrate to 373, 473, and 573 K since those substrate temperatures are usually used in a PECVD reactor.

The room temperature cluster is initially placed at a position where the cluster-surface interaction is negligible. After the addition of a center-of-mass velocity to all cluster atoms, the cluster approaches the surface with a normal incidence angle. All simulations are carried out with the general chemical dynamics computer program VENUS [43] using the empirical interatomic Ohira-Tersoff potential [59, 60, 68]. The time step used in our MD simulations was chosen to be 0.1 fs.

5.3 Results

5.3.1 Deposition of $Si_{15}H_{10}$ clusters on a H-terminated Si(100)-(2×1) surface

We started our simulations with the amorphous $Si_{15}H_{10}$ cluster. This cluster was deposited on the substrate at 373 K with different impact energies ranging from 0.42 to 9.38 eV/atom. We have observed various deposition mechanisms over that range of cluster impact energies. At impact energies from 0.42 to 1.84 eV/atom, the $Si_{15}H_{10}$ cluster lands on the surface forming new Si-Si bonds between the cluster and the substrate. No cluster atoms penetrate into the substrate during these deposition processes. Clusters deposited with impact energies from 2.39 to 5.30 eV/atom, however, partly or completely penetrate into the substrate. About 0.4 ps after the collision, the cluster silicon atoms start to reconstruct. Some of them might insert themselves into lattice positions of the substrate by replacing substrate silicon atoms. The other cluster silicon atoms together with some substrate silicon atoms move to the surface and settle there by forming bonds with surface silicon atoms. Eventually, there is no substrate damage. High impact energies from 6.21 to 9.38 eV/atom cause serious and irreversible damage to the crystalline substrate structure.

We have observed epitaxial growth in the case where $Si_{15}H_{10}$ clusters approach the substrate with an impact energy of 5.30 eV/atom. Figure 5.2 shows the snapshots of the atomic configurations at various times during the collision process. At 0.4 ps the cluster completely penetrates into the substrate. Thereafter, the cluster silicon atoms start to reconstruct and eventually at about 78.70 ps all cluster silicon atoms adopt a perfect, epitaxial order on top of the initial substrate structure.

Directly after the impact, the temperature of the cluster atoms together with the substrate atoms touching the cluster exceeded 3000 K due to the transfer of the kinetic

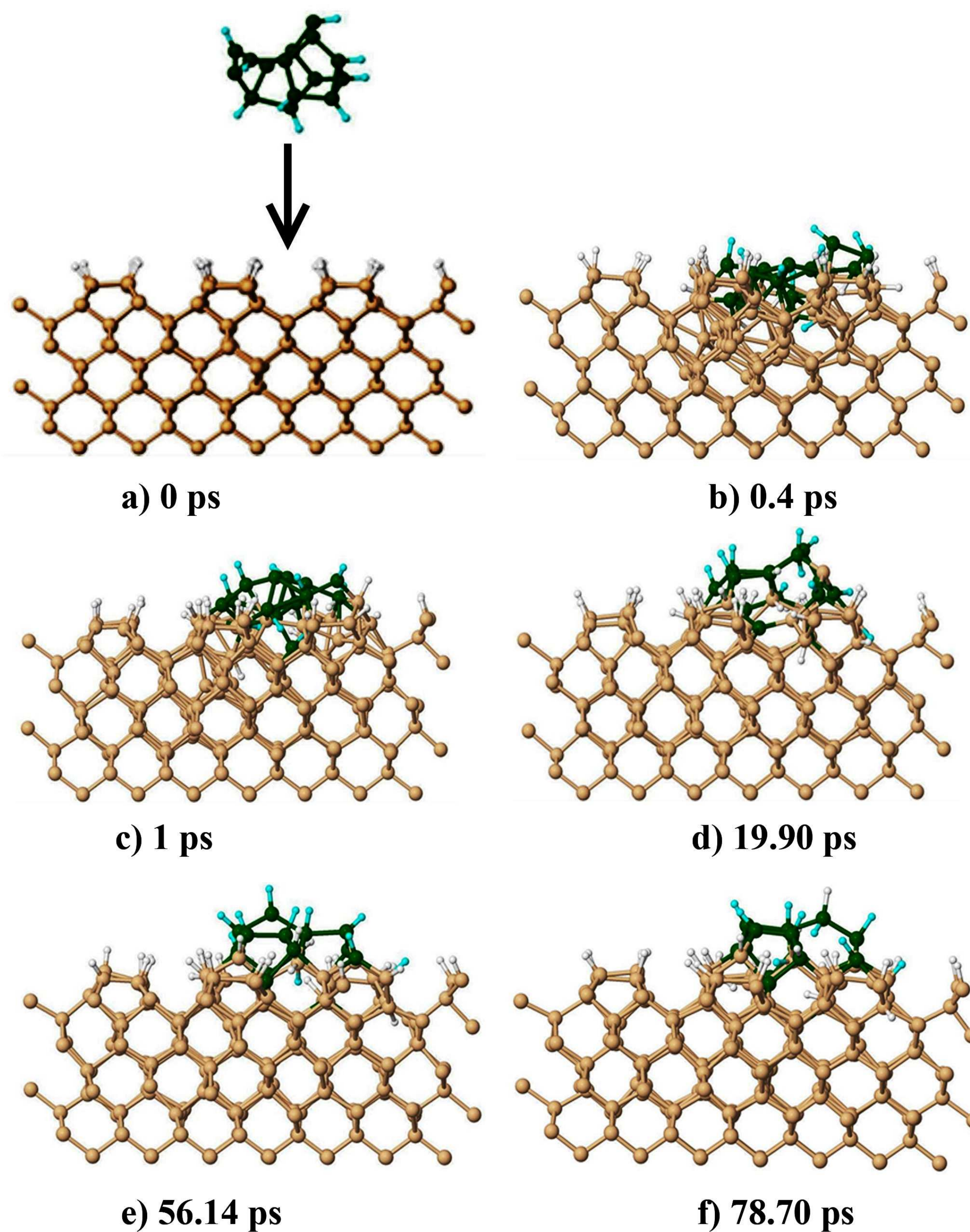

FIGURE 5.2: Snapshots of atomic configurations at various times during the $Si_{15}H_{10}$ cluster surface collision with an impact energy of 5.3 eV/atom and a substrate temperature of 373 K. The large brown spheres represent the surface silicon atoms while the green ones represent silicon atoms of the $Si_{15}H_{10}$ cluster. The small white spheres represent surface hydrogen atoms while the cyan ones represent hydrogen atoms of the $Si_{15}H_{10}$ cluster. The same colors will be used to display atomic configurations of the following investigated trajectories.

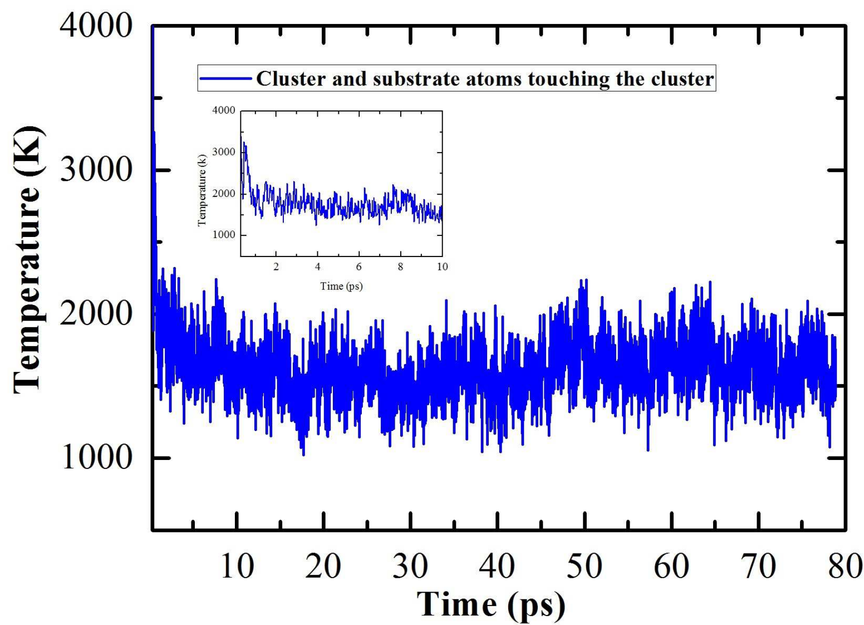

FIGURE 5.3: Time evolution of the instantaneous temperature of atoms belonging to both the initial $Si_{15}H_{10}$ cluster and the substrate in the immediate vicinity of the cluster after impact. The insert shows that right after the impact the temperature of cluster atoms and substrate atoms touching the cluster exceeds 3000 K and then rapidly decreases to 1600 K.

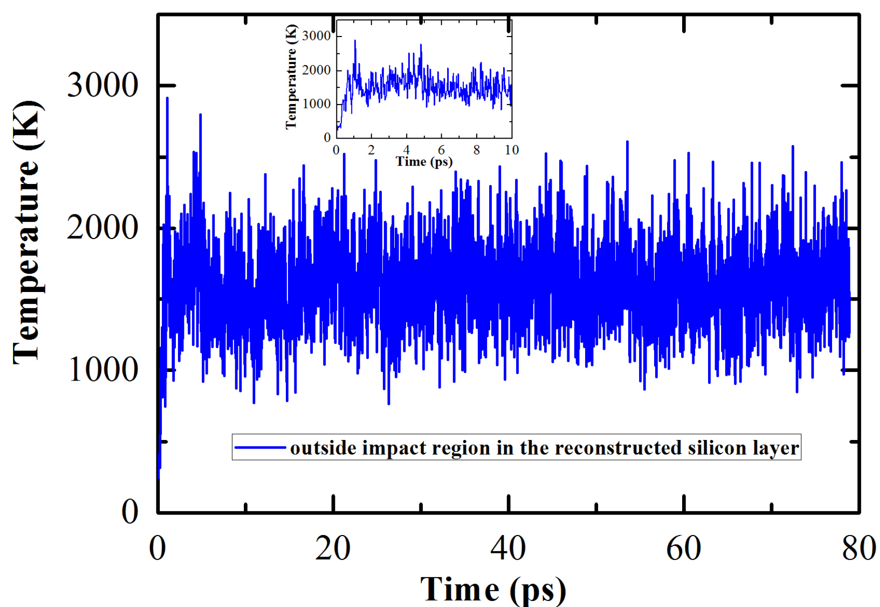

FIGURE 5.4: Time evolution of the instantaneous temperature of substrate atoms surrounding the impact region in the reconstructed silicon layer after the $Si_{15}H_{10}$ cluster-surface impact. The insert indicates a rapid increase of the temperature of those atoms from 373 K to about 3000 K and a subsequent decrease to an equilibrated temperature of 1600 K.

impact energy. Rapidly after, both the temperature of those atoms, as well as the temperature of the substrate atoms surrounding the impact region equilibrated at about 1600 K (see Fig. 5.3 & 5.4).

To comply with the experimental conditions, we thereafter cooled down the temperature of all atoms to 373 K by employing a Berendsen thermostat [110] to the substrate. Figure 5.5 presents the atomic configurations after the cooling down.

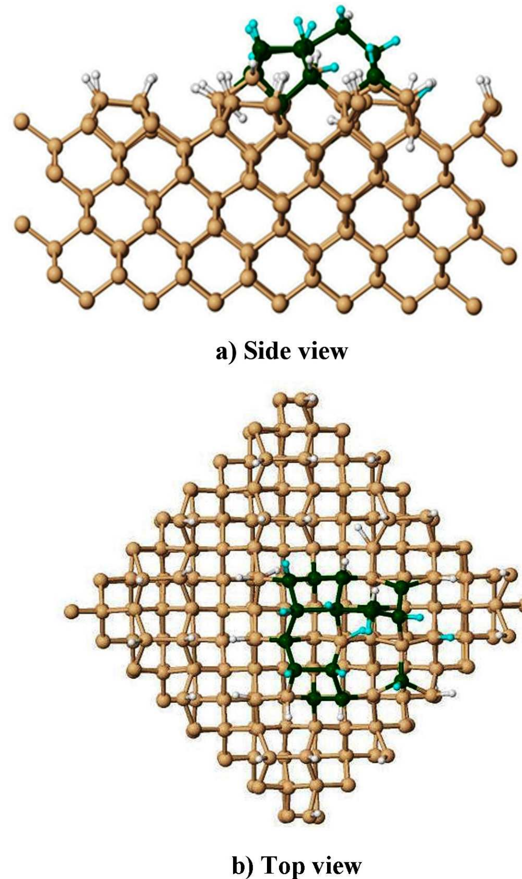

FIGURE 5.5: Side and top view of the atomic configuration after cooling down the system to the experimental temperautre of 373 K in the case where the $Si_{15}H_{10}$ cluster approached the surface at 373 K with an impact energy of 5.3 eV/atom resulting in a local equilibrated heating at the impact region to 1600 K and the reoganisation of cluster and substrate atoms at the impact region to the perfectly ordered stucture of the initial substrate at about 78.70 ps.

To investigate the structure of the cluster before and after the substrate impact, we calculated the radial distribution functions (RDFs) of the amorphous cluster at 300 K (before the impact), of the cluster including the immediate neighbor substrate atoms at 1 ps after the impact, and after the cooling down to 373 K. The RDF graph of the cluster and substrate atoms touching the cluster after cooling down to 373 K is quite consistent with the one of crystalline bulk silicon (see Fig. 5.6d).

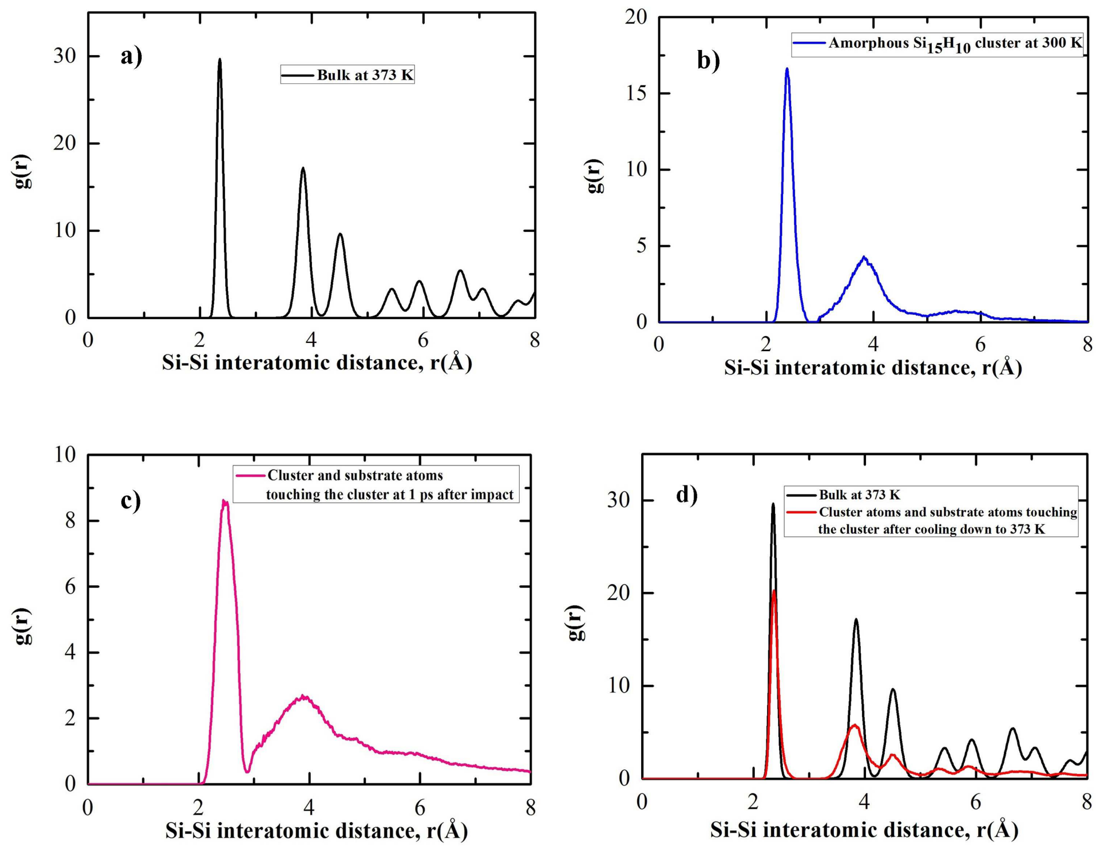

Figure 5.6: RDFs of: a) bulk silicon at 373 K; b) the amorphous $Si_{15}H_{10}$ cluster at 300 K before impact; c) cluster and substrate atoms touching the cluster at 1 ps after the impact; d) cluster and substrate atoms touching the cluster after the cooling down to 373 K. The RDF graph of the cluster and substrate atoms touching the cluster after cooling down to 373 K is quite consistent with the one of crystalline bulk silicon.

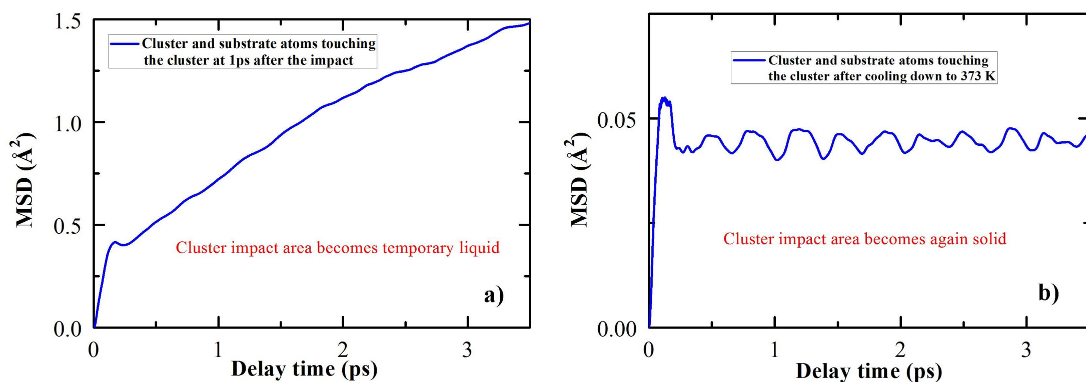

Figure 5.7: MSDs of silicon atoms of the $Si_{15}H_{10}$ cluster and substrate silicon atoms touching the cluster: a) at 1 ps after the impact; b) after the cooling down to 373 K.

To investigate the phase state of the cluster after the impact and after the cooling down to 373 K, we calculated the mean square displacement functions (MSDs). As can be seen on Fig. 5.7, the MSD graphs of the cluster and substrate atoms touching the cluster behave like a liquid state at 1 ps after the impact and like a solid state after the cooling down to 373 K.

Following this observation, we have to answer the question if we need 5.30 eV/atom or 79.5 eV total kinetic energy (since there are 15 silicon atoms in the amorphous $Si_{15}H_{10}$ cluster) to obtain epitaxial growth of thin silicon films by means of cluster deposition. Therefore, we have investigated deposition processes of hydrogenated silicon clusters which are smaller and bigger than $Si_{15}H_{10}$. To this end, we chose Si_8H_{12}, $Si_{28}H_{13}$, and $Si_{29}H_{24}$.

5.3.2 Deposition of Si_8H_{12} clusters on H-terminated Si(100)-(2×1) surfaces

We have examined the deposition of amorphous Si_8H_{12} clusters on H-terminated Si(100)-(2×1) surfaces at different substrate temperatures (373, 473, and 573 K) with two impact energies 5.23 eV/atom and 9.95 eV/atom; the latter corresponding to a total kinetic energy of 79.5 eV. All trajectories are followed for 200 ps. For all investigated cases, we have observed that the cluster partly or fully penetrates into the surface lattice after the impact with the substrate surface to form a disordered structure consisting of cluster atoms and local substrate atoms from the impact region. At about 0.4 ps, those atoms start to rearrange. Some cluster atoms insert themselves into lattice positions. The other cluster atoms together with the local substrate atoms move back to the substrate surface. During the arrangement process on the surface, some of those atoms also find epitaxial positions.

In the case where Si_8H_{12} clusters approach the substrate at 373 K with an impact energy of 5.23 eV/atom, we have observed 5 out of 8 silicon atoms find epitaxial positions at about 3 ps after the surface impact. Thereafter, those atoms did not change their bonds with their neighbors anymore. The temperature of the cluster atoms and the substrate atoms touching the cluster in the impact region directly reached 2000 K after the impact and rapidly decreased to 990 K. We thereafter cooled down the temperature of all atoms to 373 K by employing the Berendsen thermostat to the substrate. Figure 5.8 presents the atomic configurations after the cooling down. The MSD graphs of those atoms are shown in Fig. 5.9. At 1 ps after the impact, the MSD graph of the cluster silicon atoms and the substrate silicon atoms touching the cluster indicates an intermediate state between liquid and solid phases, while it displays a solid state character after the cooling down to 373 K.

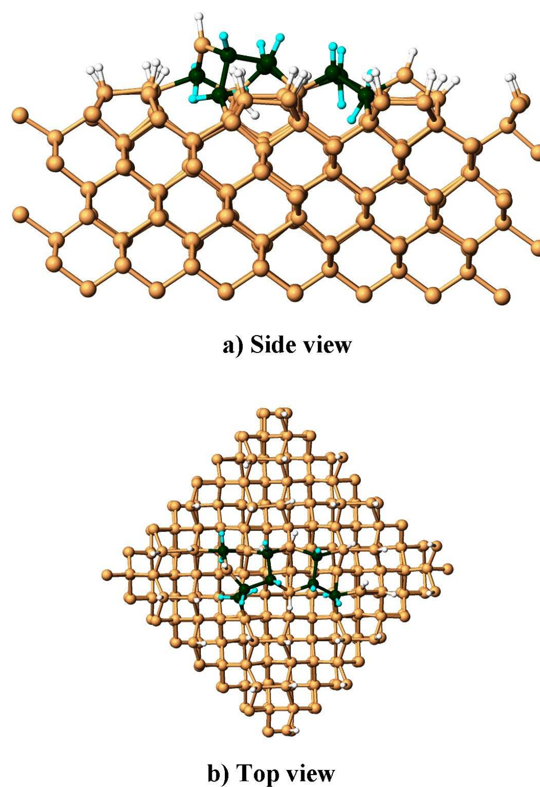

FIGURE 5.8: Side and top view of the atomic configuration after the cooling down to 373 K for the case of the Si_8H_{12} cluster approaching the substrate with an impact energy of 5.23 eV/atom.

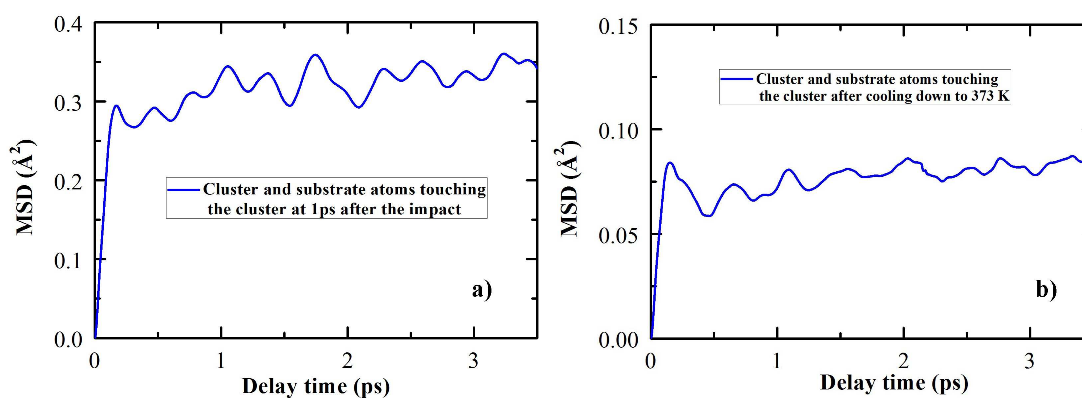

FIGURE 5.9: MSDs of silicon atoms of the Si_8H_{12} cluster and substrate silicon atoms touching the cluster for the case of the Si_8H_{12} cluster approaching the substrate with an impact energy of 5.23 eV/atom: a) at 1 ps after the impact; b) after the cooling down to 373 K.

In the case where Si_8H_{12} clusters approach the substrate at 473 K with an impact energy of 5.23 eV/atom, there are only 3 out of 8 silicon atoms that find epitaxial positions. The temperature of the cluster atoms and the substrate atoms touching the cluster in the impact region directly reached 3000 K after the impact and rapidly decreased to 1050 K. Figure 5.10 shows the atomic configuration at 200 ps after the collision.

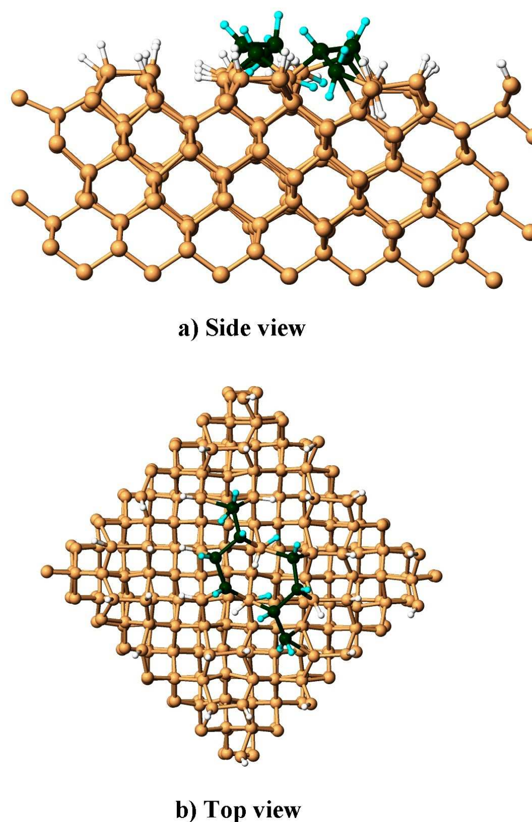

Figure 5.10: Side and top view of the atomic configuration at 200 ps after the collision for the case of the Si_8H_{12} cluster approaching the substrate at 473 K with an impact energy of 5.23 eV/atom.

In the case where Si_8H_{12} clusters approach the substrate at 573 K with an impact energy of 5.23 eV/atom, 6 out of 8 silicon atoms found epitaxial positions. The temperature of the cluster atoms and the substrate atoms touching the cluster in the impact region directly reached 3000 K after the impact and rapidly decreased to 1220 K. We thereafter cooled down the temperature of all atoms to 573 K by employing a Berendsen thermostat to the substrate. The atomic configurations after the cooling down are presented in Fig. 5.11. The MSD graphs of the cluster silicon atoms and the substrate silicon atoms touching the cluster exhibit a liquid state at 1 ps after the impact and a solid state after the cooling down to 573 K (see Fig. 5.12).

In the case where Si_8H_{12} clusters approach the substrate at 373 K with an impact energy of 9.95 eV/atom corresponding again to a total kinetic energy of 79.5 eV, we

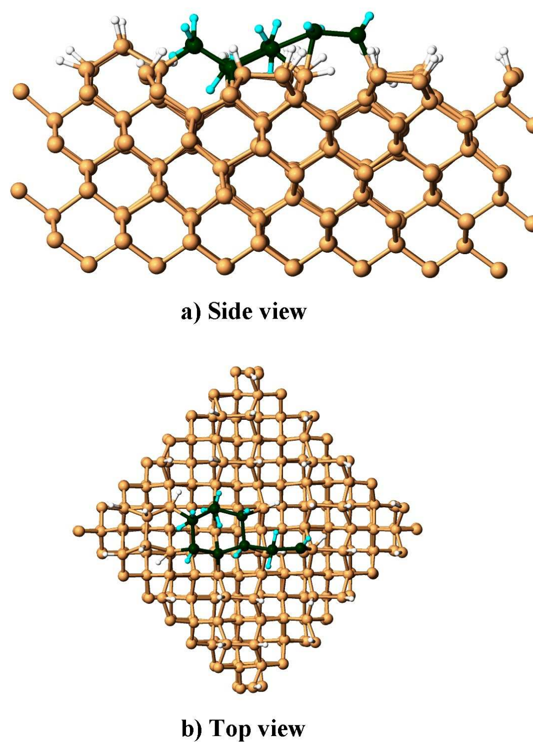

FIGURE 5.11: Side and top view of the atomic configuration after the cooling down to 573 K for the case of the Si_8H_{12} cluster approaching the substrate with an impact energy of 5.23 eV/atom.

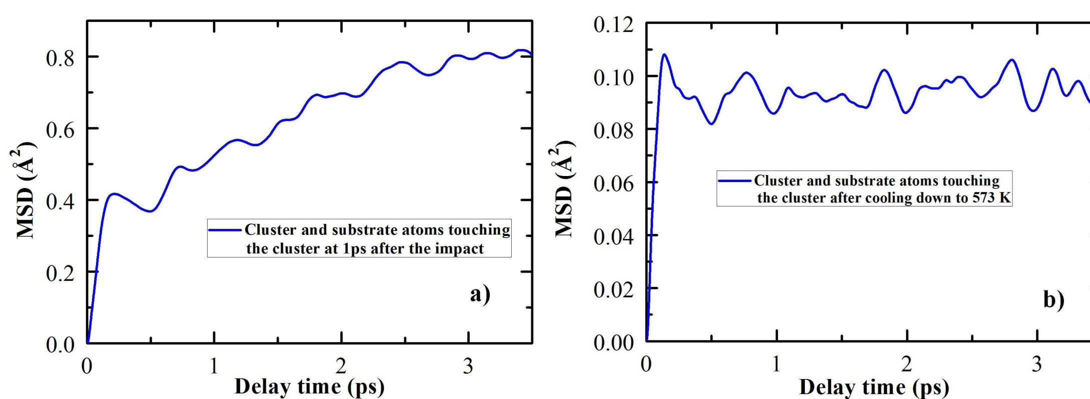

FIGURE 5.12: MSDs of silicon atoms of the Si_8H_{12} cluster and substrate silicon atoms touching the cluster for the case of the Si_8H_{12} cluster approaching the substrate with an impact energy of 5.23 eV/atom: a) at 1 ps after the impact; b) after the cooling down to 573 K.

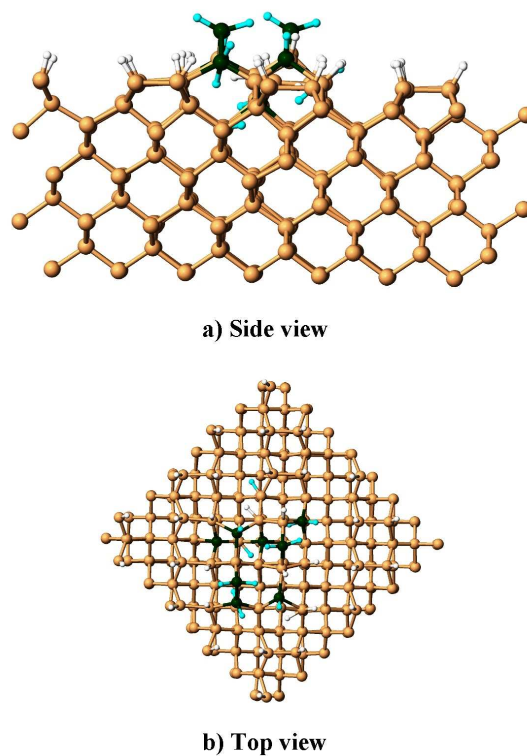

FIGURE 5.13: Side and top view of the atomic configuration after the cooling down to 373 K for the case of the Si_8H_{12} cluster approaching the substrate with an impact energy of 9.95 eV/atom.

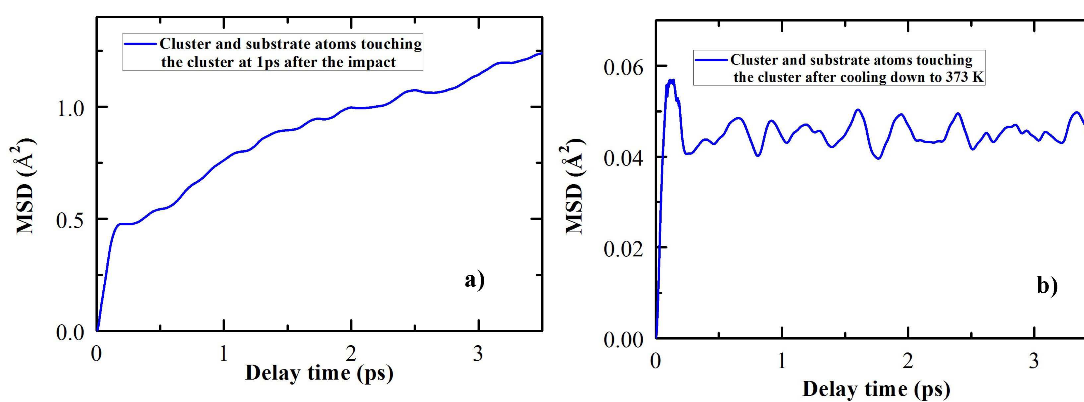

FIGURE 5.14: MSDs of silicon atoms of the Si_8H_{12} cluster and substrate silicon atoms touching the cluster for the case of the Si_8H_{12} cluster approaching the substrate with an impact energy of 9.95 eV/atom: a) at 1 ps after the impact; b) after the cooling down to 373 K.

have observed all 8 out of 8 silicon atoms find epitaxial positions at about 52 ps after the surface impact. Two cluster silicon atoms insert themselves in the first layer below the initial surface substrate. The temperature of the cluster atoms and the substrate atoms touching the cluster in the impact region directly reached 3000 K after the impact and rapidly decreased to 1540 K. We thereafter cooled down the temperature of all atoms to 373 K by employing again the Berendsen thermostat to the substrate. Figure 5.13 shows the atomic configuration after the cooling down. The MSD graphs of cluster silicon atoms and substrate silicon atoms touching the cluster exhibit a liquid state at 1 ps after the impact, while a solid state is observed for those atoms after the cooling down to 373 K (see Fig. 5.14).

In the case where Si_8H_{12} clusters approach the substrate at 473 K with an impact energy of 9.95 eV/atom, all 8 out of 8 silicon atoms found epitaxial positions at about 138 ps after the surface impact. One cluster silicon atom inserts itself in the first layer below the initial surface substrate. The temperature of the cluster atoms and the substrate atoms touching the cluster in the impact region directly reached 3000 K after the impact and rapidly decreased to 1620 K. We thereafter cooled down the temperature of all atoms to 473 K by employing the Berendsen thermostat to the substrate. Figure 5.15 presents the atomic configurations after the cooling down. The MSD graphs of cluster silicon atoms and substrate silicon atoms touching the cluster shown in Fig. 5.16 display a liquid state at 1 ps after the impact and a solid state after the cooling down to 473 K.

In the case where Si_8H_{12} clusters approach the substrate at 573 K with an impact energy of 9.95 eV/atom, 2 out of 8 silicon atoms found epitaxial positions. Two cluster silicon atoms insert themselves in the first layer below the initial surface substrate. The temperature of the cluster atoms and the substrate atoms touching the cluster in the impact region directly reached 3500 K after the impact and rapidly decreased to 1720 K. Figure 5.17 shows the atomic configuration at 200 ps after the collision.

The above observations for Si_8H_{12} and $Si_{15}H_{10}$ cluster deposition lead us to the following conclusions: The total impact energy of about 79.5 eV seems to play a more important role than the impact energy per atom for the epitaxial growth. An impact energy of about 5.3 eV/atom for Si_8H_{12} leads to a total impact energy of about 42.0 eV resulting in temperatures for both the cluster atoms and the substrate atoms touching the cluster that rapidly equilibrate to temperatures smaller than 1220 K for all three investigated substrate temperatures. This impact energy is apparently not high enough to access epitaxial positions for all cluster silicon atoms. From the investigations of the phase states of cluster silicon atoms and substrate silicon atoms touching the cluster shown in the MSD graphs right after the cluster-surface impact, we tentatively suggest that a temporary phase transition to the liquid state is necessary for the cluster-catalyzed epitaxial growth of thin silicon films.

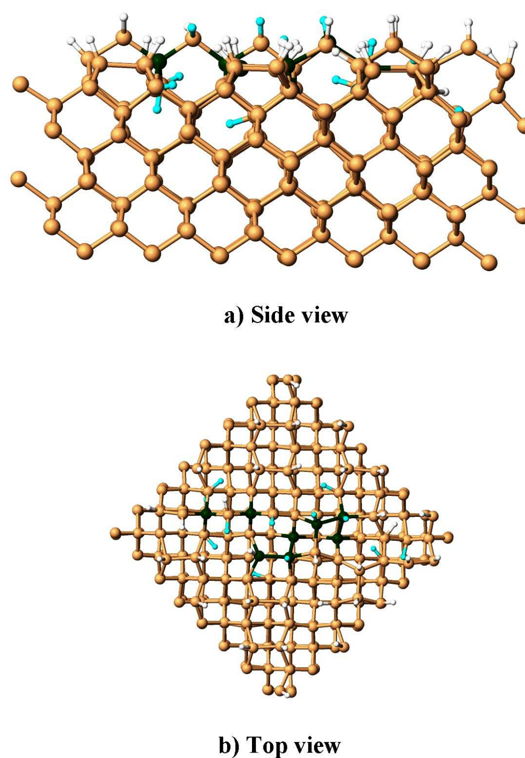

FIGURE 5.15: Side and top view of the atomic configuration after the cooling down to 473 K for the case of the Si_8H_{12} cluster approaching the substrate at 473 K with an impact energy of 9.95 eV/atom.

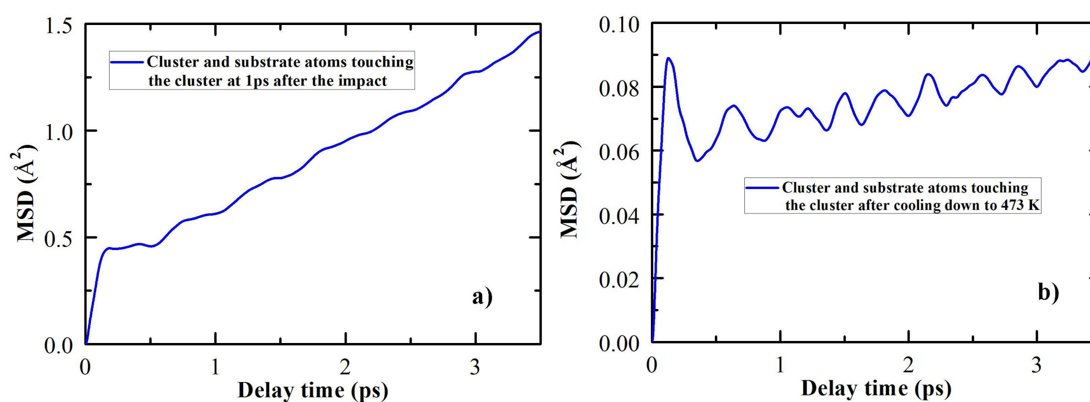

FIGURE 5.16: MSDs of silicon atoms of the Si_8H_{12} cluster and substrate silicon atoms touching the cluster for the case of the Si_8H_{12} cluster approaching the substrate at 473 K with an impact energy of 9.95 eV/atom: a) at 1 ps after the impact; b) after the cooling down to 473 K.

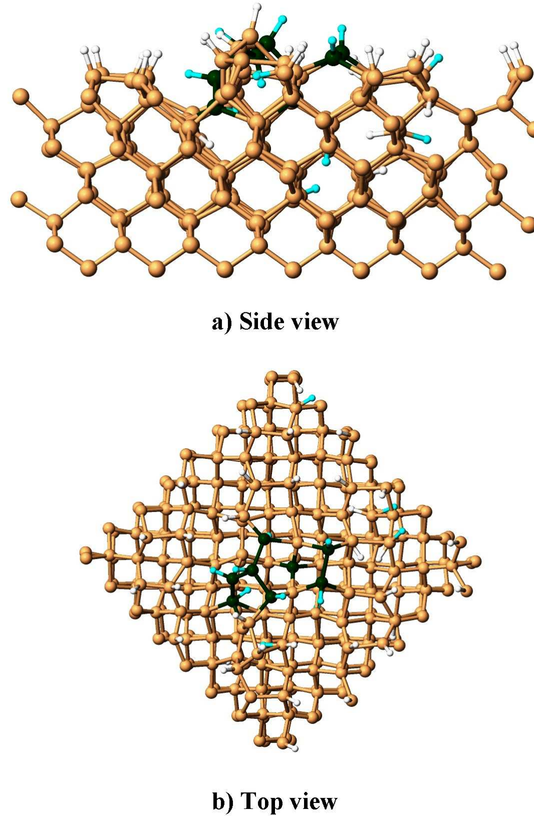

FIGURE 5.17: Side and top view of the atomic configuration at 200 ps after the collision for the case of the Si_8H_{12} cluster approaching the substrate at 573 K with an impact energy of 9.95 eV/atom.

To confirm our conclusion that it is the total kinetic energy of 79.5 eV and not the kinetic energy per atom of 5.3 eV that is necessary to achieve epitaxial growth and our suggestion mentioned above, we simulate in the following the deposition of a considerably larger amorphous cluster ($Si_{28}H_{13}$) for surface temperatures of 373 and 573 K.

5.3.3 Deposition of $Si_{28}H_{13}$ clusters on H-terminated Si(100)-(2×1) surfaces

To search for epitaxial growth, we deposited the $Si_{28}H_{13}$ cluster on a H-terminated Si(100)-(2×1) surface at a substrate temperature of 373 K and changed the impact energies due to its previously observed strong influence on the cluster deposition process. There are five impact energies that were investigated: 2.46, 2.84, 3.08, 3.77, and 5.37 eV/atom. We note here that an impact energy of 2.84 eV/atom corresponds to a total impact energy of about 79.5 eV and that 5.37 eV/atom is the impact energy where the epitaxial growth was obtained from $Si_{15}H_{10}$ cluster deposition. We follow all trajectories for 200 ps.

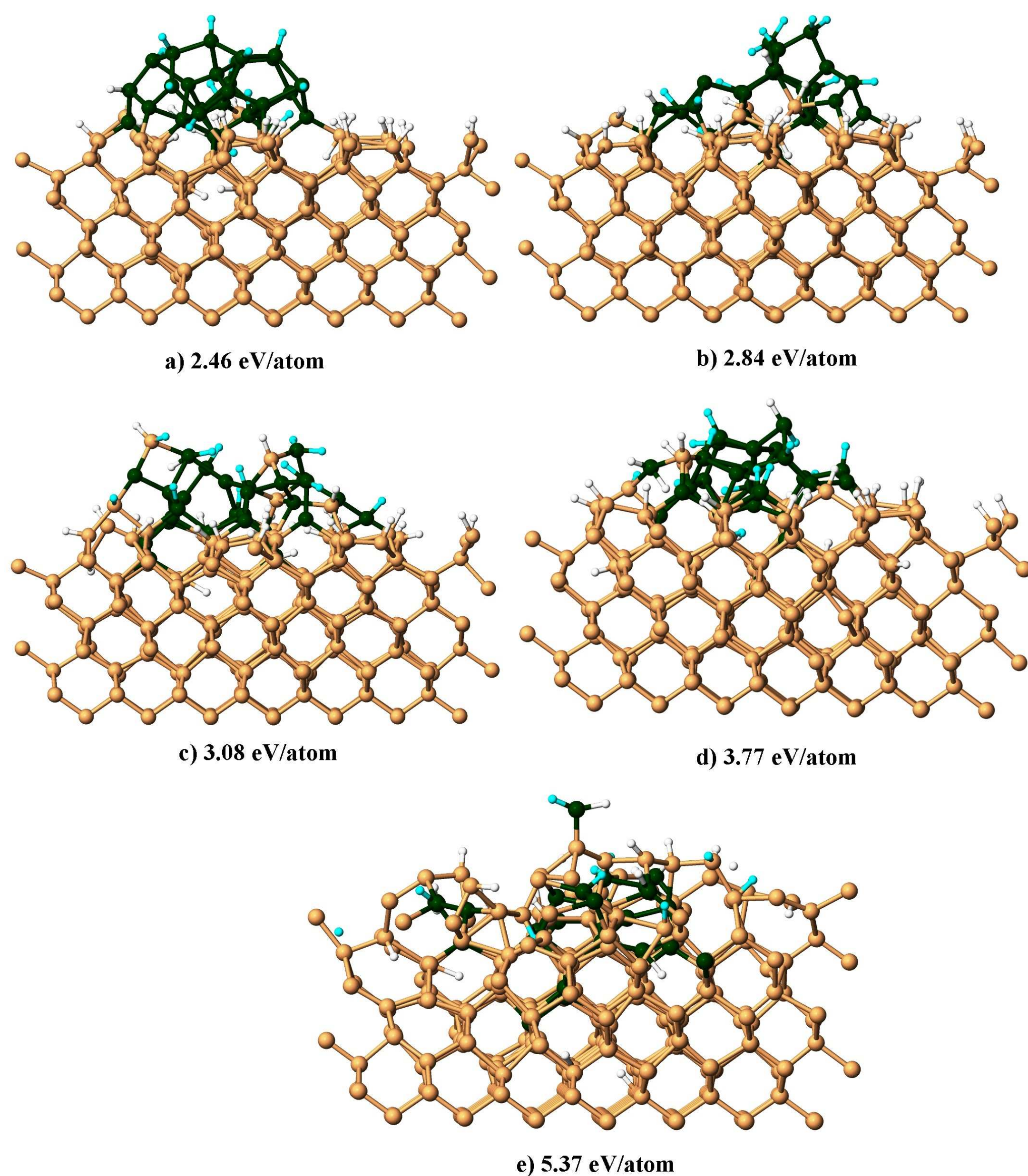

FIGURE 5.18: Snapshots of the atomic configurations at 200 ps after the impact of the $Si_{28}H_{13}$ cluster onto the silicon surface for various impact energies: a) 2.46, b) 2.84, c) 3.08, d) 3.77, and e) 5.37 eV/atom. The substrate temperature is always at 373 K.

For impact energies of 2.46, 2.84, and 3.08 eV/atom, the $Si_{28}H_{13}$ cluster partly penetrates into the substrate and creates a temporary disorder of cluster and substrate atoms in the substrate. At about 0.8 ps after the impact, those atoms start to reconstruct. For the impact energy of 2.46 eV/atom, all cluster silicon atoms move back to the surface at about 15 ps after the impact. For the impact energies of 2.84 and 3.08 eV/atom, some of the cluster silicon atoms insert themselves into lattice positions. The other cluster silicon atoms together with some substrate silicon atoms go to the top of the surface. The substrate lattice totally recovers after 20 and 30 ps for impact energies of 2.84 and 3.08 eV/atom, respectively. We calculated the temperatures of cluster atoms and substrate atoms touching the clusters after the collision for three cases. Shortly after the impact, those temperatures are 1380, 1550, and 1590 K for the impact energies of 2.46, 2.84, and 3.08 eV/atom, respectively. The corresponding atomic configurations at 200 ps after the impact exhibit that the number of silicon atoms that accessed epitaxial positions are 5 out of 28 (Fig. 5.18a), 21 out of 28 (Fig. 5.18b), and 12 out of 28 (Fig. 5.18c).

For the impact energy of 3.77 eV/atom, the $Si_{28}H_{13}$ cluster completely penetrates into the substrate, consequently a temporary disorder of cluster and substrate atoms is formed. The equilibrated temperature in this region is about 1810 K. Then, the atoms start to rearrange themselves. At about 50 ps after the impact, the substrate lattice totally recovers from the cluster damage with the insertion of some cluster silicon atoms in some lattice positions. At 200 ps after the collision, 10 out of 28 silicon atoms are found in epitaxial positions (see Fig. 5.18d).

An impact energy of 5.3 eV/atoms seriously damages both the cluster and the substrate due to the extremely high temperature of about 5000 K that still remains as high as 2250 K after equilibration resulting in silicon and hydrogen atoms evaporating from the surface. Figure 5.18e shows the remaining surface after this etching.

In the following, we studied the influence of substrate temperature for the epitaxial growth. To this end, the $Si_{28}H_{13}$ cluster was deposited on a H-terminated Si(100)-(2×1) surface with an impact energy of 2.84 eV/atom at two different substrate temperatures of 373 and 573 K. The structural evolution of the cluster during the deposition processes for the two cases are quite similar. This observation is consistent with the investigations in Ref. [35]. The details of the structural evolution for the case of a substrate temperature of 373 K were described above. With a substrate temperature of 573 K, two cluster silicon atoms insert themselves into lattice positions at the first layer below the initial surface substrate (see Fig. 5.19b). The temperatures of the cluster atoms and the substrate atoms touching the cluster are 1550 and 1770 K for the two substrate temperatures of 373 and 573 K, respectively. At 200 ps after the collision, the numbers of silicon atoms that accessed epitaxial positions are 21 out of 28 for a substrate temperature of 373 K and 18 out of 28 for a substrate temperature of 573 K (see Fig. 5.19).

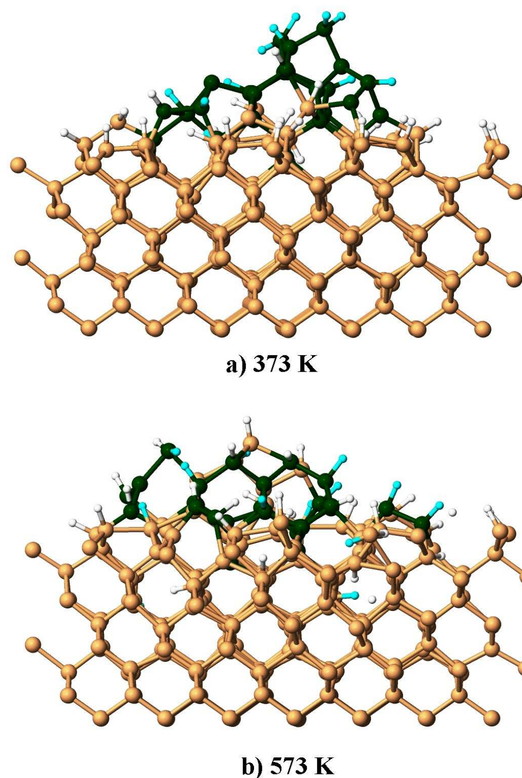

FIGURE 5.19: Snapshots of the atomic configurations at 200 ps after the impact of the $Si_{28}H_{13}$ cluster with the surface for different substrate temperatures: a) 373 K; b) 573 K. The impact energy is always 2.84 eV/atom.

We have not observed any trajectories in which all 28 silicon atoms found epitaxial positions after the cluster-surface deposition. The best result achieved so far was 21 out of 28 silicon atoms accessing epitaxial positions when the $Si_{28}H_{13}$ cluster deposited on a crystalline silicon substrate at a substrate temperature of 373 K with an impact energy of 2.84 eV/atom. In the following, we will scrutinize one case which resulted in a low epitaxial efficiency; *i.e.*, a small number of silicon atoms settling in epitaxial positions: impact energy of 2.46 eV/atoms and a substrate temperature of 373 K. In this case, we have observed that, after coming back to the surface of the substrate from a disordered atom arrangement inside the substrate lattice, the cluster and substrate silicon atoms build an amorphous entity on top of the lattice that remained unchanged during the rest of our simulation preventing the involved silicon atoms to rearrange themselves into epitaxial positions.

So far all three employed clusters had amorphous structures. Therefore, we would like to know if there is something different for the epitaxial growth mechanisms of thin silicon films from amorphous and crystalline clusters. The deposition process of the crystalline $Si_{29}H_{24}$ cluster is thus simulated in the following to answer this question in order to clarify the mechanisms leading to epitaxial growth.

5.3.4 Deposition of $Si_{29}H_{24}$ clusters on H-terminated Si(100)-(2×1) surfaces

First, we deposit the $Si_{29}H_{24}$ clusters on a H-terminated Si(100)-(2×1) surface with various impact energies at a substrate temperature of 373 K. The investigated impact energies are 2.74, 3.03, 3.67, and 5.31 eV/atom; note that the impact energy of 2.74 eV/atom corresponds to a total impact energy of 79.5 eV. We follow all trajectories again for 200 ps.

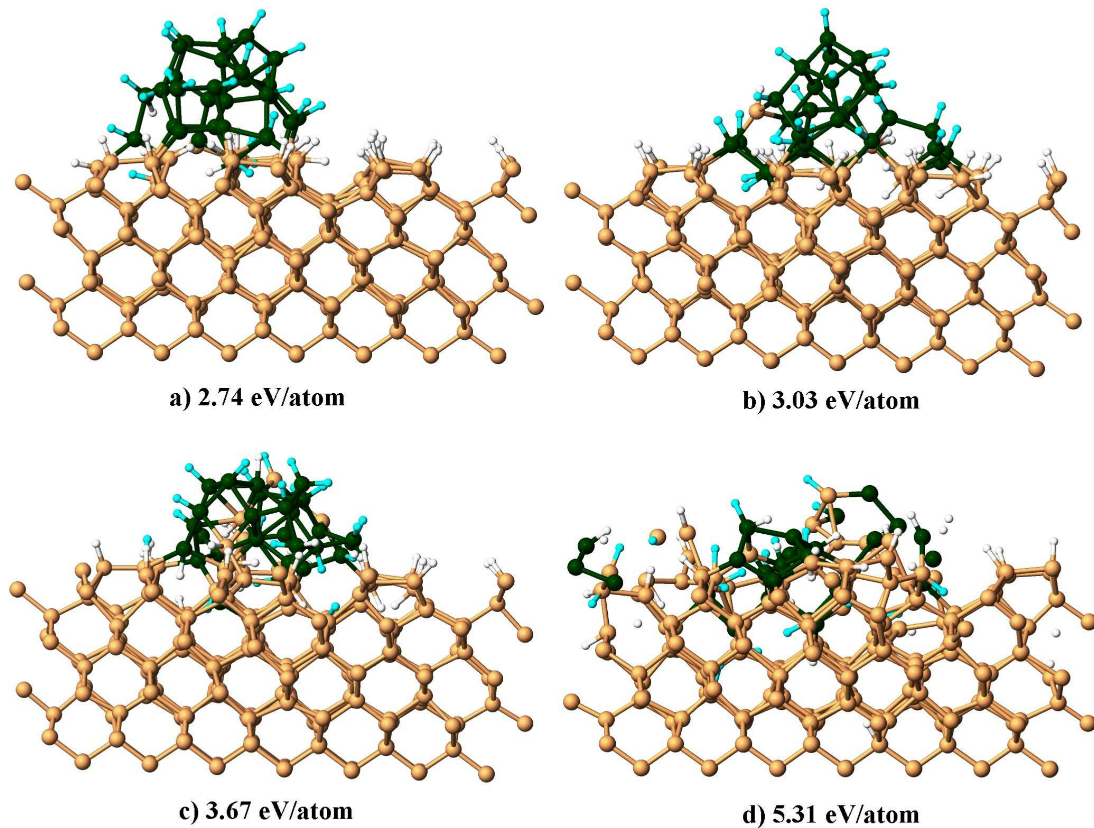

FIGURE 5.20: Snapshots of the atomic configurations at 200 ps after the impact of the $Si_{29}H_{24}$ cluster with the surface for various impact energies: a) 2.74, b) 3.03, c) 3.67, and d) 5.31 eV/atom. The substrate temperature is always 373 K.

For the impact energies of 2.74 and 3.03 eV/atom, the cluster partly penetrates into the substrate lattice causing a temporary substrate damage: the cluster atoms and substrate atoms at the impact region form a disordered arrangement. At about 0.8 ps after the impact, these disordered atoms start to reconstruct. All cluster silicon atoms move back to the surface at about 3 ps for the case of an impact energy of 2.74 eV/atom and at about 7 ps for an impact energy of 3.03 eV/atom. The equilibrated temperatures of cluster atoms and substrate atoms touching the cluster after the collision are about 1340 and 1440 K for the impact energies of 2.74 and 3.03 eV/atom, respectively. Figures

5.20 a and b present the atomic configurations for the two impact energies indicating that at 200 ps after the impact 5 out of 29 silicon atoms are found in epitaxial positions for an impact energy of 2.74 eV/atom, while there are 13 out of 29 silicon atoms for an impact energy of 3.03 eV/atom.

For the impact energy of 3.67 eV/atom, the cluster completely penetrates into the substrate lattice. A temporary disorder consisting of cluster atoms and substrate atoms is formed inside the substrate lattice. After 0.8 ps, those atoms start to rearrange and one cluster silicon atom is found to insert itself into a lattice position. The other cluster silicon atoms diffuse back to the surface at about 12 ps after the impact. The equilibrated temperature of the cluster atoms and substrate atoms touching the cluster is about 1663 K. At 200 ps after the impact, 5 out of the 29 silicon atoms found epitaxial positions (see Fig. 5.20c).

A seriously damaged silicon surface was obtained in the case of an impact energy of 5.31 eV/atom due to the very high temperature in the impact region which exceeds 5000 K and rapidly equilibrates to 2140 K . This high temperature again leads to silicon and hydrogen atom evaporating from the silicon surface. The atomic configuration at 200 ps after the impact shown in Fig. 5.20d is the remaing of the silicon surface after this etching.

Second, all $Si_{29}H_{24}$ clusters deposit with an impact energy of 2.74 eV/atom on H-terminated Si(100)-(2×1) surfaces at different substrate temperatures of 373, 473, and 573 K. There is no significant difference in the structural evolution of the cluster during the deposition processes for the three investigated cases. The details of the deposition process where the cluster approached the substrate at 373 K with an impact energy of 2.74 eV/atom are mentioned above. Due to the initial substrate temperature differences, the equilibrated temperatures of the cluster atoms and the substrate atoms touching the cluster are 1340, 1400, and 1530 K for the substrate temperature of 373, 473, and 573 K, respectively. The corresponding atomic configurations at 200 ps after the impact shown in Fig. 5.21 indicate that the number of silicon atoms that accessed epitaxial positions is 5, 4, and 9 out of 29 for the three different substrate temperatures.

Whatever combination of incident kinetic energy and substrate temperature we have investigated, we could never observe a case of complete epitaxial growth. The epitaxial growth efficiency is actually quite low in comparison to our studies with amorphous clusters (the best case was 13 out of 29 silicon atoms that could access epitaxial positions for an impact energy of 3.03 eV/atoms and a substrate temperature of 373 K). Since all simulations of above were performed with a normal incidence angle, we were wondering if a non-zero incidence angle could not help in spreading out the cluster over the substrate to facilitate the access to epitaxial positions for the cluster atoms. This idea was triggered by previous studies concerning the surface scattering of large rare gas clusters [115–117].

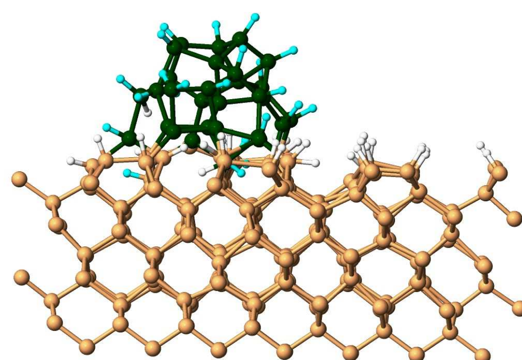

a) 373 K

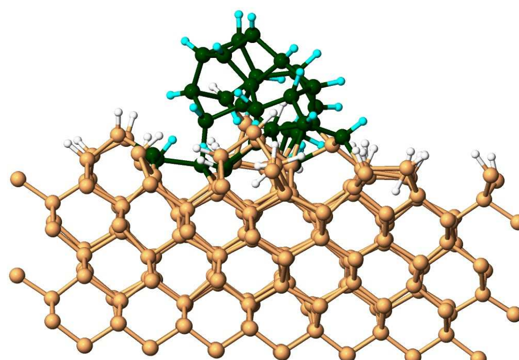

b) 473 K

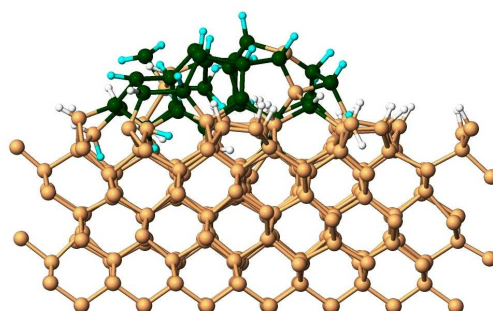

c) 573 K

FIGURE 5.21: Snapshots of the atomic configurations at 200 ps after the impact of the $Si_{29}H_{24}$ cluster with the surface for various substrate temperatures: a) 373, b) 473, and c) 573 K. The impact energy is always 2.74 eV/atom.

We deposited the crystalline $Si_{29}H_{24}$ cluster on a H-terminated Si(100)-(2×1) surface with a substrate temperature of 473 K and an impact energy of 3.67 eV/atom and we chose three different incidence angles of 0, 30, and 45 degrees as measured from the surface normal direction.

In the case of normal incidence angle, the cluster completely penetrates into the substrate and the cluster atoms together with the local substrate atoms form a highly disordered arrangement inside of the substrate lattice. At 0.8 ps after the impact, those atoms start to rearrange. At 15 ps after the impact, most cluster atoms and some substrate atoms move back to the surface of the substrate. One cluster atom inserts itself into the second layer of the substrate lattice. The equilibrated temperature of the cluster atoms and substrate atoms touching the cluster is now 1750 K. Figure 5.22 presents the structural evolution of the cluster during the deposition process. At 200 ps after the impact, 6 out of 29 silicon atoms take epitaxial positions.

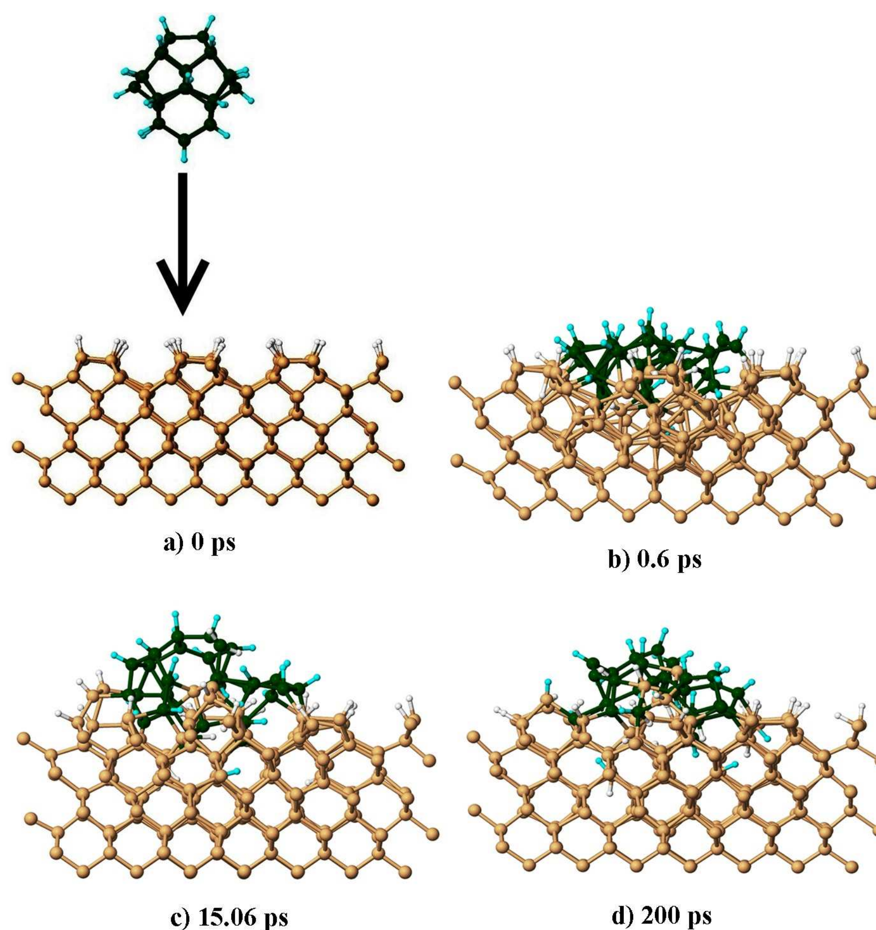

FIGURE 5.22: Snapshots of atomic configurations at various times during the $Si_{29}H_{24}$ cluster surface collision with an impact energy of 3.67 eV/atom, a substrate temperature of 473 K, and a normal incidence angle.

Next, the $Si_{29}H_{24}$ cluster approaches the crystalline silicon substrate again with an impact energy of 3.67 eV/atom, but with an incidence angle of 30 degrees. At about 0.38 ps the cluster arrives on the substrate surface. Thereafter, the cluster partly penetrates into the substrate lattice and partly spreads out on the substrate surface. Due to the impact, the cluster loses its crystalline structure. Cluster and substrate atoms form an amorphous structure thereafter (see Fig. 5.23c). Those atoms start to rearrange, and at about 148 ps after the impact, 24 out of 29 silicon atoms found epitaxial positions. The temperature of the cluster atoms and substrate atoms touching the cluster exceeds 3000 K after the impact and rapidly equilibrates to 1680 K (see Fig. 5.24). To simulate the experimental situation, we then cool down the whole system to 473 K by using the Berendsen thermostat. The atomic configuration after the cooling down is presented in Fig. 5.25.

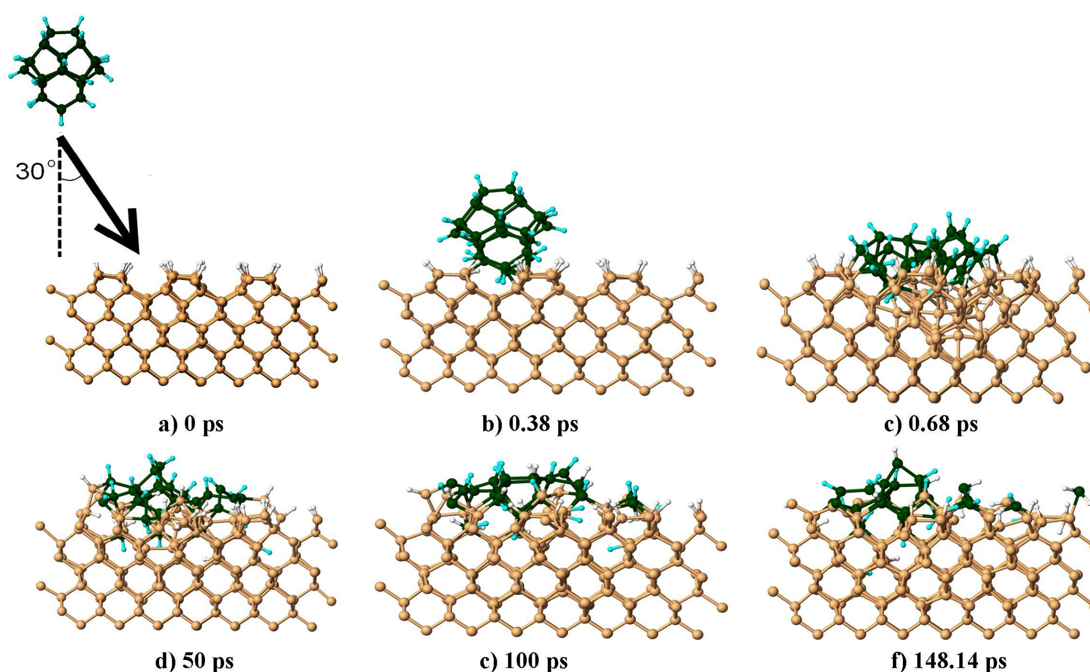

FIGURE 5.23: Snapshots of atomic configurations at various times during the $Si_{29}H_{24}$ cluster surface collision with an impact energy of 3.67 eV/atom, a substrate temperature of 473 K, and an incidence angle of 30 degrees.

To investigate the structure of the cluster after the substrate impact, we calculated the RDFs of the cluster including the immediate neighbor substrate atoms at 1 ps after the impact, and after the cooling down to 473 K. The RDF graph shown in Fig. 5.26a indicates that cluster atoms and substrate atoms touching the cluster are in a disordered structure at 1 ps as shown in the structural evolution of the cluster after the surface impact observed in Fig. 5.23. The ordered structure of those atoms after the cooling down to 473 K can be seen at the RDF graph in Fig. 5.26b. The RDF of bulk silicon

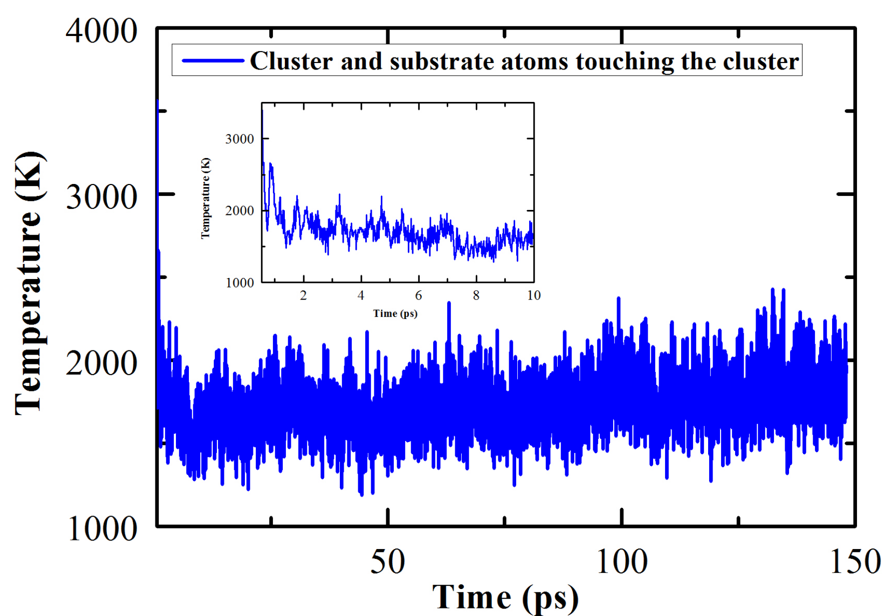

FIGURE 5.24: Time evolution of the instantaneous temperature of atoms belonging to both the initial $Si_{29}H_{24}$ cluster and the substrate in the immediate vicinity of the cluster after the impact.

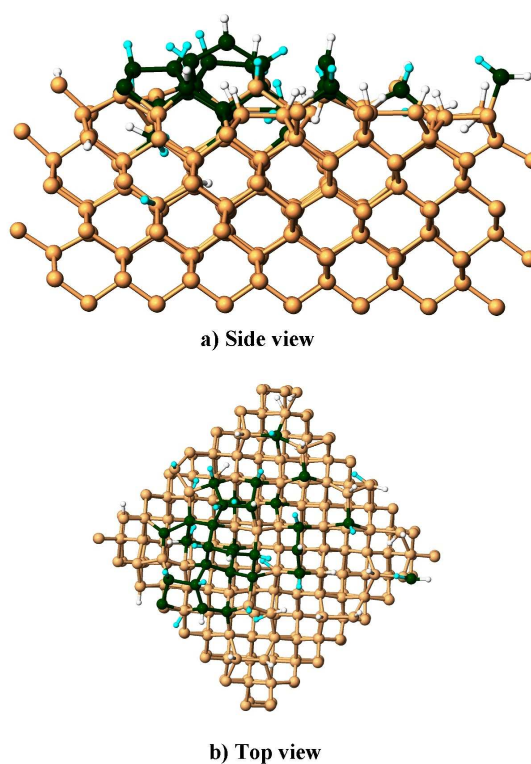

FIGURE 5.25: Side and top view of the atomic configuration after the cooling down to 473 K for the case of the $Si_{29}H_{24}$ cluster approaching the surface at 473 K with an impact energy of 3.67 eV/atom and an incidence angle of 30 degrees.

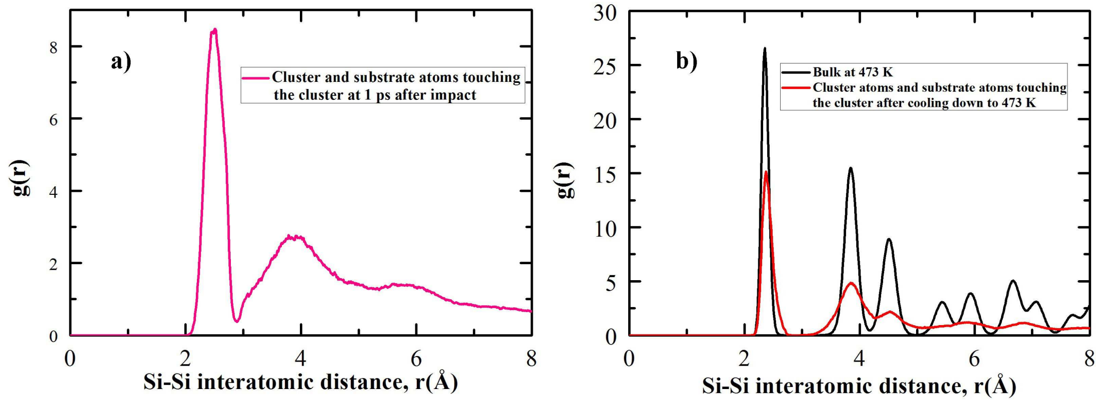

FIGURE 5.26: RDFs of silicon atoms of the $Si_{29}H_{24}$ cluster and substrate atoms touching the cluster: a) at 1 ps after the impact; b) after the cooling down to 473 K for the case of the $Si_{29}H_{24}$ cluster approaching the surface at 473 K with an impact energy of 3.67 eV/atom and an incidence angle of 30 degrees.

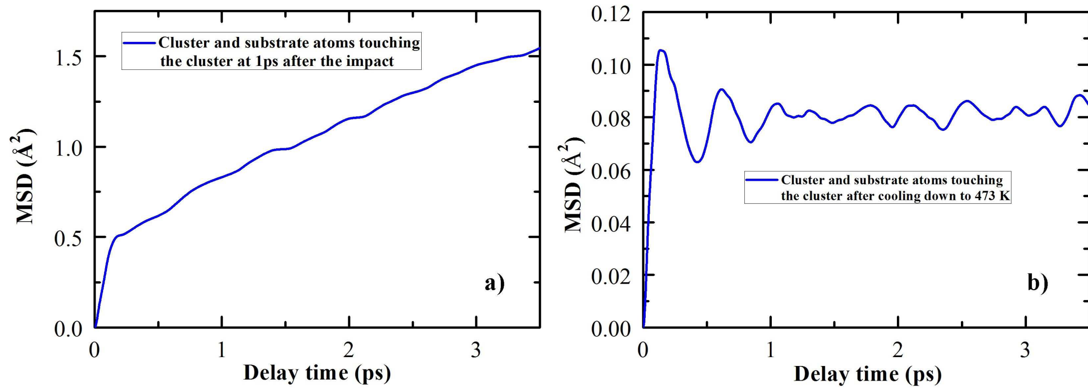

FIGURE 5.27: MSDs of silicon atoms of the $Si_{29}H_{24}$ cluster and substrate atoms touching the cluster for the case of the $Si_{29}H_{24}$ cluster approaching the surface at 473 K with an impact energy of 3.67 eV/atom and an incidence angle of 30 degrees: a) at 1 ps after the impact; b) after the cooling down to 473 K.

at 473 K is drawn for comparison. The RDF graph after the cooling down to 473 K is quite consistent with the RDF of bulk silicon at 473 K.

To determine the phase state of the cluster silicon atoms and substrate atoms touching the cluster, we investigated the MSDs of those silicon atoms at 1 ps after the impact and after the cooling down to 473 K. As shown in Fig. 5.27, the MSD graph at 1 ps after the impact displays a liquid-like behavior, while the MSD graph after the cooling down exhibits a solid-like state.

For the incidence angle of 45 degrees, the $Si_{29}H_{24}$ cluster arrives on the substrate surface with an impact energy of 3.67 eV/atom at about 0.44 ps. Thereafter, the cluster partly penetrates and partly spreads out on the surface, therefore, totally loses its initial crystalline structure. The cluster atoms together with the local substrate atoms of the

impact region form an ill-defined disordered structure. Those atoms start to rearrange and at 200 ps after the impact, 17 out of 29 silicon atoms access epitaxial positions. The equilibrated temperature of the cluster atoms and substrate atoms touching the cluster is 1660 K. Figure 5.28 shows the snapshots of atomic configurations at various times during the cluster surface collision.

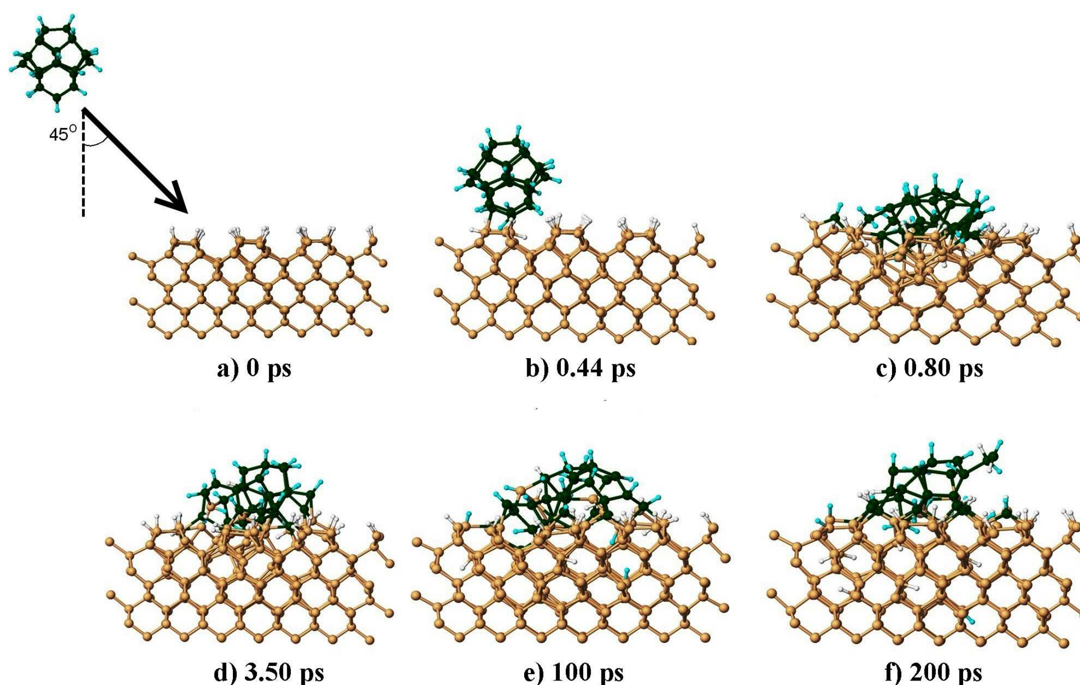

FIGURE 5.28: Snapshots of atomic configurations at various times during the $Si_{29}H_{24}$ cluster surface collision with an impact energy of 3.67 eV/atom, a substrate temperature of 473 K, and an incidence angle of 45 degrees.

From the above observations, we conclude that a non-normal incidence angle significantly facilitates the epitaxial growth as witnessed by the considerably higher epitaxial efficiency for the incidence angles of 30 and 45 degrees in comparison to normal incidence. Right after the cluster-surface impact, the cluster approaching the surface with a non-normal incidence angle spreads out on the surface together with a partial penetration into the substrate lattice, while the normal incidence cluster mostly penetrates into the substrate lattice only covering a surface area that is not much larger than the initial impact area.

5.4 Conclusions

We have performed an in-depth study on the deposition dynamics of hydrogenated silicon clusters on H-terminated Si(100)-(2×1) surfaces by controlling the impact parameters

governing the cluster-surface deposition process: impact energy, substrate temperature, and incidence angles. Four hydrogenated silicon clusters with different sizes (very small, small and moderate) and structures (amorphous and crystalline) have been employed.

With $Si_{15}H_{10}$ amorphous clusters, epitaxial growth has been observed in the case where the clusters approach the substrate with an impact energy of 5.3 eV/atom and a substrate temperature of 373 K. Investigations with the small Si_8H_{12} amorphous clusters indicate that the total impact energy of about 79.5 eV seems to play a more important role than the impact energy per atom (about 5.3 eV/atom) for the epitaxial growth. The total impact energy of 79.5 eV condition has been tested with bigger clusters ($Si_{28}H_{13}$ and $Si_{29}H_{24}$). Highly efficient epitaxial growth (*i.e.*, 21 out of 28 silicon atoms accessed epitaxial positions) has been achieved when the amorphous $Si_{28}H_{13}$ cluster deposits on a crystalline silicon substrate with an impact energy of 2.84 eV/atom (*i.e.*, again a total impact energy of 79.5 eV) with a substrate temperature of 373 K. The same conditions (impact energy of 2.74 eV/atom corresponding to a total impact energy of 79.5 eV and a substrate temperature of 373 K) were applied for the $Si_{29}H_{24}$ crystalline cluster. However, we only could obtain a very low epitaxial efficiency for the $Si_{29}H_{24}$ cluster (only 5 out of the 29 silicon atoms could access epitaxial positions). Hence, the total impact energy of 79.5 eV might be a necessary, but not a sufficient condition for high efficiency epitaxial growth.

By using normal incidence, we have observed that all cluster silicon atoms can find epitaxial positions (8 out of 8) for the Si_8H_{12} cluster and (15 out of 15) for the $Si_{15}H_{10}$ cluster for some specific conditions of impact energy and substrate temperature. However, we have not yet seen any complete epitaxial growth (*i.e.*, 100% of the cluster silicon atoms find epitaxial positions) for bigger clusters ($Si_{28}H_{13}$ and $Si_{29}H_{24}$) when those clusters were deposited with a normal incidence angle. Deposition of the $Si_{29}H_{24}$ cluster with non-normal incidence angles, however, shows very high efficiency for the epitaxial growth (24 out of 29 for an incidence angle of 30 degrees and 17 out of 29 for an incidence angle of 45 degrees, while there were only 6 out of 29 for normal incidence with the same impact energy of 3.67 eV/atom and a substrate temperature of 473 K for all three incidence angles). Therefore, we conclude that a non-normal incidence angle might significantly facilitate epitaxial growth and we tentatively suggest that the need for non-normal incidence increases with the size of the impinging clusters.

From our observations for the cases where we obtain epitaxial growth, we can describe a deposition process as follows. For both initially amorphous and crystalline clusters, the cluster partly or totally penetrates into the substrate lattice. Cluster atoms and local substrate atoms around the impact region then form a disordered structure. Subsequently, those atoms rearrange themselves and move back to the surface of the substrate. Some cluster silicon atoms might insert themselves into lattice positions during the period where the disordered structure is present inside the substrate lattice. Thereafter,

the silicon atoms rearrange themselves on the surface of the substrate and might settle down in epitaxial positions. From the temperature and MSD graphs calculated from the investigated trajectories we can conclude that a temporary phase transition to the liquid state is necessary for the cluster-catalyzed epitaxial growth of silicon thin films. This condition, however, seems to be sufficient only for the two smallest investigated impinging clusters. For larger clusters, the introduction of a non-normal incidence angle appears to be necessary to spread out the cluster on the substrate to permit a majority of the cluster atoms to get close to potential epitaxial positions that are not too far away from the top layer of the substrate.

Epitaxial growth of thin, but crystalline silicon films induced from the deposition of hydrogenated silicon clusters is a complicated process. Due to the small size of our model substrate, we could not investigate larger incidence angles as we had wished, *e.g.*, 60 and 75 degrees. Hence, we suggest as future work to construct a bigger system (both substrate and cluster) in order to further investigate the effect of non-normal incidence angles for getting high efficiencies for the cluster-induced epitaxial growth of silicon thin films.

Chapter 6

Conclusions and Perspectives

We have presented investigations concerning three processes performed in PECVD reactors during silicon thin film depositions. Previously, it was experimentally shown that hydrogenated silicon clusters/nanoparticles can be produced in the gas phase of PECVD reactors. The growth mechanisms and the role of atomic hydrogen for the crystallization of those plasma-born nanoparticles have been reported. Heating from reactions with atomic hydrogen was shown to be necessary for the amorphous hydrogenated silicon clusters to overcome potential energy barriers to more stable structures. However, high H-atom flow rates might lead to cluster melting. In our work, we investigated quantitatively how plasma-born hydrogenated silicon clusters heat up by reactions with H-atoms. We have observed the phase transition from crystalline to amorphous and solid to liquid states as well as the on-set for etching of those nanoparticles during hydrogen exposure. Contrary to previous studies concerning the phase transition dynamics of pure or hydrogenated silicon nanoparticles with numerical thermostats, we considered here "realistic" cluster heating induced by reactions with H-atoms in a plasma reactor instead of using "artificial" velocity scaling. Our results indicate that the average energy resulting from each H-atom reaction is about the same for both the amorphous and the initially crystalline clusters before the clusters start undergoing their structural transition from the solid to the liquid state. We also show the temperature region where two investigated clusters undergo the solid to liquid phase transition; namely, from 1450 to 1704 K in the case of $Si_{15}H_{10}$ and from 1621 to 1668 K in the case of $Si_{29}H_{24}$. In those temperature regions, the cluster temperature only slowly increases, while the self-diffusion coefficients significantly augment. In a typical example, we have observed the melting dynamics of the $Si_{29}H_{24}$ cluster at 1668 K after the reaction with the 12th H-atom, showing that the phase transition from an intermediate to a completely liquid-like state takes about 15 ps after the $Si_{29}H_{24}$ cluster reacted with the 12th H-atom. Our quantitative analysis of H-induced heating and melting of plasma-born hydrogenated silicon clusters might help

to improve our understanding of dusty plasma dynamics necessary for the optimization of plasma conditions employed for *pm-Si:H* thin film deposition.

Recently, hydrogenated silicon nanoparticles synthesized in a PECVD reactor have been shown to be ideal building blocks for the deposition of high quality silicon thin films with high deposition rates. The deposition dynamics of hydrogenated silicon nanoparticles on crystalline silicon substrates under realistic plasma conditions have been investigated with a special emphasis on the influence of cluster-surface impact parameters on the deposition mechanisms ranging from soft-lading to destructive depositions. Based on our knowledge of the reaction dynamics with H-atoms, we have employed atomic hydrogen to "treat" a silicon surface which was partly damaged by a violent cluster impact; such a study can be justified by the fact that there are always H-atoms from the plasma that interact with the silicon substrate during the experimental silicon thin films deposition process. After the exposure with hydrogen atoms, we have observed that the ill-defined silicon surface is rearranged to its initial crystalline structure and that the silicon atoms of the deposited cluster are incorporated in the crystalline growth of the substrate surface. This finding, however, is only correct when a relatively low flux of H-atoms is used. At too high impinging H-atom rates, the surface will instead suffer even greater damage due to the resulting etching. The increase in kinetic energy of the silicon atoms is the result of the chemical reaction with H-atoms (either adsorption or recombination). This increase in kinetic energy permits the silicon atoms to overcome local potential barriers giving them access to epitaxial positions. Every time a silicon atom finds an epitaxial position, the total potential energy becomes somewhat more negative and the local area around that silicon atom heats accordingly slightly up. As long as this additional kinetic energy remains localized around that silicon atom, it can leave again its epitaxial position. The silicon atom can only remain "permanently" in its epitaxial position if a sufficient part of its increased kinetic energy is transferred to its neighbors. Ideally, it has to be well distributed among many neighbor atoms to avoid that another silicon atom might leave its epitaxial position. From those results, we propose for the experimentalists to expose locally disordered silicon surfaces to a hydrogen plasma after epitaxial deposition to repair local damages due to non-perfect epitaxial deposition conditions.

Epitaxial growth of thin silicon films can be achieved by many different deposition techniques. Recently, it has been shown experimentally that high-quality epitaxial growth of silicon thin films in a PECVD reactor can be achieved at low temperatures and high deposition rates when plasma-born hydrogenated silicon clusters are used as deposition precursors. The under-lying growth mechanisms for such epitaxial silicon thin films, however, have not been understood yet. With the aim to get a better understanding for those epitaxial growth mechanisms, we have performed an in-depth study of the deposition dynamics of hydrogenated silicon clusters on H-terminated Si(100)-(2×1) surfaces

by controlling the impact parameters governing the cluster-surface deposition process: impact energy, substrate temperature, and incidence angles. Four hydrogenated silicon clusters with different sizes and structures have been employed as models for plasma-born nanoparticles. Based on our first observation of epitaxial growth where clusters approached the substrate at a temperature of 373 K with an impact energy of 5.3 eV/atom, we asked the question if it is the total impact energy of 79.5 eV or the impact energy per atom (5.3 eV/atom) that is necessary for epitaxial growth. A comparison of our findings for the two smallest amorphous clusters clearly indicates that the total impact energy plays a more important role than the impact energy per atom for the epitaxial growth. For the larger clusters, however, the situation turns out to be more complicated: The deposition of the amorphous $Si_{28}H_{13}$ and the crystalline $Si_{29}H_{24}$ clusters on a crystalline silicon substrate at the same substrate temperature (373 K) with the same total impact energy (79.5 eV) results in a relatively high efficiency for epitaxial growth for the amorphous cluster (21 out of 28 silicon atoms) and a low efficiency for the crystalline one (only 5 out of 29 silicon atoms). Simply increasing the total impact energy to compensate for the higher binding energy of the crystalline cluster does not increase its efficiency for epitaxy.

For all investigated cases for bigger clusters ($Si_{28}H_{13}$ and $Si_{29}H_{24}$), we have not observed complete epitaxial growth yet. Especially, a low epitaxial efficiency was obtained in our investigations with the crystalline $Si_{29}H_{24}$ clusters. In all deposition studies of above, the impinging clusters never seem to interact with a surface area that is much larger than the initial impact area. Therefore, we started to explore the role of the cluster incidence angle since a non-normal incidence angle could lead to the spreading out of the impinging cluster over a considerably larger part of the substrate. It actually turns out that deposition of the crystalline $Si_{29}H_{24}$ cluster with non-normal incidence angles yields a very high efficiency for epitaxial growth: 24 out of 29 for an incidence angle of 30 degrees and 17 out of 29 for an incidence angle of 45 degrees; while there were only 6 out of the 29 silicon atoms that took epitaxial positions for normal incidence under the same impact conditions. Therefore, we conclude that a non-normal incidence angle might facilitate the epitaxial growth.

Based on the temperature and MSD graphs calculated from the investigated trajectories, we can conclude that a temporary phase transition to the liquid state around the impact area is necessary for cluster-catalyzed epitaxial growth of silicon thin films. In addition, we showed that non-normal cluster incidence can significantly increase the efficiency for epitaxial growth especially for larger impinging clusters. The first conclusion helps us in better understanding the underlying mechanisms of cluster-catalyzed epitaxy, while the second finding might lead to some immediate applications for industrial applications for thin crystalline silicon films at low temperatures with high deposition rates.

Due to the small size of our model substrate, we could not investigate the effect of larger incidence angles. Hence, we suggest as one future project to construct a bigger system (both substrate and clusters) to scrutinize the effects of non-normal incidence angles for getting high efficiency epitaxial growth for crystalline silicon thin films. The investigation of the deposition dynamics with larger clusters and substrates will also permit us to determine the "ideal" kinetic impact energy for epitaxy as function of cluster size, cluster structure, surface temperature, and incidence angle. In addition, the role of heat transfer rates should be explored more in detail; *e.g.,* we could try to answer the question if a colder surface could not easier absorb the excess heat resulting from the crystallization process and, thus, fix the cluster atoms more rapidly in their epitaxial positions by avoiding that they have enough kinetic energy left to leave those target positions again. In this sense, it could also be studied whether a preferential heating of only the substrate surface, instead of the entire bulk substrate, could be more efficient for epitaxy since it could combine the supply of energy; *e.g.,* from an IR-lamp, with the fast heat dissipation of the excess energy resulting from the crystallization by a cooled substrate support.

Bibliography

[1] R. A. Street, *Hydrogenated amorphous silicon*. Cambridge: Cambridge University Press, 1991.

[2] A. Luque and S. Hegedus, *Handbook of photovoltaic science and enginering*. West Sussex: John Wiley & Sons Ltd, 2003.

[3] European photovoltaic industry association, *Solar generation 6 report*. 2011.

[4] P. R. i Cabarrocas, S. Hamma, S. N. Sharma, E. B. G. Viera, and J. Costa, "Nanoparticle formation in low-pressure silane plasmas: Bridging the gap between a-Si:H and μc-Si films," *Journal of Non-Crystalline Solids*, vol. 227-230, pp. 871–875, 1998.

[5] P. R. i Cabarrocas, "Plasma enhanced chemical vapor deposition of amorphous, polymorphous and microcrystalline silicon films," *Journal of Non-Crystalline Solids*, vol. 266-269, pp. 31–37, 2000.

[6] H. Aguas, P. R. i Cabarrocas, S. Lebib, V. Silva, E. Fortunato, and R. Martins, "Polymorphous silicon deposited in large area reactor at 13 and 27 MHz," *Thin Solid Films*, vol. 427, pp. 6–10, 2003.

[7] W. Bronner, J. P. Kleider, R. Bruggemann, and P. R. i Cabarrocas, "Comparison of transport and defects properties in hydrogenated polymorphous and amorphous silicon," *Journal of Non-Crystalline Solids*, vol. 299-302, pp. 551–555, 2002.

[8] Y. M. Soro, A. Abromov, M. E. Gueenier-Farret, E. V. Johnson, C. Longeuaud, P. R. i Cabarrocas, and J. P. Kleider, "Polymorphous silicon thin films deposited at high rate: transport properties and density of states," *Thin Solid Films*, vol. 516, pp. 6888–6891, 2008.

[9] R. Butte, M. M. S. Vignoli, R. Meaudre, O. Marty, L. Saviot, and P. R. i Cabarrocas, "Structural, optical and electronic properties of hydrogenated polymorphous silicon films deposited at 150 °C," *Journal of Non-Crystalline Solids*, vol. 266-269, pp. 263–268, 2000.

[10] S.-B. Li, Z.-M. Wu, Y.-D. Jiang, W. L. J.-S. Yu, and N.-M. Liao, "Growth mechanism of microcrystalline and polymorphous silicon film with pure silane source gas," *J. Phys. D: Appl. Phys.*, vol. 41, pp. 105207.1–105207.5, 2008.

[11] P. R. i Cabarrocas, A. F. i Morral, S. Lebib, and Y. Poissant, "Plasma production of nanocrystalline silicon particles and polymorphous silicon thin films for large-area electronic devices," *Pure Appl. Chem.*, vol. 74, pp. 359–367, 2002.

[12] P. R. i Cabarrocas, N. Chaabane, A. V. Kharchenko, and S. Tchakarov, "Polymorphous silicon thin films produced in dusty plasmas: Application to solar cells," *Plasma Phys. Control. Fusion*, vol. 46, pp. B235–B243, 2004.

[13] I. V. Markov, *Crystal growth for beginners: Fundamentals of nucleation, crystal growth and epitaxy.* Singapore: World Scientific Publishing Co. Pte. Ltd, 1995.

[14] H. Khan and H. Frey, "Ion-beam deposition of nanocrystalline and epitaxial silicon films using silane plasma," *Surf. and Coat. Tech.*, vol. 116-119, pp. 472–475, 1999.

[15] C. W. Teplin, K. Alberi, M. Shub, C. Beall, I. T. Martin, M. J. Romero, D. L. Young, R. C. Reedy, P. Stradins, and H. M. Branz, "Mechanisms controlling the phase and dislocation density in epitaxial silicon films grown from silane below 800 °C," *Appl. Phys. Lett.*, vol. 96, pp. 201901.1–201901.3, 2010.

[16] P. R. i Cabarrocas, R. Cariou, and M. Labrune, "Low temperature plasma deposition of silicon thin films: From amorphous to crystalline," *Journal of Non-Crystalline Solids*, vol. 358, pp. 2000–2003, 2012.

[17] M. Labrune, X. Bril, G. Patriarche, L. Largeau, O. Mauguin, and P. R. i Cabarrocas, "Epitaxial growth of silicon and germanium on (100)-oriented crystalline substrates by RF PECVD at 175 °C," *EPJ Photovoltaics*, vol. 3, pp. 30303.1–30303.5, 2012.

[18] D. Shahrjerdi, B. Hekmatshoar, S. W. Bedell, M. Hopstaken, and D. K. Sadana, "Low-temperature epitaxy of compressively strained silicon directly on silicon substrates," *Journal of Electronic Materials*, vol. 41, pp. 494–497, 2011.

[19] M. Moreno and P. R. i Cabarrocas, "Ultra-thin crystalline silicon films produced by plasma assisted epitaxial growth on silicon wafers and their transfer to foreign substrates," *EPJ Photovoltaics*, vol. 1, pp. 10301.1–10301.6, 2010.

[20] P. R. i Cabarrocas, K.-H. Kim, R. Cariou, M. Labrune, E. V. Johnson, M. Moreno, A. T. Rio, S. Abolmasov, and S. Kasouit, "Low temperature plasma synthesis of nanocrystals and their application to the growth of crystalline silicon and germanium thin films," *MRS Online Proceedings Library*, vol. 1426, pp. 319–329, 2012.

[21] N. Chaâbane, V. Suendo, H. Vach, and P. R. i Cabarrocas, “Soft landing of silicon nanocrystals in plasma enhanced chemical vapor deposition,” *App. Phys. Lett.*, vol. 88, pp. 203111.1–203111.3, 2006.

[22] T. Nguyen-Tran, P. R. i Cabarrocas, and G. Patriarche, “Study of radial growth rate and size control of silicon nanocrystals in square-wave-modulated silane plasmas,” *Appl. Phys. Lett.*, vol. 91, pp. 111501.1–111501.3, 2007.

[23] P. R. i Cabarrocas, T. Nguyen-Tran, Y. Djeridane, A. Abramov, E. V. Johnson, and G. Patriarche, “Synthesis of silicon nanocrystals in silane plasmas for nanoelectronics and large area electronic devices,” *J. Phys. D: Appl. Phys.*, vol. 40, pp. 2258–2266, 2007.

[24] H. Vach and Q. Brulin, “Controlled growth of silicon nanocrystals in a plasma reactor,” *Phys. Rev. Lett.*, vol. 95, pp. 165502.1–165502.4, 2005.

[25] H. Vach, Q. Brulin, N. Chaâbane, T. Novikova, P. R. i Cabarrocas, B. Kalache, K. Hassouni, S. Botti, and L. Reining, “Growth dynamics of hydrogenated silicon nanoparticles under realistic conditions of a plasma reactor,” *Comput. Mat. Sci.*, vol. 35, pp. 216–222, 2006.

[26] N. Ning, G. Dolgonos, W. Morscheidt, A. Michau, K. Hassouni, and H. Vach, “Computational methods for fundamental studies of plasma processes,” *Comput. Methods Sci. Eng.*, vol. 1, pp. 224–249, 2007.

[27] Q. Brulin, N. Ning, and H. Vach, “Hydrogen-induced crystallization of amorphous silicon clusters in a plasma reactor,” *Journal of Non-Crystalline Solids*, vol. 352, pp. 1055–1058, 2006.

[28] H. Vach, “Ultrastable silicon nanocrystals due to electron delocalization,” *Nano Letters*, vol. 11, pp. 5477–5481, 2011.

[29] C. M. S. R. Biswas, G. S. Grest, “Molecular dynamics simulation of cluster and atom deposition on silicon (111),” *Phys. Rev. B*, vol. 38, pp. 8154–8162, 1988.

[30] I. Kwon, R. Biswas, G. S. Grest, and C. M. Soukoulis, “Molecular-dynamics simulation of amorphous and epitaxial Si film growth on Si(111),” *Phys. Rev. B*, vol. 41, pp. 3678–3687, 1990.

[31] G. Gilmer, C. Roland, D. Stock, M. Jaraiz, and T. D. de la Rubia, “Simulations of thin film deposition from atomic and cluster beams,” *Mater. Sci. and Eng. B*, vol. 37, pp. 1–7, 1996.

[32] J. Q. Xie and J. Y. Feng, “Molecular dynamics simulation of silicon film growth from cluster beams,” *Nucl. Instr. and Methods in Phys. Research B*, vol. 142, pp. 77–82, 1998.

[33] J. Q. Xie, J. Y. Feng, and H. W. Lu, “Molecular dynamics simulation of low-temperature growth of silicon films by cluster deposition,” *Modelling Simul. Mater. Sci. Eng.*, vol. 7, pp. 289–295, 1999.

[34] J. Tarus and K. Nordlund, “Molecular dynamics study on Si_{20} cluster deposition on Si(001),” *Nucl. Instr. and Methods in Phys. Research B*, vol. 212, pp. 281–285, 2003.

[35] N. Ning, S. M. Rinaldi, and H. Vach, “An atomicscale study of hydrogenated silicon cluster deposition on a crystalline silicon surface,” *Thin Solid Films*, vol. 517, pp. 6234–6238, 2009.

[36] N. Ning and H. Vach, “Deposition dynamics of hydrogenated silicon clusters on a crystalline silicon substrate under typical plasma conditions,” *J. Phys. Chem. A*, vol. 114, pp. 3297–3305, 2010.

[37] L. W. Chen, Y. Shibuta, M. Kambara, and T. Yoshida, “Molecular dynamics simulation of Si nanoclusters in high rate and low temperature epitaxy,” *J. Appl. Phys.*, vol. 111, pp. 123301.1–123301.6, 2012.

[38] L. W. Chen, Y. Shibuta, M. Kambara, and T. Yoshida, “Molecular dynamics simulation of the role of hydrogenated si clusters for fast rate mesoplasma epitaxy,” *J. Phys. D: Appl. Phys.*, vol. 46, pp. 425302.1–425302.6, 2013.

[39] Mazzone, “Molecular dynamics simulations of impact of energetic silicon clusters onto crystalline silicon,” *Journal of Computer-Aided Materials Design*, vol. 9, pp. 1–9, 2002.

[40] Mazzone, “Cluster beam steering onto silicon surfaces studied by molecular dynamics,” *Nucl. Instr. and Methods in Phys. Research B*, vol. 196, pp. 51–60, 2002.

[41] R. Cariou, M. Labrune, and P. R. i Cabarrocas, “Thin crystalline silicon solar cells based on epitaxial films grown at 165 °C by RF-PECVD,” *Solar Energy Materials and Solar Cells*, vol. 95, pp. 2260–2263, 2011.

[42] N. Ning, *Doctoral thesis.* PhD thesis, Ecole Polytechnique, Paris Tech, 2008.

[43] W. L. Hase, R. J. Duchovic, X. Hu, A. Komornicki, K. F. Lim, D. Lu, G. H. Peslherbe, K. N. Swamy, S. R. V. Linde, A. Varanda, W. Haobin, and R. J. Wolf, *VENUS96: General Chemical Dynamics Computer Program.* Department of Chemistry - Wayne State University, Detroit, MI, 1996.

[44] G. Kresse and J. Hafner, "Ab initio molecular dynamics for liquid metals," *Phys. Rev. B*, vol. 47, pp. 558–561, 1993.

[45] G. Kresse and J. Furthmüller, "Efficiency of ab initio total energy calculations for metals and semiconductors using a plane-wave basis set," *Comput. Mat. Sci.*, vol. 6, pp. 15–50, 1996.

[46] G. Kresse and D. Joubert, "From ultrasoft pseudopotentials to the projector augmented-wave method," *Phys. Rev. B*, vol. 59, pp. 1758–1775, 1999.

[47] D. C. Rapaport, *The art of molecular dynamics simulation.* Cambridge: Cambridge University Press, 2004.

[48] D. Frenkel and B. Smit, *Understanding molecular simulation.* Orlando: Academic Press, 2001.

[49] D. B. Graves and P. Brault, "Molecular dynamics for low temperature plasma-surface interaction studies," *Journal of Physics D: Applied Physics*, vol. 42, pp. 194011.1–194011.27, 2009.

[50] H. P. W. A. T. Saul, T. V. William, and P. F. Brian, *Numerical Recipes in FORTRAN: the art of scientific computing.* Cambrige: Cambridge University Press, 1992.

[51] J. M. Haile, *Molecular Dynamics Simulations: Elementary Methods.* New York: Wiley, 1992.

[52] C. W. Gear, *Numerical initial value problems in ordinary differential equations.* Englewood Cliffs: Prentice-Hall, 1971.

[53] C. W. Gear, *Argonne National Lab Report.* Argonne, IL: ANL-7126, 1966.

[54] F. Stillinger and T. Weber, "Computer simulation of local order in condensed phases of silicon," *Phys. Rev. B*, vol. 31, pp. 5263–5271, 1985.

[55] J. Tersoff, "New empirical model for the structural properties of silicon," *Phys. Rev. Lett.*, vol. 56, pp. 632–635, 1986.

[56] R. Biswas and D. R. Hamann, "Interatomic potentials for silicon structural energies," *Phys. Rev. Lett.*, vol. 55, pp. 2001–2004, 1985.

[57] B. Dodson, "Development of a many-body Tersoff-type potential for silicon," *Phys. Rev. B*, vol. 35, pp. 2795–2798, 1987.

[58] M. I. Baskes, "Observation of Bhabha scattering in the center-of-mass kinetic-energy range 342 to 845 keV," *Phys. Rev. Lett.*, vol. 59, pp. 266–269, 1987.

[59] T. Ohira, T. Inamuroa, and T. Adachi, "Molecular dynamics simulation of hydrogenated amorphous silicon with Tersoff potential," *Mat. Res. Spc. Symp. Proc.*, vol. 34, pp. 565–570, 1994.

[60] T. Ohira, O. Ukai, and T. Adachi, "Molecular dynamics simulations of SiH_3 radical deposition on hydrogen-terminated silicon (100) surfaces," *Phys. Rev. B*, vol. 52, pp. 8283–8286, 1995.

[61] S. Ramalingam, D. Maroudas, and E. S. Aydil, "Interactions of SiH radicals with silicon surfaces: An atomic-scale simulation study," *J. Appl. Phys.*, vol. 84, pp. 3895–3911, 1998.

[62] S. Ramalingam, P. Mahalingam, E. S. Aydil, and D. Maroudas, "Theoretical study of the interactions of SiH_2 radicals with silicon surfaces," *J. Appl. Phys.*, vol. 86, pp. 5497–5508, 1999.

[63] S. Ramalingam, D. Maroudas, and E. S. Aydil, "Atomistic simulation study of the interactions of SiH_3 radicals with silicon surfaces," *J. Appl. Phys.*, vol. 86, pp. 2872–2888, 1999.

[64] S. P. Walch, S. Ramalingam, S. Sriraman, E. S. Aydil, and D. Maroudas, "Mechanisims and energetics of SiH_3 adsorption on the pristine Si(100)-(2×1) surface," *Chem. Phys. Lett.*, vol. 344, pp. 249–255, 2001.

[65] S. Sriraman, E. S. Aydil, and D. Maroudas, "Atomic-scale analysis of deposition and characterization of a-Si:H thin films grown from SiH radical precursor," *J. Appl. Phys.*, vol. 92, pp. 842–852, 2002.

[66] S. Sriraman, E. S. Aydil, and D. Maroudas, "Growth and characterization of hydrogenated amorphous silicon thin films from SiH_2 radical precursor: Atomic-scale analysis," *J. Appl. Phys.*, vol. 95, pp. 11792–1805, 2002.

[67] S. Sriraman, S. Agarwal, E. S. Aydil, and D. Maroudas, "Mechanism of hydrogen-induced crystallization of amorphous silicon," *Nature*, vol. 418, pp. 62–65, 2002.

[68] T. Ohira, O. Ukai, and M. Noda, "Fundamental processes of microcrystalline silicon film growth: A molecular dynamics study," *Surface Science*, vol. 458, pp. 216–228, 2000.

[69] J. Tersoff, "New empirical approach for the structure and energy of covalent systems," *Phys. Rev. B*, vol. 37, pp. 6991–7000, 1988.

[70] J. Tersoff, "Modeling solid-state chemistry: Interatomic potentials for multicomponent systems," *Phys. Rev. B*, vol. 39, pp. 5566–5568, 1989.

[71] M. V. R. Murty and H. A. Atwater, "Empirical interatomic potential for Si-H interactions," *Phys. Rev. B*, vol. 51, pp. 4889–4893, 1995.

[72] T. Ohira, O. Ukai, M. Noda, Y. Takeyuchi, M. Murata, and H. Yoshida, "Molecular-dynamics simulations of hydrogenated amorphous silicon thin-film growth," *Mat. Res. Spc. Symp. Proc.*, vol. 408, p. 445, 1996.

[73] D. Alfè, M. J. Gillan, M. D. Towler, and R. J. Needs, "Diamond and b-tin structures of Si studied with quantum Monte Carlo calculations," *Phys. Rev. B*, vol. 70, pp. 214102.1–214102.8, 2004.

[74] R. Iftimie, P. Minary, and M. E. Tuckerman, "Ab initio molecular dynamics: Concepts, recent developments, and future trends," *PNAS*, vol. 102, pp. 6654–6659, 2005.

[75] F. Jensen, *Introduction to computational chemistry.* England: John Wiley & Sons Ltd, 2007.

[76] P. Hohenberg and W. Kohn, "Inhomogeneous electron gas," *Physical Review*, vol. 136, p. B864–B871, 1964.

[77] W. Kohn and L. J. Sham, "Inhomogeneous electron gas," *Physical Review*, vol. 140, p. A1133–A1138, 1965.

[78] D. Marx and J. Hutter, *Ab initio molecular dynamics: Basic Theory and advanced methods.* Cambridge: Cambridge University Press, 2009.

[79] D. Frenkel and B. Smit, *Understanding molecular simulation.* Orlando: Academic Press, 2001.

[80] D. H. Li and J. Jellinek, "Rotating clusters: centrifugal distortion, isomerization, fragmentation," *Z. Phys. D - Atoms, Molecules and Clusters*, vol. 12, pp. 177–180, 1989.

[81] J. Jellinek and D. H. Li, "Separation of the energy of overall rotation in any N-body system," *Phys. Rev. Lett.*, vol. 62, pp. 241–244, 1989.

[82] M. P. Allen and D. J. Tildesley, *Computer simulations of liquids.* Oxford: Clarendon Press, 1987.

[83] C. D. Laboratory, "Democritus: The radial distribution function," October, 2013.

[84] M. P. Allen and D. J. Tildesley, *Computer simulations of liquids.* Oxford: Clarendon Press, 1987.

[85] M. P. Allen and D. J. Tildesley, *Computer simulations of liquids.* Oxford: Clarendon Press, 1987.

[86] P. R. i Cabarrocas, A. F. i Morral, and Y. Poissant, “Growth and optoelectronic properties of polymorphous silicon thin films,” *Thin Solid Films*, vol. 403, pp. 39–46, 2002.

[87] N. Chaâbane, A. V. Kharchenko, H. Vach, and P. R. i Cabarrocas, “Optimization of plasma parameters for the production of silicon nano-crystals,” *New Journal of Physics*, vol. 5, pp. 37.1–37.15, 2003.

[88] T. Novikova, B. Kalache, P. Bulkin, K. Hassouni, W. Morscheidt, and P. R. i Cabarrocas, “Numerical modeling of capacitively coupled hydrogen plasma: Effects of frequency and pressure,” *J. Appl. Phys.*, vol. 93, pp. 3198–3206, 2003.

[89] H. Vach, “Electron-deficiency aromaticity in silicon nanoclusters,” *J. Chem. Theory Comput.*, vol. 8, pp. 2088–2094, 2012.

[90] L. Mitas, J. Therrien, R. Twesten, G. Belomoin, and M. H. Nayfeh, “Effect of surface reconstruction on the structural prototypes of ultrasmall ultrabright Si_{29} nanoparticles,” *Appl. Phys. Lett.*, vol. 78, pp. 1918–1920, 2001.

[91] G. Belomoin, J. Therrien, A. Smith, S. Rao, R. Twesten, S. Chaieb, M. H. Nayfeh, L. Wagner, and L. Mitas, “Observation of a magic discrete family of ultrabright Si nanoparticles,” *Appl. Phys. Lett.*, vol. 80, pp. 841–843, 2002.

[92] G. Belomoin, E. Rogozhina, J. Therrien, P. V. Braun, L. Abuhassan, M. H. Nayfeh, L. Wagner, and L. Mitas, “Effects of surface termination on the band gap of ultrabright Si_{29} nanoparticles: Experiments and computational models,” *Phys. Rev. B*, vol. 65, pp. 193406.1–193406.4, 2002.

[93] S. Rao, J. Sutin, R. Clegg, E. Gratton, , M. H. Nayfeh, S. Habbal, A. Tsolakidis, and R. M. Martin, “Excited states of tetrahedral single-core Si_{29} nanoparticles,” *Phys. Rev. B*, vol. 69, pp. 205319.1–205319.7, 2004.

[94] S. Rao, K. Mantey, J. Therrien, A. Smith, and M. H. Nayfeh, “Molecular behavior in the vibronic and excitonic properties of hydrogenated silicon nanoparticles,” *Phys. Rev. B*, vol. 76, pp. 155316.1–155316.9, 2007.

[95] M. R. Zachariah, M. J. Carrier, and E. Blaisten-Barojas, “Properties of silicon nanoparticles: A molecular dynamics study,” *J. Phys. Chem.*, vol. 100, pp. 14856–14864, 1996.

[96] N. Jakse and A. Pasturel, "Liquid-liquid phase transformation in silicon: Evidence from first-principles molecular dynamics simulations," *Phys. Rev. Lett.*, vol. 99, pp. 205702.1–205702.4, 2007.

[97] N. Jakse and A. Pasturel, "Dynamics aspects of the liquid-liquid phase transformation in silicon," *J. Chem. Phys.*, vol. 129, pp. 104503.1–104503.4, 2008.

[98] M. R. Zachariah and M. J. Carrier, "Molecular dynamics computaion of gas-phase nanoparticle sintering: A comparison with phenomenological models," *J. Aerosol Sci.*, vol. 30, pp. 1139–1151, 1999.

[99] T. Hawa and M. R. Zachariah, "Internal pressure and surface tension of bare and hydrogen coated silicon nanoparticles," *J. Chem. Phys.*, vol. 121, pp. 9043–9049, 2004.

[100] N. Jakse and A. Pasturel, "Dynamics of liquid and undercooooled silicon: An ab initio molecular dynamics study," *Phys. Rev. B*, vol. 79, pp. 144206.1–144206.6, 2009.

[101] P. T. Dinda, G. Vlastou-Tsinganos, N. Flytzanis, and A. D. Mistriotis, "Simulation of the melting behavior of small silicon clusters," *Phys. Rev. B*, vol. 51, pp. 13697–13704, 1994.

[102] J. Wang, G. Wang, F. Ding, H. Lee, W. Shen, and J. Zhao, "Structural transition of Si clusters and their thermodynamics," *Chem. Phys. Letters*, vol. 341, pp. 529–534, 2001.

[103] P. R. i Cabarrocas, Y. Djeridane, T. Nguyen-Tran, E. V. Johnson, A. Abramov, and Q. Zhang, "Low temperature plasma synthesis of silicon nanocrystals: A strategy for high deposition rate and efficient polymorphous and microcrystalline solar cells," *Plasma Phys. Control. Fusion*, vol. 50, pp. 124037–124045, 2008.

[104] H.-L. T. Le, N. C. Forero-Martinez, and H. Vach, "Heating and melting of plasma-born hydrogenated silicon clusters by reactions with atomic hydrogen," *Phys. Status Solidi a*, vol. 211, pp. 294–300, 2014.

[105] N. C. Forero-Martinez, H.-L. T. Le, and H. Vach, "Self-assembly in silane/hydrogen plasmas: from silicon atoms to aromatic silicon nanocrystals," *Plasma Chemistry and Plasma Processing*, vol. 34, pp. 535–543, 2014.

[106] A. F. i Morral and P. R. i Cabarrocas, "Etching and hydrogen diffusion mechanisms during a hydrogen plasma treatment of silicon thin films," *Journal of Non-Crystalline Solids*, vol. 299-302, pp. 196–200, 2002.

[107] A. F. i Morral and P. R. i Cabarrocas, "Role of hydrogen diffusion on the growth of polymorphous and microcrystalline silicon thin films," *Eur. Phys. J. Appl. Phys.*, vol. 35, pp. 165–172, 2006.

[108] S. Sriraman, M. S. Valipa, E. S. Aydil, and D. Maroudas, "Hydrogen-induced crystallization of amorphous silicon thin films. I. Simulation and analysis of film postgrowth treatment with H_2 plasmas," *J. Appl. Phys.*, vol. 100, pp. 053514.1–053514.11, 2006.

[109] M. S. Valipa, S. Sriraman, E. S. Aydi, and D. Maroudas, "Hydrogen-induced crystallization of amorphous si thin films. II. Mechanisms and energetics of hydrogen insertion into Si–Si bonds," *J. Appl. Phys.*, vol. 100, pp. 053515.1–053515.13, 2006.

[110] H. J. C. Berendsen, J. P. M. Postma, W. F. Vangunsteren, A. Dinola, and J. R. Haak, "Molecular dynamics with coupling to an external bath," *J. Chem. Phys.*, vol. 81, pp. 3684–3690, 1984.

[111] M.Timonova, B. J. Lee, and B. J. Thijsse, "Sputter erosion of Si(001) using a new silicon mean potential and different thermostats," *Nucl. Instr. Meth.*, vol. 255, pp. 195–201, 2007.

[112] M. Moreno, G. Patriarche, and P. R. i Cabarrocas, "Fine-tuning of the interface in high-quality epitaxial silicon films deposited by plasma-enhanced chemical vapor deposition at 200 °C," *Journal of materials research*, vol. 28, pp. 1626–1632, 2013.

[113] E. Schmich, N. Schillinger, and S. Reber, "Silicon cvd deposition for low cost applications in photovoltaics," *Surf. & Coat. Tech.*, vol. 201, pp. 9325–9329, 2007.

[114] M. Labrune, M. Moreno, and P. R. i Cabarrocas, "Ultra-shallow junctions formed by quasi-epitaxial growth of boron and phosphorous-doped silicon films at 175 °C by rf-PECVD," *Thin Solid Films*, vol. 518, pp. 2528–2530, 2010.

[115] H. Vach, "Lost-memory model for the surface scattering of van der Waals clusters," *Phys. Rev. B*, vol. 61, pp. 2310–2315, 2000.

[116] E. Fort, A. D. Martino, F. Pradère, M. Châtelet, and H. Vach, "Enrichment of binary van der Waals clusters surviving surface collisions," *J. Chem. Phys.*, vol. 110, pp. 2579–2587, 1999.

[117] F. Pradère, M. Benslimane, M. Châtelet, A. D. Martino, and H. Vach, "Species selective surface scattering," *Surf. Sci.*, vol. 375, p. 375, 1997.